Exploring quadrupolar MRI for healthcare benefits

Daria V. Fomina, MPhys

Thesis submitted to the University of Nottingham for the degree of

Doctor of Philosophy

April 2024

To my mum and my husband

Abstract

Magnetic resonance imaging (MRI) and spectroscopy (MRS) of sodium (^{23}Na) are of great interest in biomedical research due to their sensitivity to tissue viability and ion homeostasis (Madelin, Lee, et al., 2014). In biological tissue, sodium experiences restricted and anisotropic motion through interaction with different macromolecules. Because of its quadrupolar nature, sodium possesses a bi-exponential transverse NMR relaxation with components T_{2short} and T_{2long} which account for 60% and 40%, respectively.

Recently, a new paradigm has appeared that alongside renal sodium regulation in the human body, skin also participates in the control of sodium homeostasis (Selvarajah et al., 2018). The skin dermis is enriched with proteoglycans (PGs) and glycosaminoglycans (GAGs) in the extracellular matrix, which provide a high density of negatively charged sites to osmotically inactivate sodium cations (Titze et al., 2004).

In this thesis, type 2 Diabetes Mellitus (T2DM) was chosen as a clinical model to investigate ^{23}Na relaxation in human skin. T2DM accounts for 90% of all cases of diabetes in the world, which is estimated at 537 million (IDF, 2021). This thesis aims to demonstrate that sodium relaxation times, T_{2short} and T_{2long}, and quadrupolar interaction ω_Q in human skin may serve as a biomarker for the presence of T2DM and provide more insight into the disease's development. Single-quantum (SQ) and multiple-quantum filtering (MQF) spectroscopy was applied to *ex vivo* human skin samples in ultra-high 9.4 T to determine these parameters. The proposed methodology can be translated to other diseases involving sodium homeostasis like chronic kidney disease and cystic fibrosis.

Since low-field portable NMR devices have been developed recently and found their biomedical application in profiling tendons and skin (Mitchell et al., 2006), the sodium relaxation properties in the skin studied in a high magnetic field created a motivation to translate this work into sodium measurements in low inhomogeneous fields. A STRAFI setup was designed where a poor-shielded superconducting 9.4 T magnet served as a source of the polarizing magnetic field B_0, and two probes with different diameters were constructed. Sodium signal acquisitions and relaxation measurements were conducted in a fringe field of 0.5 T with a static gradient of 4.1 T/m on phantoms with a range of sodium concentrations from saturated solutions to 0.125 M. The experiments aimed to assess the feasibility of sodium detection from concentrations close to ones in biological tissues. In the future, this work could serve as a basis for the design of a new portable sodium sensor based on a permanent magnet to perform sodium measurements in the skin of patients *in vivo*.

Acknowledgements

I would like to acknowledge all the people who have helped me during my whole PhD. Firstly, I would like to thank my supervisors, Dr Galina Pavlovskaya and Prof Thomas Meersmann, for the amazing opportunity to study for the PhD in the UK and the guidance and support throughout it. Special thank you goes to Dr Andrew Peters: even when my research did not go into your area of expertise, I highly appreciated your support.

I would like to thank members of the research team that I have worked with: thank you to Dr Gregory Rees for training on a Bruker spectrometer and to Dr Christopher Philp for valuable guidance, understanding and support during my time in the lab and for interesting conversations about life in general. Special thanks to Max Filkins and Arthur Harrison for being encouraging and supportive lab mates, for brainy discussions about science and for tips and tricks about life during the PhD in the UK.

I am also very thankful to Dr Laura Bortolotti who was very kind to me from the very first moment we met at SPMIC and who gave me a lot of encouragement, support and boosts of motivation and positive energy during my time in the centre and especially at difficult times. All of these are highly appreciated. A special thank you to Sarah Wolfe, a woman with a big heart, whose anytime willingness to listen and help really aided me in keeping going. The whole SPMIC stands on your energy and desire to help people.

And finally, my sincere gratitude to my family. A big thank you to my mum for giving me the courage to start this PhD journey and always believing in me more than I have in myself. It was not an easy journey, but you always have been on my side no matter what. And to my husband Zak, who has been my fortress throughout my whole PhD. You have been my inspiration; you gave me strength and faith in myself like nobody else could in the most difficult and challenging times. I am infinitely grateful to you both.

Contents

List of Figures

List of Tables

Abbreviations

AC	Alternating Current
BP	Blood Plasma
CDF	Cumulative Distribution Function
CF	Cystic Fibrosis
CKD	Chronic Kidney Disease
CPMG	Carr-Purcell-Meiboom-Gill
CSF	Cerebrospinal Fluid
DQ/DQC	Double Quantum/Double Quantum Coherence
DQF-MA	Double Quantum Filtering with Magic Angle
DW	Dwell Time
EC	Extracellular
ECF	Extracellular Fluid
ECM	Extracellular Matrix
EFG	Electric Field Gradient
ENaC	Epithelial Sodium Channel
ESRD	End-Stage Renal Disease
FID	Free Induction Decay
FLASH (MRI)	Fast Low Angle Shot (MRI)
FOV	Field Of View
FT	Fourier Transform
GAGs	Glycosaminoglycans
GARField	Gradient At Right angles to Field
GE	Gradient Echo
GLUT	GLUcose Transporters

GM	Grey Matter
^{1}H	Proton
HA	Hyaluronic Acid
HD	Haemodialysis
IC	Intracellular
ICP-OES	Inductively Coupled Plasma Optical Emission Spectrometry
ISTOs	Irreducible Spherical Tensor Operators
IV	Intravascular
JB test	Jarque-Bera test
KS test	Kolmogorov-Smirnov test
LB	Line Broadening
LVH	Left Ventricular Hypertrophy
MRI	Magnetic Resonance Imaging
MQ/MQC	Multiple Quantum/Multiple Quantum Coherence
MQF	Multiple Quantum Filtering
MyD	Myotonic Dystrophy
Na/Na^+/^{23}Na	Sodium
Na^+/K^+-ATPase	Sodium–Potassium Adenosine Triphosphatase
NMR	Nuclear Magnetic Resonance
NMR-MOUSE	MObile Universal Surface Explorer
NS	Number of Scans (Averages)
OA	Osteoarthritis
OP	Osteoporosis
PGs	Proteoglycans
PL	Pulse length

PTFE	Polytetrafluoroethylene
rf	Radio frequency
RG	Receiver Gain
RQI	Residual Quadrupolar Interaction
SD	Standard Deviation
SGLT-2	Sodium-Glucose Like Transporters 2
SNR	Signal-to-Noise Ratio
SR test	Serial Randomness test
SSc	Systemic Sclerosis
STRAFI	STRAy Field Imaging
SQ/SQC	Single Quantum/Single Quantum Coherence
T2DM	Type 2 Diabetes Mellitus
TD	Time Domain
TE	Echo Time
TQ/TQC	Triple Quantum/Triple Quantum Coherence
TQF	Triple Quantum Filtering
TR	Repetition Time
TSC	Tissue Sodium Concentration
VEGF-C factor	Vascular Endothelial Growth factor C
WHO	World Health Organization
WM	White Matter
w/w	Weight in Weight

1 Introduction

Magnetic resonance imaging (MRI) is a widely used diagnostic tool which plays a significant role in modern healthcare routines. Conventional MRI technique uses proton nuclei, excitation of which by radiofrequency (RF) pulses and spatial encoding with magnetic field gradients produces an MR image. However, MRI or more general nuclear magnetic resonance (NMR) phenomenon can be observed on other nuclei whose spin quantum number is non-zero. One particular nucleus of most interest in this thesis is sodium.

Sodium is a vital ion and also the second NMR-sensitive nucleus that is most abundant in living organisms: sodium is a primary cation found in the extracellular fluid of the human body (Guyton & Hall, 2006) which is about 50% of the total body water by weight (Ruperto et al., 2019). Sodium performs many essential functions on a cellular level: osmotic regulation, transmitting nerve impulses and excitation of muscles, and energy turnover, which translates to proper functioning on the organ and body level (Guyton & Hall, 2006). Changes in cell homeostasis often precede macroscopic appearances of pathological conditions. Therefore, it is of high interest to detect these changes as early as possible, and this is where sodium NMR has the potential to fulfil these needs.

Over the past four decades, ^{23}Na MRI has undergone significant technical advancement to become a viable tool in biomedical research (Madelin, Lee, et al., 2014; Ouwerkerk, 2011). Detecting alterations in the total tissue sodium concentration is crucial because it can indicate an inability of Na^+/K^+ ATPase to maintain the sodium gradient across the cell membrane, which can reveal the presence of pathology (Pirahanchi et al., 2023). In addition, investigating the molecular surroundings of sodium ions through sodium NMR, such as the interaction of sodium with proteoglycans, is an intriguing avenue that could yield valuable insights into the health status of specific tissues and organs (Wheaton et al., 2004). Recent findings revealed a correlation between dietary sodium chloride intake and blood pressure and, as a consequence, hypertension and opposed the traditional view of exclusively renal handling of sodium balance in the human body (Selvarajah et al., 2018). The traditional paradigm was challenged by an examination of sodium and water excretion 4 h after the infusion of hypertonic saline in healthy individuals (Olde Engberink et al., 2017). It was shown that the amount of sodium observed in the urine was only half of the anticipated quantity. This suggests that a portion of the infused sodium was retained in the body osmotically inactive. Therefore, it was proposed that skin might serve as a buffer for sodium ions (Na^+) by being full of negatively charged macromolecules which can store sodium osmotically inactive (Titze et al., 2004). In addition, elevated sodium content was found in the skin of patients with type 2 Diabetes Mellitus (T2DM) compared to hypertensive subjects (Kannenkeril et al., 2019) indicating that there are supplementary unexplored mechanisms of sodium regulation and retention in the skin in T2DM. Understanding the molecular environment of sodium ions in the skin can be gainful for a better understanding of the pathophysiology and monitoring of the disease.

This thesis is divided into 3 chapters. Firstly, Chapter 2 overviews the basics of the Nuclear Magnetic Resonance phenomenon. It starts with introducing fundamental quantum mechanical properties such as nuclear spin, which leads to the Zeeman effect and definition of macroscopic magnetization. Then the nuclear sensitivity is discussed engaging other nuclei than a proton like sodium.

The dynamics of spin-3/2 nuclei is better described by quantum mechanics (second part of Chapter 2). Spin density operators and irreducible tensor formalism are introduced which are well adapted for illustrating the relaxation of spin-3/2 nuclei under electric quadrupolar interaction. Types of electric quadrupolar interaction, corresponding motional regimes and relaxation times are described. Single quantum (SQ) and multiple quantum (MQ) coherences are introduced.

One approach to analyse the molecular environment of sodium nuclei in the skin is to investigate its relaxation characteristics by examining the time evolution of SQ and MQ coherences to obtain sodium transverse relaxation times T_{2short} and T_{2long}. Relaxation times of the coherences are affected by the speed of molecular motion and tissue ordering which links with quadrupolar interactions of the quadrupole moment of the sodium nucleus with electric field gradients (EFG) created by macromolecules in the tissue (Navon et al., 2001). The influence of either quadrupolar interaction or slow motion on sodium relaxation can be probed separately by pulse sequences like double quantum filter with magic angle (DQF-MA) and triple quantum filter (TQF) correspondingly. Chapter 3 describes how the Carr-Purcell-Meiboom-Gill (CPMG) pulse sequence and multiple quantum filters mentioned above are applied to study the molecular environment of sodium in the *ex vivo* skin samples of patients suffering from type 2 Diabetes Mellitus and their control counterparts. Obtained results and interpretations of the measurements are reported. As biexponential relaxation of sodium is observed in biological tissues (Madelin, Lee, et al., 2014), CPMG decays were fit to extract T_{2short} and T_{2long}. In DQF-MA experiments, only coherences arising from the quadrupolar interaction are detected. In TQF experiments, only slow-moving sodium produces a signal. Analysing the time evolution of MQ coherences, T_{2short}, T_{2long} and the value of quadrupolar interaction ω_Q can be obtained. The values of T_{2short}, T_{2long} and ω_Q of control and diabetic patients are compared to extract the potential difference in skin sodium regulation and tissue properties like degree of order and viscosity with and without T2DM. In addition, a comparison of the SQ and MQ methods is discussed.

Sodium MRI has been shown to be a useful tool for studying sodium in skin tissue (Kopp et al., 2013; Linz et al., 2014; Wang et al., 2017). However, these studies are severely restricted because of the inability to reach a resolution high enough to distinguish different skin structures. Also, in some situations, a patient cannot be put inside an MRI scanner due to some physiological conditions or external equipment such as a haemodialysis machine during treatment (Dahlmann et al., 2015; Kopp et al., 2018). Nonetheless, it might be very important to monitor the efficiency of the intervention by measuring sodium concentration in the skin of patients with diseases like hypertension (Kopp et al., 2013), chronic kidney disease (CKD) (Nerbass et al., 2018; Qirjazi et al., 2021) and type 2 Diabetes Mellitus (Kannenkeril et al., 2019; Kopp et al., 2018). To overcome the practical difficulties of measuring skin sodium with whole-body MRI scanners, portable NMR devices can be developed that are based on permanent magnets.

Portable NMR devices like the NMR-MOUSE and GARField were developed to study samples much bigger than NMR probes (Blümich et al., 2008) and planar samples including human skin (Dias et al., 2003; Landeghem et al., 2011) using proton nuclei. Both setups can be considered as varieties of STRAy Field Imaging (STRAFI) (Randall, 2011), as measurements are performed in a stray field of a permanent or a superconducting magnet like in a standard STRAFI arrangement. The described measuring systems can be potentially adapted for detecting sodium signal in living tissues like skin. However, only a couple of papers have been published so far describing sodium signal acquisition by devices based on permanent magnets:

investigating salt disposition in walls of ancient buildings (Zia, 2016) and salt content in cheese products (Greer et al., 2019) that are very far from biomedical applications. The application of devices possessing a high magnetic field gradient to biological tissues is complicated due to low sodium concentrations and short relaxation times (F. Boada et al., 2005). As in biological tissues, sodium possesses biexponential transverse relaxation with T_{2short} and T_{2long} components, short echo times should be used to detect T_{2short} as it is responsible for 60% of the signal.

In order to construct a portable device for sodium measurements in biological tissues *in vivo*, the feasibility of sodium detection in inhomogeneous fields was assessed. This is the aim of Chapter 4, which describes the utilization of the "like-STRAFI" setup using a fringe field of a poor-shielded superconducting magnet, home-built volume probes with different diameters and a miniaturized spectrometer. Beforehand, the fringe magnetic field of the magnet was simulated in MATLAB and then accurately measured in an axial direction and on a perpendicular planar surface with two gaussmeters with different geometries of sensing probes. Then sodium measurements were performed with phantoms of aqueous NaCl solutions of concentrations from saturated to 0.125 M and in an agar gel with 4.87 M NaCl. Two probes were constructed to examine the effectiveness of increasing the excitation slice area on signal-to-noise ratios (SNRs) and overall measurement times, as indicated in the findings.

Chapter 5 contains general conclusions for all Chapters of the thesis and future work is outlined.

Effect of the COVID-19 Pandemic on my PhD research study

My PhD study started in December 2018, and it was funded by the "Vice-Chancellor's Scholarship for Research Excellence" for 3 years. The COVID-19 pandemic began three months into my 2^{nd} year. My research activities in the laboratory at the Sir Peter Mansfield Imaging Centre (SPMIC) were heavily disrupted due to the lack of access to laboratory facilities. At that time, there were three main projects that I was working on: (1) sodium MRI of human skin samples in 9.4 T, processing of the MRI data (Chapter 3) and establishing a pipeline of performing ICP-OES analysis in the School of Chemistry to determine the absolute sodium concentration in different parts of skin samples (dermis, fat and plasma). These activities were very important as the publication of the results was expected by the project collaborators; (2) development of a portable sodium NMR device based on permanent magnets to measure sodium from planar objects and human skin *in vivo* in a low inhomogeneous magnetic field (Chapter 4); (3) development of a protocol of 129-xenon detection on the 7T clinical scanner with its future adaptation to human subjects.

Although sodium MRI in 9.4 T was performed for a significant number of human skin samples before the COVID-19 pandemic occurred in March 2020, more deliveries of the human skin samples were planned for MRI scanning and performing ICP-OES analysis in the School of Chemistry. These experiments were important for the preparation of the publication which was expected as soon as possible by the project collaborators from Coventry. I was doing my best to develop skills for working on an NMR spectrometer, data processing and helping my lab PhD colleagues by learning rat lung extraction techniques. For ICP, I was developing skills in dissecting human tissue, working with strong acids for the digestion of the human tissue, and accurate pipetting for diluting the digested material. To perform ICP, I needed to rely on other researchers in the School of Chemistry and their workload due to limited access to expensive equipment. Firstly, I was testing the digesting pipeline on gel phantoms with known sodium concentration to make sure that it was producing adequate results. After that, I could move to chicken tissues and then human skin samples. By the time the pandemic occurred, the ICP analysis was performed only for two skin samples.

The development of the portable NMR device for sodium measurements was at an early stage. I was developing skills in building NMR probes, learning how to operate a miniaturized NMR spectrometer and also allocating my time to oversee undergraduate students working in our laboratory. While designing a new NMR probe from scratch, I also was trying to fix another handmade probe that a lab colleague broke before the start of my PhD.

The development of a protocol for 129-xenon (^{129}Xe) detection on the 7T clinical scanner was also at an early stage. A new ^{129}Xe NMR probe needed to be tested with gas phantoms containing pressurised ^{129}Xe to obtain a xenon signal. My supervisor and I were trying to understand the details of the transmit-receive tract of the 7T clinical scanner to be able to control the power applied to the probe. Also, the scanner should have been programmed to work with the new coil and new nucleus. Due to the extreme workload of my supervisor as a faculty manager at the SPMIC and the limited booking availability of the 7T scanner as a shared piece of equipment, I was not able to have the appropriate training to become an independent scanner operator.

When the first lockdown was announced in March 2020, my main supervisor and I decided to shift the focus to data processing for the human skin samples and prepare a draft of a paper. In April 2020, I made a presentation at the Respiratory Division Science meeting at the School of Medicine.

After the COVID-19 pandemic occurred in March 2020, communications with one of my supervisors were drastically reduced due to his overwhelming responsibilities as a safety officer. This responsibility continued post-lockdown. Because of this, I could not acquire new skills in working on a clinical 7T MRI scanner, which was originally planned to form part of my thesis. Therefore, it was decided with all of my supervisors that it was not feasible to continue working on this project anymore.

In June 2020, my mother and grandmother (from my mother's side) contracted COVID-19 and were administered to a hospital in Russia, where they live. My grandmother died after 7 days in the hospital due to serious complications. Although my mother had not fully recovered from the infection, she needed to organize a bereavement by herself as at that time I could not leave the UK to help her because Russia had its borders closed, and my mother had not fully recovered and therefore there was a risk to me catching COVID-19 with unknown outcomes.

The fact that I was not able to help my family in any way heavily affected my mental health. Unfortunately, I struggled to cope, and my mental health declined. Therefore, I sought support from the university health centre and cognitive behaviour therapists (CBT). However, I had not got an opportunity to go home to my family due to COVID-19 restrictions. This was an aggravating circumstance for my mental health.

My projects were not included in the list of selected priority projects of the School of Medicine until January 2021, thereby I could not use laboratory facilities for 10 months (March 2020 – December 2020). Also, from January 2021 to June 2021, the capacity of the laboratory was limited due to pandemic restrictions. Therefore, my time in the laboratory was limited as other PhD students also needed to work in the lab and social distancing restrictions were in place.

At the beginning of May 2021, my other grandmother (from my father's side) died and again I could not participate in the bereavement due to COVID-19 restrictions.

The described events, as well as general anxiety during the pandemic, heavily affected my mental health and my ability to work towards my PhD. In July 2021, by the university health centre, I was recommended to have additional CBT sessions to help me with recovering.

Despite struggling with my mental health, I presented a digital poster at ISMRM 2021 (15-20 May), made a presentation at the SPMIC seminar (June 2020), obtained the required training credits and continued working on the data processing and construction of the new sodium probe.

As 10 months of lack of access to laboratory facilities heavily impacted my research activities, I requested 4 months of unfunded extension to my registered period of study: from December 2021 to March 2022. I dedicated the extension time to developing the design of the sodium probe and performing low-field sodium measurements. Before the start of the extension time, the project's objective was modified to align with the available reduced time frame. Therefore, instead of constructing a device based on permanent magnets, it was decided to change it to a construction of a volume coil and perform measurements in the inhomogeneous fringe field of the superconducting magnet.

Overall, the impact of the COVID-19 pandemic on my PhD can be summarized as follows: (1) the project with 129-xenon at 7 T had to be cancelled; (2) deliveries of human skin samples were interrupted and consequently their ICP-OES analysis could not be done; (3) the time in the laboratory required for the development of the sodium probe was extremely reduced.

2 Theoretical background

This Chapter contains 2 sections. Section 2.1 provides a basic quantum mechanical description of the NMR phenomenon in general. Section 2.2 gives a quantum mechanical explanation specifically for the spin-3/2 systems.

2.1 Basics of Nuclear Magnetic Resonance

The fundamentals of NMR are described. A more comprehensive theory of NMR physics (classical and quantum descriptions) can be found in (Levitt, 2008).

2.1.1 Nuclear Spin and Zeeman Effect

Any nucleus consists of protons and neutrons which possess an intrinsic angular momentum called spin. The spin of the nucleus depends on the number of protons and neutrons and it is identified by the spin quantum number I. Nuclei with non-zero I possess a non-zero magnetic moment μ_I as in eq. [2.1]:

$$\vec{\mu}_I = \gamma \vec{I}, \qquad [2.1]$$

where γ is the gyromagnetic ratio which is isotope-specific. Units of γ are radians per second per tesla $\left[\frac{rad}{s \cdot T}\right]$. As nuclear spin (angular momentum) is quantized, the magnitude of the magnetic moment is also quantized (eq. [2.2]):

$$\mu_I = \gamma \hbar \sqrt{I(I+1)}, \qquad [2.2]$$

where $\hbar$ is the reduced Planck constant (or Dirac constant) equal to the Plank constant divided by 2π [joule·seconds, J·s]. It is a fundamental constant connecting the mass, energy and frequency of a proton.

If a nucleus is placed in a magnetic field of internal or external origin, the magnetic moment of the nucleus interacts with the magnetic field. Energy levels of the nucleus split into several sublevels (states) and this phenomenon is called the Zeeman effect.

To the nuclear spin corresponds a spin operator $\hat{I} = \{\hat{I}_x, \hat{I}_y, \hat{I}_z\}$. Usually, the direction of the external magnetic field $\vec{B}_0$ is chosen along the z-axis. Eigenvalues of the z-component of the angular momentum operator $\hat{I}_z$ are $I_z = m\hbar$, where m is a magnetic quantum number which can take values of $I, I-1, \ldots, -I+1, -I$. Hence, any given nucleus can possess $2I+1$ angular momentum states or Zeeman states (Levitt, 2008). The z-component of the magnetic moment can be expressed as in eq. [2.3]:

$$\mu_z = \gamma I_z = \gamma m\hbar. \tag{2.3}$$

In the absence of a magnetic field, the nuclear states with different I_z are degenerate – they have the same energy. If a nucleus is placed in a magnetic field, however, the degeneracy can be lifted: the nuclear magnetic moment interacts with the external magnetic field and the states no longer have the same energy. The energy of the Zeeman state with a magnetic quantum number m can be described by eq. [2.4]:

$$E_m = -\mu_z B_0 = -\gamma m\hbar B_0. \tag{2.4}$$

As a result, the energy difference between the two states is equal to (eq. [2.5]):

$$\Delta E = \gamma\hbar B_0. \tag{2.5}$$

As $\Delta E = \hbar\omega_0$, it can be derived that (eq. [2.6])

$$\omega_0 = \gamma B_0, \tag{2.6}$$

where $\omega_0 \left[\frac{rad}{s}\right]$ is the frequency of the electromagnetic radiation required to induce a transition between the energy levels.

The Zeeman splitting for proton (^{1}H) and sodium (^{23}Na) nuclei is shown in Figure 2.1. The distance between energy levels depends linearly on the applied field B_0 and, therefore, ω_0.

At the thermal equilibrium, the probability to find the system of N spins with energy E_m at an absolute temperature, T (Kelvin, K), is described by the normalized Boltzmann factor (Haacke et al., 1999) as in eq. [2.7]:

$$P_m = \frac{e^{-\frac{E_m}{k_B T}}}{Z}, \tag{2.7}$$

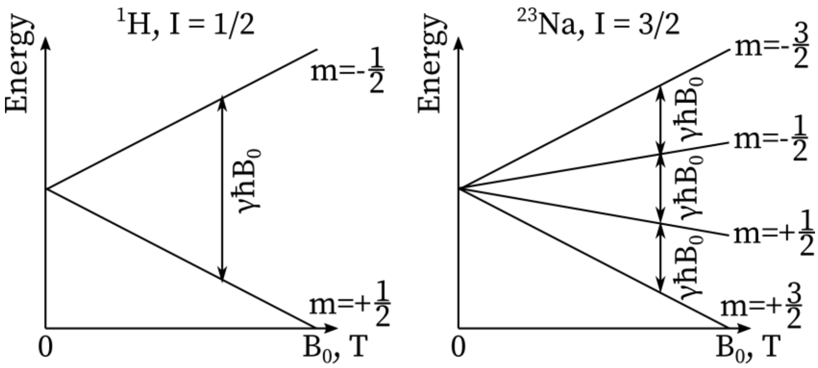

Figure 2.1. Nuclear Zeeman states of proton ^{1}H ($I = 1/2$) and sodium ^{23}Na ($I = 3/2$). As γ is different for these nuclei, the distance between the energy levels and, therefore, ω_0 are different.

where k_B is the Boltzmann constant [J/K], and Z is the partition function defined by eq. [2.8]:

$$Z = \sum_{m=-I}^{I} e^{-\frac{E_m}{k_B T}}. \qquad [2.8]$$

The thermal average of the z-component of the magnetization $\vec{M}_0$ can be expressed as in eq. [2.9]:

$$M_0 = \rho_0 \sum_{m=-I}^{I} P_m \mu_z(m), \qquad [2.9]$$

where $\rho_0 = N/V$ is the number of spins N per volume V, i.e. spin density. Given eq. [2.3]-[2.4], the equilibrium magnetization is as follows (eq. [2.10]):

$$M_0 = \rho_0 \gamma \hbar \frac{\sum_{m=-I}^{I} m e^{\frac{m\hbar\omega_0}{k_B T}}}{\sum_{m=-I}^{I} e^{\frac{m\hbar\omega_0}{k_B T}}}. \qquad [2.10]$$

If we designate $\mathcal{B} = \frac{\hbar\omega_0}{k_B T}$ (Boltzmann factor), at room and body temperatures, $\hbar\omega_0 \ll k_B T$ ($\mathcal{B} \ll 1$), therefore, for protons it can be written as in eq. [2.11]:

$$e^{\mathcal{B}} = 1 + \mathcal{B} + O(\mathcal{B}^2) + \cdots \cong 1 + 6.6 \times 10^{-6} B_0. \qquad [2.11]$$

The expression for the equilibrium magnetization can be approximated by eq. [2.12]:

$$M_0 \simeq \rho_0 \frac{I(I+1)\gamma^2\hbar^2}{3k_B T} B_0. \qquad [2.12]$$

2.1.2 NMR sensitivity

The highest gyromagnetic ratio and abundance in the human body made protons the most used and diagnostically important nuclei in NMR. The use of other nuclei for MRS and MRI in the human body is challenging due to low signal strength relative to protons. Rotating magnetization of the spins in a sample is defined as in eq. [2.13]:

$$M_+(t) = M_x(t) + iM_y(t) = M_0 e^{-i\omega_0 t + i\phi_0}. \qquad [2.13]$$

where ϕ_0 is the initial phase in the transverse plane. $M_+(t)$ creates a time-varying magnetic flux that induces electromotive force (EMF) in a receiving coil according to Faraday's law. EMF is defined as in eq. [2.14] (Haacke et al., 1999):

$$EMF = -\frac{d}{dt}\int d^3r \vec{M}(\vec{r},t) \cdot \vec{B}^{receive}(\vec{r}), \qquad [2.14]$$

where the receive coil produces the magnetic field $\vec{B}^{receive}(\vec{r})$ per unit current. Making the assumptions that spatial variations of $\vec{M}(\vec{r},t)$ and $\vec{B}^{receive}(\vec{r})$ are small and the time dependence of $\vec{M}(\vec{r},t)$ is caused mainly by precession, one can simplify that EMF is proportional to $\omega_0 M_0$. Using eq. [2.12] and noting $\omega_0 \propto \gamma$, the relative signal strength (or sensitivity) R of a given nuclear isotope can be expressed as in eq. [2.15] (Haacke et al., 1999):

$$R = |\gamma|^3 \cdot r \cdot a \cdot I(I+1), \qquad [2.15]$$

where r is the relative abundance of the nuclear isotope in the human body ($r = 1$ for protons), and a is a natural abundance relative to all stable isotopes of the given nucleus. The characteristics mentioned above for several nuclei presented abundantly in the human body are shown in Table 2.1. The molarity of ^{1}H in the human body can be calculated as follows: considering a mass fraction of ^{1}H in the human body as 9.5% (Rundo & Bunce, 1966), the average density of the human body ρ_{body} was taken as 1.05 g/ml (Pollock et al., 1975, 1976), and a molar mass of ^{1}H M_{1H} is 1 g/mol, then average hydrogen molarity C_{1H} can be calculated as follows (eq. [2.17]):

$$C_{1H} = \frac{\nu_{1H}}{V_{body}} = \frac{m_{1H}}{M_{1H} \cdot \frac{m_{body}}{\rho_{body}}} = \frac{0.095 m_{body}}{M_{1H} \cdot \frac{m_{body}}{\rho_{body}}} = 99.75 \frac{mol}{L} = 99.75M. \qquad [2.16]$$

The relative abundance of sodium ^{23}Na in the human body was calculated in a similar fashion: considering the total concentration of sodium ions as 54 mEq/kg (Bhave & Neilson, 2011) which equals to 1.242 g/kg, then average sodium molarity C_{23Na} can be calculated as follows (eq. [2.17]):

$$C_{23Na} = \frac{\nu_{23Na}}{V_{body}} = \frac{m_{23Na}}{M_{23Na} \cdot \frac{m_{body}}{\rho_{body}}} = 0.0567 \frac{mol}{L} = 56.7\ mM, \qquad [2.17]$$

Table 2.1. Several nuclei with their characteristics: gyromagnetic ratio $\bar{\gamma} = \gamma/2\pi$, spin I, relative abundance in the human body r, natural abundance a, and relative sensitivity R normalized by ^{1}H relative sensitivity R_{1H}.

Nucleus in the human body	**$\bar{\gamma}$, MHz/T**	**I**	**r**	**a**	**R/R_{1H}**
^{1}H, average	42.577	1/2	1.0	1.0	1
^{23}Na, average	11.262	3/2	$5.68 \cdot 10^{-4}$	1.0	$5.26 \cdot 10^{-5}$

where M_{Na} = 23 g/mol is a molar mass of sodium. From there, the relative abundance r of sodium to proton can be found by dividing C_{23Na} by C_{1H}.

Due to the relatively high abundance in the human body, sodium can be considered to be the second most NMR-sensitive nucleus after ^{1}H.

2.2 Basics of quantum mechanics for spin = 3/2

2.2.1 Spin density operator

In quantum mechanics, the state of the particle i can be described by a continuous complex wave function $|\Psi_\mathrm{i}\rangle$ which in general depends on space coordinates and time. The wave function can be represented in terms of "basis functions" $|\psi_n\rangle = |n\rangle$ (eq. [2.18]):

$$|\Psi_i(t)\rangle = \sum_n c_n^i(t)|n\rangle, \qquad [2.18]$$

where $c_n^i(t)$ is a complex coefficient which is generally time dependent. Any spin state of a nucleus with a quantum number I may be represented in the basis of the $2I + 1$ Zeeman eigenstates $|m\rangle$ of the operator $\hat{I}_z$. Hence for a nucleus with $I = 3/2$, there are 4 Zeeman states: $\left|+\frac{3}{2}\right\rangle$, $\left|+\frac{1}{2}\right\rangle$, $\left|-\frac{1}{2}\right\rangle$ and $\left|-\frac{3}{2}\right\rangle$, and in the basis of these states, the wave function of a nucleus can be given as follows (eq. [2.19]):

$$|\Psi_i\rangle = c_{+3/2}^i\left|+\frac{3}{2}\right\rangle + c_{+1/2}^i\left|+\frac{1}{2}\right\rangle + c_{-1/2}^i\left|-\frac{1}{2}\right\rangle + c_{-3/2}^i\left|-\frac{3}{2}\right\rangle. \qquad [2.19]$$

When an ensemble of nuclei is considered, to describe its state it is useful to use a density matrix (or a density operator) $\hat{\sigma}$ as in eq. [2.20]:

$$\hat{\sigma} \equiv \overline{|\Psi(t)\rangle\langle\Psi(t)|}, \qquad [2.20]$$

which elements can be calculated as in eq. [2.21]:

$$\sigma_{uv} = \langle u|\hat{\sigma}|v\rangle = \overline{\langle u|\Psi\rangle\langle\Psi|v\rangle} = \overline{c_u c_v^*}, \qquad [2.21]$$

where the overbar indicates the average over all particles in the ensemble.

The quantum state of a spin-3/2 ensemble may be presented as a 4 × 4 density matrix, as follows in eq. [2.22] (Levitt, 2008):

$$\hat{\sigma} = \overline{|\psi\rangle\langle\psi|} = \begin{pmatrix} \sigma_{|+3/2\rangle} & \sigma_{+1,+2} & \sigma_{+2,+2} & \sigma_{+3,0} \\ \sigma_{-1,-2} & \sigma_{|+1/2\rangle} & \sigma_{+1,0} & \sigma_{+2,-2} \\ \sigma_{-2,-2} & \sigma_{-1,0} & \sigma_{|-1/2\rangle} & \sigma_{+1,-2} \\ \sigma_{-3,0} & \sigma_{-2,+2} & \sigma_{-1,+2} & \sigma_{|-3/2\rangle} \end{pmatrix} \qquad [2.22]$$

Diagonal elements denoted $\sigma_{|+3/2\rangle}$, $\sigma_{|+1/2\rangle}$, $\sigma_{|-1/2\rangle}$, and $\sigma_{|-3/2\rangle}$ ($u = v$) represent the populations of the four Zeeman states. They are real and positive numbers and are normalized to unity. The off-diagonal elements σ_{uv} ($u \neq v$) define coherences. Each coherence has an order p_{uv} (the first number in the index position in eq. [2.22]) which is equal to the difference in Zeeman quantum numbers m for the connected states: $p_{uv} = m_u - m_v$; and q_{uv} (second number in the index position in eq. [2.22]) is a satellite order which is determined as $q_{uv} = m_u^2 - m_v^2$. Coherences are complex numbers and they come in conjugate pairs.

The difference in the populations depicts a longitudinal magnetization. Transverse magnetization is described by the presence of coherences. In its turn, coherences require a certain level of alignment of the transverse polarization vectors of spins, which corresponds to the amplitude of coherence. As coherences are complex numbers, they also have a phase which indicates the direction of the transverse magnetization in the xy-plane.

As one can see, a spin-3/2 system supports 12 coherences (Figure 2.2):

- 3 (-1)- and 3 (+1)-quantum (single quantum, or SQ) coherences between neighbouring energy levels ($p = \pm 1$). The coherence involving $|\pm 1/2\rangle$ is particularly important and associated with the central transition of the spin-3/2 system.

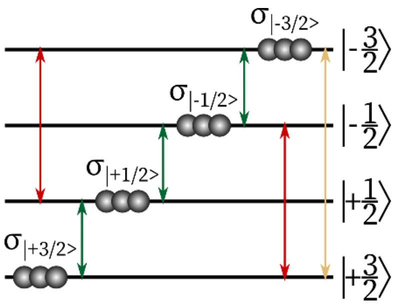

Figure 2.2. Spin-3/2 energy levels associated with quantum number m and transitions between them: $\sigma_{\pm1,0}$, $\sigma_{\pm1,+2}$, $\sigma_{\pm1,-2}$ SQ (green), $\sigma_{\pm2,+2}$, $\sigma_{\pm2,-2}$ DQ (red) and $\sigma_{\pm3,0}$ TQ (yellow) coherences. Grey balls on the energy levels represent populations.

- 2 (-2)- and 2 (+2)-quantum (double quantum, or DQ) coherences ($p = \pm 2$);
- and a pair of triple quantum (TQ) coherences ($p = \pm 3$).

2.2.2 Transformations under RF pulses

Let's examine a single-pulse experiment where a hard $(\pi/2)_x$ pulse is applied to a spin-3/2 ensemble. The density matrix $\hat{\sigma}$ at thermal equilibrium contains populations that adhere to the Boltzmann distribution and no coherences. Within the high-temperature approximation $\hbar\omega_0 \ll k_B T$ (Boltzmann factor $\mathcal{B} = \frac{\hbar\omega_0}{k_B T} \ll 1$), the thermal equilibrium spin density operator at time point (1) (before the pulse) is given by eq. [2.23] (Levitt, 2008):

$$\hat{\sigma}_{(1)} = \frac{1}{4}\hat{1} + \frac{1}{4}\mathcal{B}\hat{I}_z. \qquad [2.23]$$

A case will be considered when the RF field satisfies the strong-pulse condition $\left|\frac{\gamma}{2}B_1 \sin\theta_{RF}\right| \gg \left|\omega_Q^{(1)}\right|$, where B_1 is a magnitude of an applied oscillating RF field, θ_{RF} is an angle between $\vec{B}_1$ and $\vec{B}_0$ (both fields are applied at certain directions), and $\omega_Q^{(1)}$ is defined by eq. [2.39]. In this case, after the hard $(\pi/2)_x$ pulse at time point (2) the spin density operator will be defined as in eq. [2.24]:

$$\hat{\sigma}_{(2)} = \hat{R}_x\left(\frac{\pi}{2}\right)\hat{\sigma}_{(1)}\hat{R}_x\left(\frac{\pi}{2}\right)^{\dagger} = \frac{1}{4}\hat{1} - \frac{1}{4}\mathcal{B}\hat{I}_y, \qquad [2.24]$$

where $\hat{R}_x\left(\frac{\pi}{2}\right)$ is a pulse propagator or a rotation operator (Levitt, 2008) and the spin operator $\hat{I}_y$ for the spin-3/2 has the following matrix representation (eq. [2.25]):

$$\hat{I}_y = \frac{1}{2i}\begin{pmatrix} 0 & \sqrt{3} & 0 & 0 \\ -\sqrt{3} & 0 & 2 & 0 \\ 0 & -2 & 0 & \sqrt{3} \\ 0 & 0 & -\sqrt{3} & 0 \end{pmatrix}. \qquad [2.25]$$

Consequently, $\hat{\sigma}_{(2)}$ can be calculated as follows (eq. [2.26]):

$$\hat{\sigma}_{(2)} = \frac{1}{4}\begin{pmatrix} 1 & \frac{i\mathcal{B}}{2}\sqrt{3} & 0 & 0 \\ -\frac{i\mathcal{B}}{2}\sqrt{3} & 1 & iB & 0 \\ 0 & -i\mathcal{B} & 1 & \frac{i\mathcal{B}}{2}\sqrt{3} \\ 0 & 0 & -\frac{i\mathcal{B}}{2}\sqrt{3} & 1 \end{pmatrix}. \qquad [2.26]$$

It can be seen that the $(\pi/2)_x$ pulse does not excite the double- and triple-quantum coherences, while the excited (-1)-quantum coherences are expressed as follows (eq. [2.27]):

$$\sigma_{-1,+2_{(2)}} = -i\frac{\sqrt{3}}{8}\mathcal{B}, \qquad \sigma_{-1,0_{(2)}} = -i\frac{1}{4}\mathcal{B}, \qquad \sigma_{-1,-2_{(2)}} = -i\frac{\sqrt{3}}{8}\mathcal{B}. \qquad [2.27]$$

Equations [2.26] and [2.27] show the $(\pi/2)_x$ pulse equalizes populations of all energy levels and creates (±1)-quantum coherences where the central coherence has a larger amplitude than the satellite coherences (Figure 2.3).

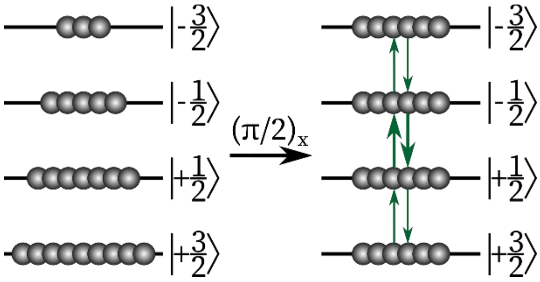

Figure 2.3. The result of the action of the $(\pi/2)_x$ pulse: all populations are equalized and (±1)-quantum coherences are created. Central $\sigma_{-1,0}$ coherence has a higher amplitude which is shown by thicker arrows.

After the $(\pi/2)_x$ pulse, during a time period $\tau/2$, the spins in the ensemble will dephase. In the operators' interpretation, $\hat{\sigma}_{(2)}$ will evolve into $\hat{\sigma}_{(3)}$ which will contain a combination of both operators $\hat{I}_y$ and $\hat{I}_x$. We will not go into details of the relaxation of the spin-3/2 system during this time period for now, however, it will be covered in the following sections. After $\tau/2$, a π_y pulse is applied. From the transformation properties of the raising and lowering operators $\hat{I}^{\pm} = \hat{I}_x \pm i\hat{I}_y$ as in eq. [2.28]:

$$\hat{R}_y(\pi)\hat{I}^{+}\hat{R}_y(\pi)^{\dagger} = -\hat{I}^{-}, \qquad \hat{R}_y(\pi)\hat{I}^{-}\hat{R}_y(\pi)^{\dagger} = -\hat{I}^{+}, \qquad [2.28]$$

it can be seen that the π_y pulse inverts the coherence order. The (+1)-quantum coherence is converted by the π_y pulse into the (-1)-quantum coherence which gives rise to the echo signal after the time $\tau/2$ from the π_y pulse. This sequence of two pulses, $(\pi/2)_x$ and π_y, is the spin echo and its coherence transfer diagram is shown in Figure 2.4. The diagram shows only (+1)-quantum coherence which solely gives an NMR signal at the end of the pulse sequence.

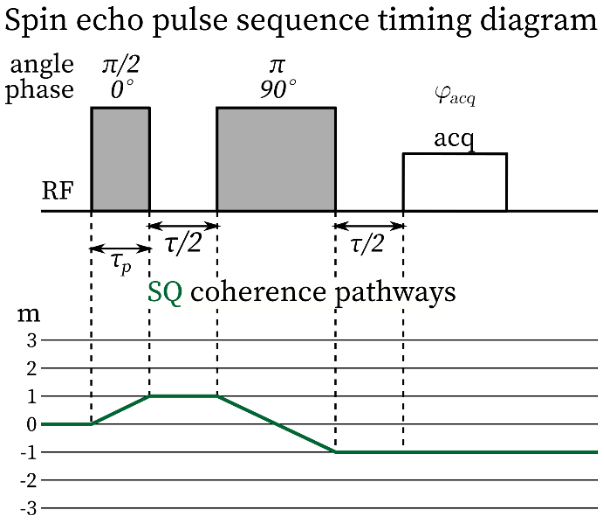

Figure 2.4. Timing diagram of the spin echo pulse sequence. Corresponding single-quantum coherence pathways are shown underneath.

2.2.3 Irreducible Tensor Formalism

For spin-1/2 systems, it is common to use product operators in Cartesian coordinates. To describe the evolution of coherences for spin-3/2 systems, it is more suitable to use irreducible spherical tensor operators (ISTOs) T_{lm} with the rank $l = 0, 1, 2, 3$ and order $m = -l, -l+1, \ldots, +l$ which form a complete and orthogonal basis (Ernst et al., 1987). In this case, the density operator can be represented in this basis as in eq. [2.29]:

$$\hat{\sigma} = \sum_{l,m} c_{lm} \hat{T}_{lm}, \qquad [2.29]$$

where c_{lm} are the complex coefficients. In this case, m can be equalized with the coherence order p. All 16 ISTOs and their expressions through the Cartesian $\hat{I}_z$ and raising and lowering operators $\hat{I}^{\pm} = \hat{I}_x \pm i\hat{I}_y$ can be found in (Madelin, Lee, et al., 2014).

The spin interaction in a static magnetic field can be described by the Hamiltonian as in eq. [2.30] (considering eq. [2.6]):

$$\hat{H}_0 = -\gamma B_0 \hat{I}_z = -\omega_0 \hat{T}_{1,0}, \qquad [2.30]$$

where $\hat{T}_{1,0} = \hat{I}_z$ represents longitudinal magnetization. To describe transformations of the tensors during an application of an RF pulse and relaxation, one can use the following rules (Ernst et al., 1987):

1. A non-selective RF pulse changes the order of coherence p (or m) within the limits $|p| \leq l$ (equivalent to rotation in three-dimensional space).
2. A free precession (without the RF field) changes rank l without changing the order p. Consequently, quadrupolar relaxation can only change l.

The schematic representation of these rules is shown in Figure 2.5. Horizontal conversions of tensors can be performed with the help of an RF pulse (in one or several steps), and vertical transformations occur due to relaxation. In thermal equilibrium, the density operator contains only $\hat{T}_{0,0}$ and $\hat{T}_{1,0}$ terms.

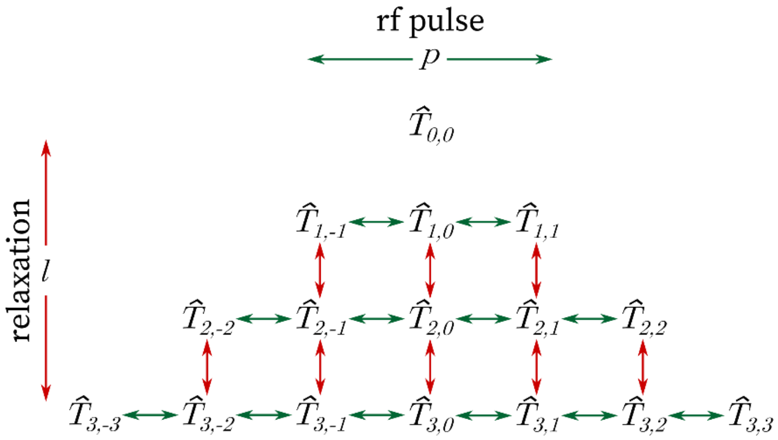

Figure 2.5. Conversion of ISTOs by RF pulses and relaxation. ISTOs represent coherences. Adapted from (Ernst et al., 1987).

In isotropic liquids under the influence of quadrupolar relaxation, only odd-rank tensors $\hat{T}_{3,\pm1}$ can be formed. In an anisotropic environment, where the residual quadrupolar interaction (RQI) (Subsections 2.2.4-2.2.5) does not vanish due to averaging, tensors of the second rank $\hat{T}_{2,\pm1}$ can be also generated. To distinguish between these two cases, different MQF experiments can be performed. For instance, in the case of RQI generated $\hat{T}_{2,\pm1}$ can be reformed by another pulse to a double-quantum coherence (DQC) $\hat{T}_{2,\pm2}$, as it cannot be obtained due to only relaxation.

2.2.4 Electric quadrupolar interaction

Besides magnetic dipolar moment, nuclei with spin > ½, or quadrupole nuclei like sodium, have an electric quadrupolar moment which originates from the non-spherical distribution of the electric charge in the nucleus. The energy of an interaction of the sodium nucleus with the surrounding electric field can be written in the multipole representation as in eq. [2.31] (Levitt, 2008):

$$E_{elec} = E_{elec}^{(0)} + E_{elec}^{(1)} + E_{elec}^{(2)} + \cdots, \qquad [2.31]$$

where $E_{elec}^{(n)}$ is defined by eq. [2.32]:

$$E_{elec}^{(n)} = \frac{1}{2}\int_V \rho^{(n)}(\vec{r})\, V^{(n)}(\vec{r})dV, \qquad [2.32]$$

where $\rho^{(n)}(\vec{r})$ is an electric charge density and $V^{(n)}(\vec{r})$ is an electric potential and n is an order of the derivative. The odd terms of $E_{elec}^{(n)}$ vanish due to the symmetry property of the parity conservation. This means that for all spin-1/2 nuclei, there is electric energy only associated with point charge approximation. This is not particularly important in NMR as it does not give information about the internal structure of the nucleus or its orientation in space. But for the spin systems with $I \geq 1$ the term $E_{elec}^{(2)}$ is particularly important. It represents an interaction of the quadrupolar moment of the nucleus with an electric field gradient (EFG) $V^{(2)}(\vec{r})$ (e.g., the gradient formed by electrons surrounding the nucleus in a molecule). The electric field gradient $V^{(2)}$ can be represented as a second-rank tensor with the components $V_{\alpha\beta}$ described by eq. [2.33]:

$$V_{\alpha\beta} = \left.\frac{\partial^2 V}{\partial\alpha\partial\beta}\right|_{r=0}. \qquad [2.33]$$

Then, a general quadrupolar Hamiltonian $\widehat{H}_Q$ can be given as in eq. [2.34]:

$$\widehat{H}_Q = \frac{1}{6}\sum_{\alpha,\beta} V_{\alpha\beta}\hat{Q}_{\alpha\beta}, \qquad [2.34]$$

where $\hat{Q}_{\alpha\beta} = e\sum_k\left[3x'_{\alpha k}x'_{\beta k} - r'^2_k\delta_{\alpha\beta}\right]$ is a tensor of an electric quadrupole moment of the nucleus which describes deviation of the charge distribution of a nucleus from a spherical symmetry, and $\alpha, \beta = x, y, z$; e is an elementary charge and summation is performed only over charged particles in the nucleus, i.e. protons.

The tensor of the electric potential $V_{\alpha\beta}$ is symmetric by definition. Principle axes can be found for V, that make cross-components vanish: $V_{\alpha\beta} = 0$ when $\alpha \neq \beta$. Furthermore, V must satisfy Laplace's equation: $\Delta V = 0$, which makes the potential traceless: $V_{xx} + V_{yy} + V_{zz} = 0$ (Slichter, 1996). A principal component of the electric field gradient tensor V_{zz} is usually defined as in eq. [2.35]:

$$V_{zz} = eq, \tag{2.35}$$

where q is a field gradient per unit of charge. An asymmetry parameter η can be designated as in eq. [2.36]:

$$\eta = \frac{V_{xx} - V_{yy}}{V_{zz}}, \tag{2.36}$$

and the quadrupolar Hamiltonian can be written as (eq. [2.37]):

$$\hat{H}_Q = \frac{eQV_{zz}}{4I(2I-1)}\left[3\hat{I}_z^2 - \hat{I}^2 + \eta\left(\hat{I}_x^2 - \hat{I}_y^2\right)\right]. \tag{2.37}$$

In the case of the electric field gradient with axial symmetry ($\eta = 0$) and a small quadrupolar interaction compared to the interaction of the nucleus with the external static magnetic field and considering eq. [2.30], the full Hamiltonian with the first-order quadrupolar interaction can be written as in eq. [2.38]:

$$\hat{H} = -\omega_0\hat{I}_z + \frac{eQV_{zz}}{4I(2I-1)}\left(3\hat{I}_z^2 - \hat{I}^2\right) = -\omega_0\hat{T}_{1,0} + \omega_Q^{(1)}\hat{T}_{2,0}, \tag{2.38}$$

where $\omega_Q^{(1)}$ is a first-order quadrupolar coupling and $\hat{T}_{2,0} = \frac{1}{\sqrt{6}}\left(3\hat{I}_z^2 - I(I+1)\hat{1}\right)$ is quadrupolar spin polarization (Madelin, Lee, et al., 2014). Energy levels will be described by the following equation [2.39] (Slichter, 1996):

$$\begin{aligned} E_m &= -\hbar\omega_0 m + \frac{e^2qQ}{4I(2I-1)} \cdot \frac{3\cos^2\theta - 1}{2} \cdot \left[3m^2 - I(I+1)\right] \\ &= -\hbar\omega_0 m + \hbar\omega_Q^{(1)}, \end{aligned} \tag{2.39}$$

where θ is an angle between the gradient of the electric field gradient and the magnetic field B_0. In eq. [2.38]-[2.39], the first term represents Zeeman splitting, and the second term is a first order quadrupolar interaction.

It is worth mentioning that the interaction of a nucleus with a magnetic field implies that it is so called external interaction as it originates from the “interaction” of an investigated sample with an NMR scanner. Meanwhile, the electric quadrupolar coupling is an internal interaction, as it comes from the internal properties of the sample itself. In NMR, the external interactions are usually much larger than the internal interactions.

For nuclei with spin > 1/2, electric quadrupolar interaction is the strongest among other internal interactions in solids and anisotropic liquids (in descending order): dipole-

dipole interaction, chemical shift anisotropy (CSA), and J-coupling (Levitt, 2008). Quadrupolar interaction is absent in isotropic liquids.

2.2.5 Quadrupole relaxation

In a sample, molecular tumbling causes fluctuating magnetic and electric fields, $B(t)$. The temporal evolution of these fields, i.e. the speed of their fluctuations, can be described by an autocorrelation function $G(\tau)$ defined in eq. [2.40] (Levitt, 2008):

$$G(\tau) = \overline{B(t)B(t+\tau)} \neq 0, \qquad [2.40]$$

where τ is an interval between two points in time under consideration. The bar above indicates an average over the ensemble of nuclei. If the fields are fluctuating very fast, the autocorrelation function rapidly decays to zero. It is accurate enough to assume the following form for $G(\tau)$ as in eq. [2.41]:

$$G(\tau) = \overline{B^2} e^{-\frac{|\tau|}{\tau_c}}, \qquad [2.41]$$

where τ_c is the correlation time that can characterize molecular motion. Rapid motions have a short correlation time, whereas slow motions have long τ_c. Thus, τ_c changes with temperature.

An important function in NMR is a Fourier transformation of $G(\tau)$, $J(\omega) + iK(\omega)$, which represents spectral densities of the time-varying fields (eq. [2.42]):

$$J(\omega) = \int_{-\infty}^{\infty} G(\tau) e^{-i\omega\tau} d\tau = A \frac{\tau_c}{1 + \omega^2 \tau_c^2}, \qquad K(\omega) = \omega \tau_c J(\omega), \qquad [2.42]$$

where A is the coefficient of normalization. These functions from eq. [2.42] present in an equation [2.43] of the time evolution of the density operator under the relaxation described by the quadrupolar Hamiltonian defined by eq. [2.38] (Van Der Maarel, 2003):

$$\frac{d\hat{\sigma}}{dt} = -i \frac{\omega_Q}{\sqrt{6}} \left[\hat{T}_{2,0}, \hat{\sigma}\right] - \sum_{m=-2}^{2} \left[\hat{T}_{2,m}, \left[\hat{T}_{2,m}^{+}, \hat{\sigma}\right]\right] \left(J_m(m\omega_0) + iK_m(m\omega_0)\right), \qquad [2.43]$$

where the index m coincides with the tensor's order. The part $K_m(m\omega_0)$ gives a small dynamic frequency shift but it is usually neglected as it is too small to measure experimentally.

In the case of the quadrupolar interaction with an axially symmetrical EFG tensor, the normalization coefficient A is equal to $(2\pi)^2 C_Q^2/60$ (Madelin, Lee, et al., 2014), where C_Q^2 is a quadrupolar coupling constant defined by eq. [2.44]:

$$C_Q^2 = \frac{e^2 qQ}{\hbar}. \qquad [2.44]$$

In the case of an isotropic environment with EFG averaged to zero, the first term in eq. [2.43] vanishes. Also, due to its symmetry properties, the double commutator gives decoupled equations for tensors of even and odd rank (Van Der Maarel, 2003). A solution for the spin polarization tensors $\hat{T}_{1,0}$ and $\hat{T}_{3,0}$ can be presented as in following equations [2.45]:

$$\begin{aligned} \hat{T}_{1,0} &\xrightarrow{R_{1,2}^{(0)}} \hat{T}_{1,0} f_{11}^{(0)} + \hat{T}_{3,0} f_{31}^{(0)}, \\ \hat{T}_{3,0} &\xrightarrow{R_{1,2}^{(0)}} \hat{T}_{1,0} f_{13}^{(0)} + \hat{T}_{3,0} f_{33}^{(0)}, \end{aligned} \qquad [2.45]$$

where the relaxation functions $f_{11}^{(0)}$, $f_{13}^{(0)}$, $f_{31}^{(0)}$, and $f_{33}^{(0)}$ are the following as in eq. [2.46] with the relaxation rates $R_1^{(0)}$ and $R_2^{(0)}$:

$$\begin{gathered} f_{11}^{(0)} = \frac{1}{5}\left(e^{-R_1^{(0)}t} + 4e^{-R_2^{(0)}t}\right), \qquad f_{33}^{(0)} = \frac{1}{5}\left(4e^{-R_1^{(0)}t} + e^{-R_2^{(0)}t}\right), \\ f_{13}^{(0)} = f_{31}^{(0)} = \frac{2}{5}\left(e^{-R_1^{(0)}t} - e^{-R_2^{(0)}t}\right), \\ R_1^{(0)} = 2J_1, \qquad R_2^{(0)} = 2J_2, \end{gathered} \qquad [2.46]$$

where the spectral density functions have notations: $J_1 = J_1(\omega_0)$ and $J_2 = J_2(2\omega_0)$, and the superscript (0) indicates ‘zero-quantum’, longitudinal relaxation.

From the eq. [2.45], it can be seen that the longitudinal magnetization $\hat{T}_{1,0}$ and octopolar spin polarization $\hat{T}_{3,0}$ are coupled and the longitudinal relaxation is biexponential with relaxation times T_1' and T_1'' (eq. [2.47]):

$$T_1' = \frac{1}{R_1^{(0)}} \ (20\%), \qquad T_1'' = \frac{1}{R_2^{(0)}} \ (80\%). \qquad [2.47]$$

Time evolution of single quantum coherences $\hat{T}_{1,\pm 1}$ and $\hat{T}_{3,\pm 1}$ is given as in eq. [2.48]:

$$\hat{T}_{1,\pm1} \xrightarrow{R^{(1)}} \hat{T}_{1,\pm1} f_{11}^{(\pm1)} + \hat{T}_{3,\pm1} f_{31}^{(\pm1)},$$
$$\hat{T}_{3,\pm1} \xrightarrow{R^{(1)}} \hat{T}_{1,\pm1} f_{13}^{(\pm)} + \hat{T}_{3,\pm1} f_{33}^{(\pm1)}, \qquad [2.48]$$

with the following biexponential relaxation functions as in eq. [2.49]:

$$f_{11}^{(\pm1)} = \frac{1}{5}\left(3e^{-R_1^{(\pm1)}t} + 2e^{-R_2^{(\pm1)}t}\right),$$
$$f_{33}^{(\pm1)} = \frac{1}{5}\left(2e^{-R_1^{(\pm1)}t} + 3e^{-R_2^{(\pm1)}t}\right),$$
$$f_{13}^{(\pm1)} = f_{31}^{(\pm1)} = \frac{\sqrt{6}}{5}\left(e^{-R_1^{(\pm1)}t} - e^{-R_2^{(\pm1)}t}\right), \qquad [2.49]$$
$$R_1^{(\pm1)} = J_0 + J_1, \qquad R_2^{(\pm1)} = J_1 + J_2,$$

where in $R_{1,2}^{(\pm1)}$ the terms of dynamic shift are omitted because their contributions can be neglected. The spin-spin relaxation is also shown to be biexponential with its short and long components as in eq. [2.50]:

$$T_{2short} = \frac{1}{R_1^{(\pm1)}}\ (60\%), \qquad T_{2long} = \frac{1}{R_2^{(\pm1)}}\ (40\%). \qquad [2.50]$$

Time evolutions of the quadrupolar spin polarization tensor $\hat{T}_{2,0}$ and rank-two SQ coherence $\hat{T}_{2,\pm1}$ are not shown, as they cannot be created either by RF pulse or relaxation in the isotropic environment. Therefore, their relaxation rates are unavailable.

In the case of an anisotropic environment, even and odd rank tensors are no longer decoupled. Full equations for the tensors and their solutions are provided in (Van Der Maarel, 2003), but expressions for the longitudinal relaxation are still the same as for the isotropic case (eq. [2.45]-[2.47]). However, for the transverse relaxation in the case of $\omega_Q \gg J_2$, the relaxation functions can be slightly simplified as shown in eq. [2.51] (Reddy, Li, et al., 1997; Van Der Maarel, 2003):

$$f_{11}^{(1)} = \frac{1}{5}\left(\frac{3}{2}e^{-\left(R_s^{(1)} - i\omega_Q\right)t} + 2e^{-R_c^{(1)}t} + \frac{3}{2}e^{-\left(R_s^{(1)} + i\omega_Q\right)t}\right)$$
$$= \frac{1}{5}\left(3e^{-R_s^{(1)}t}\cos\left(\omega_Q t\right) + 2e^{-R_c^{(1)}t}\right), \qquad [2.51]$$

$$f_{12}^{(1)} = f_{21}^{(1)} = \frac{1}{2}\sqrt{\frac{3}{5}}\left(e^{-\left(R_s^{(1)}-i\omega_Q\right)t} - e^{-\left(R_s^{(1)}+i\omega_Q\right)t}\right)$$

$$= i\sqrt{\frac{3}{5}}e^{-R_s^{(1)}t}\sin\left(\omega_Q t\right),$$

$$f_{13}^{(\pm1)} = f_{31}^{(\pm1)} = \frac{\sqrt{6}}{5}\left(\frac{1}{2}e^{-\left(R_s^{(1)}-i\omega_Q\right)t} - e^{-R_c^{(1)}t} + \frac{1}{2}e^{-\left(R_s^{(1)}+i\omega_Q\right)t}\right)$$

$$= \frac{\sqrt{6}}{5}\left(e^{-R_s^{(1)}t}\cos\left(\omega_Q t\right) - e^{-R_c^{(1)}t}\right),$$

$$f_{22}^{(1)} = \frac{1}{2}\left(e^{-\left(R_s^{(1)}-i\omega_Q\right)t} + e^{-\left(R_s^{(1)}+i\omega_Q\right)t}\right),$$

$$f_{23}^{(1)} = f_{32}^{(1)} = \frac{1}{\sqrt{10}}\left(e^{-\left(R_s^{(1)}-i\omega_Q\right)t} - e^{-\left(R_s^{(1)}+i\omega_Q\right)t}\right),$$

$$f_{33}^{(1)} = \frac{1}{5}\left(e^{-\left(R_s^{(1)}-i\omega_Q\right)t} + 3e^{-R_c^{(1)}t} + e^{-\left(R_s^{(1)}+i\omega_Q\right)t}\right),$$

with relaxation eigenvalues as in eq. [2.52]:

$$R_s^{(1)} = J_0 + J_1 + J_2, \qquad R_c^{(1)} = J_1 + J_2. \tag{2.52}$$

$R_s^{(1)}$ and $R_c^{(1)}$ are the relaxation rates of the satellites and the central transition correspondingly. It is worth noting that they are different from $R_1^{(\pm1)}$ and $R_2^{(\pm1)}$ in the isotropic case. Depending on the molecular system, $R_1^{(\pm1)}$ and $R_s^{(1)}$ are equal to $1/T_{2short}$, where T_{2short} is a short relaxation time, and $R_2^{(\pm1)}$, $R_c^{(1)}$ are equal to $1/T_{2long}$, where T_{2long} is a long relaxation time.

This thesis is focused on sodium behaviour in biological tissues. Typical ranges of sodium concentrations and relaxation times in some human tissues *in vivo* and some types of sodium solutions are given in Table 2.2.

It should be noted that sodium relaxation times in biological samples and aqueous solutions are distributed in a relatively wide range (from 12 to 73 ms for T_1, 0.46-6.3 ms for T_{2short} and 5-60 ms for T_{2long}) (Constantinides et al., 2000). However, T_1 appears to be more than one order less than longitudinal relaxation time for protons. It has its advantages and drawbacks. Short T_1 is beneficial for NMR signal acquisition as it allows more signal averages per unit of time. Short transverse relaxation times,

Table 2.2. Sodium concentrations and T_1, T_2 values for some human tissues and some types of sodium water solutions (adapted from (Constantinides et al., 2000; Madelin, Lee, et al., 2014)). [1](Buist et al., 1991), ND – no data.

Tissue or sample	[Na$^+$], mM	T_1, ms	T_{2short}, ms	T_{2long}, ms	Magnetic field, T
Articular cartilage	250-350	14-20	0.7-2.3	8-12	1.5
		ND	1.0±0.1	12±1	1.5
Blood plasma (human)	140-150	30.8±1.3	ND	17±1	4.7
NaCl					
Aqueous solution	20	ND	ND	58.7	1.5
	80[1]	57	ND	54	7.05
In deionized water	100	60	ND	60	4.7
Aqueous solution	140	54	ND	54	8.5
In deionized water	1000	53±2	ND	54±3	1.5
Saline solution		71±5	ND	57±7	8.3
		52.9±1.4	ND	54±3	1.5

on the other hand, could cause a loss of more than half of the signal (eq. [2.50]). Different methods should be considered to overcome these difficulties.

2.2.6 Types of electric quadrupolar interaction

Depending on the nuclear environment characterized by a molecular motion, four types of a single quantum spectrum might be obtained for spin-3/2 nuclei like sodium (Rooney & Springer, 1991b):

- Type "d" environment, also called an "extreme narrow" limit. This is usually observed in homogeneous NaCl water solutions. Fluctuations of ω_Q are very rapid, such as $\tau_c \ll 1/\omega_0$, consequently, $\omega_0\tau_c \ll 1$. Quadrupolar interaction averages to zero over time, $\overline{\omega}_Q = 0$, and it does not affect the energy levels of the nucleus (Figure 2.6). Three SQ coherences can be observed which give rise to one narrow spectrum line. Both longitudinal and transverse relaxation decays are monoexponential with relaxation times as in eq. [2.53] (Farrar & Becker, 1971):

$$\frac{1}{T_1'} = \frac{1}{T_1''} = \frac{1}{T_{2short}} = \frac{1}{T_{2long}} = \frac{1}{10}\left(\frac{e^2qQ}{\hbar}\right)^2 \tau_c. \qquad [2.53]$$

- Type “c” environment consists of two subtypes:
  - The environment is homogeneous, but the motions of the nuclei are slowed down. An aqueous solution of solubilized micelles may serve as an example. Thus, the correlation time $\tau_c \approx 1/\omega_0$ ($\omega_0\tau_c \approx 1$), but it is still shorter than $1/\bar{\omega}_Q$. A central ($\left|\frac{1}{2}\right\rangle \to \left|-\frac{1}{2}\right\rangle$) coherence is overlapped with two satellite coherences ($\left|\frac{3}{2}\right\rangle \to \left|\frac{1}{2}\right\rangle$ and $\left|-\frac{1}{2}\right\rangle \to \left|-\frac{3}{2}\right\rangle$) with the relaxation time of the latter, T_{2short}, being much shorter than one of the former, T_{2long}. Hence the spectrum line is generally broadened (Figure 2.6). For a single pool of sodium ions, T_{2short} and T_{2long} have 60 and 40% contributions respectively (Burstein & Springer, 2019). Relaxation rates are equal to (eq. [2.54]) (Madelin, Lee, et al., 2014):

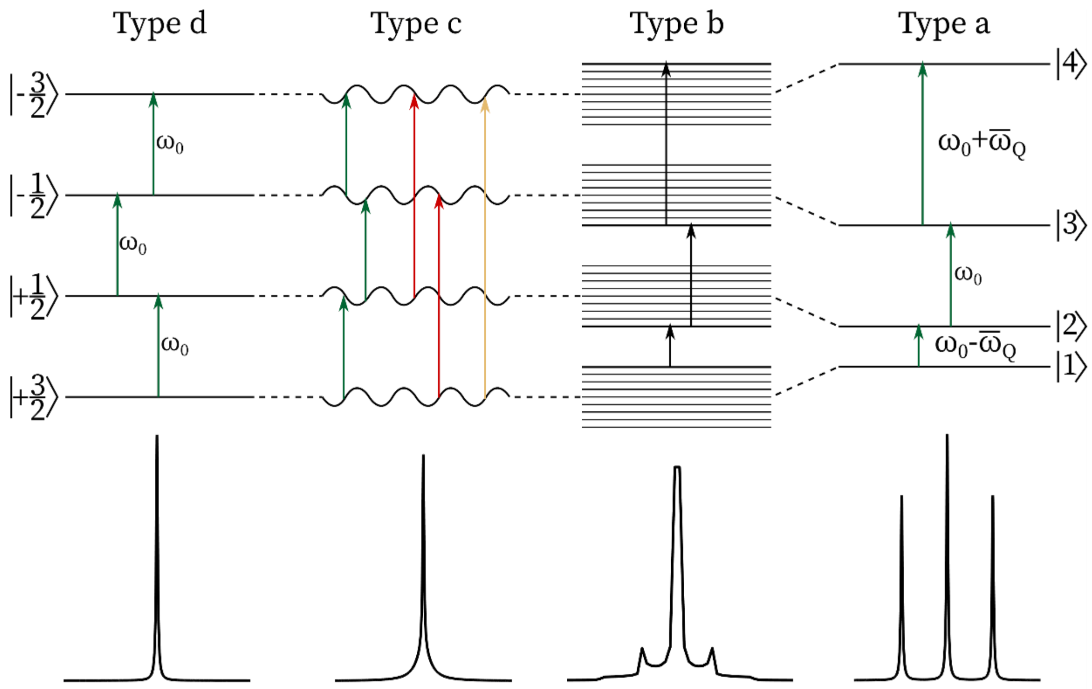

Figure 2.6. Energy level diagrams of a spin-3/2 system in four different molecular environments (“a”, “b”, “c” and “d”). Corresponding simulated spectra are shown below each diagram. Description of the types can be found in the text. Colours of the arrow mean the same as in Figure 2.2. Adapted from (Rooney & Springer, 1991b).

$$R_1^{(0)} = \frac{1}{T_1'} = 2J_0, \qquad R_2^{(0)} = \frac{1}{T_1''} = 2J_1,$$

$$R_1^{(\pm 1)} = \frac{1}{T_{2short}} = J_0 + J_1, \tag{2.54}$$

$$R_2^{(\pm 1)} = \frac{1}{T_{2long}} = J_1 + J_2.$$

In this case, multiple quantum (MQ) coherences can be generated.

- The environment possesses a slow motion along with a partial alignment ($\omega_0 \tau_c > 1$). Such environment can be found, for example, in biological tissues. The presence of negatively charged large macromolecules slows down the fluctuations of $\bar{\omega}_Q$ of sodium ions. The relaxation rates of the SQ coherences are the following expressions as in eq. [2.55] (Madelin, Lee, et al., 2014; Van Der Maarel, 2003):

$$R_1^{(\pm 1)} = J_0 + J_1 + J_1 \pm \sqrt{J_2^2 - \bar{\omega}_Q^2},$$
$$R_2^{(\pm 1)} = J_1 + J_2. \tag{2.55}$$

  In this case, $\bar{\omega}_Q < J_2$, therefore, both relaxation rates are real numbers. A spectrum consists of three overlapping Lorentzians, as there is no splitting. As is the previous case, MQ coherences can be observed.

- Type “b” environment can be characterized by the correlation time τ_c which is longer than $1/\bar{\omega}_Q$. The nuclei are located in domains with different orientations of $\bar{\omega}_Q$. This gives rise to a powder-like spectrum: central sharp resonance is superimposed with “powder patterns” from the satellite resonances (Figure 2.6). The relaxation eigenvalues are still defined by eq. [2.55], but in this case $\bar{\omega}_Q > J_2$. They are complex, but relaxation rates are defined by real parts of the eigenvalues. Satellite peaks are shifted from the central peak by $\pm\sqrt{\bar{\omega}_Q^2 - J_2^2}$. Such spectrum can be obtained, for example, from a water suspension of unoriented cylindrical micelles (Rooney et al., 1988).
- Type “a” environment can be called a crystal-like system: it is characterized by anisotropy on a macroscale and the quadrupolar interaction $\bar{\omega}_Q$ is not

fluctuating anymore – it has a specific positive value all the time and $\bar{\omega}_Q \gg J_2$. This leads to a permanent shift of the energy levels by $\bar{\omega}_Q$ (but the energy difference between $\left|\frac{1}{2}\right\rangle \rightarrow \left|-\frac{1}{2}\right\rangle$ levels does not change) and three distinguished spectral lines with 3:4:3 intensities and $2\bar{\omega}_Q$ distance between them (Figure 2.6). Relaxation rates are defined as $R_s^{(1)}$ and $R_c^{(1)}$ in eq. [2.52]. With reduced water content in the water suspension due to ageing, cylindrical micelles became oriented forming a liquid crystal which can give the spectrum described above (Rooney et al., 1988).

In the case of slow motion with biexponential relaxation observed (type "c"), MQ coherences can be created and selectively detected with the help of multiple quantum-filtered sequences (Navon et al., 2001; Wimperis & Wood, 1991), thereby providing additional opportunities for the identification of sodium which is involved in binding with macromolecules.

A type "c" spectrum was observed in a 44% (w/w) solution of bovine serum albumin in NaCl solution and a concentrated suspension of Na^+-loaded yeast cells for both the intracellular and extracellular sodium (Rooney & Springer, 1991a). Shinar et al. studied sodium in mammalian and human red blood cells (Shinar et al., 1993). They found that sodium anisotropic movement arises from interaction with the intact cytoskeletal network consisting mainly of the spectrin and actin proteins. This study is in agreement with (Tauskela & Shoubridge, 1993) that the value of residual quadrupolar interaction $\bar{\omega}_Q$ is small, about 22 Hz, and it is related to at least one population of sodium ions inside the cells that gives the type "b" spectrum. But because $\bar{\omega}_Q$ is less than a linewidth, it looks like the type "c" spectrum. The biconcave discoid shape of erythrocytes compared to the spherical yeast cells is responsible for incline towards the sodium type "b" spectrum in the former.

A type "b" spectrum was found in bovine nasal cartilage with a residual splitting $\bar{\omega}_Q \approx 270$ Hz (Eliav & Navon, 1994). Investigation of hydrated collagen fibre powder showed that it gave an even broader type "b" spectrum than the cartilage. On the other hand, quadrupolar splitting does not manifest in gelatine (denatured collagen in a soluble form) and chondroitin sulphate separately suggesting that the left-handed helical conformation of collagen is responsible for creating a microscopic order experienced by sodium spins (Eliav & Navon, 1994).

3 Sodium NMR of the human skin in 9.4 T

Experiments presented in this Chapter were performed by Dr G. Pavlovskaya at the Sir Peter Mansfield Imaging Centre at the University of Nottingham. Dr G. Pavlovskaya also developed the original concept and the design of the scanning protocol. An analysis of CPMG data were initially performed in collaboration and presented at an international meeting: Fomina D. V., Sadykhov E. G., Hanson P., Philp C. J., Randeva H. S., O’Hare J. P., Pavlova O. S., Anisimov N. V, Makurenkov A. M., Pirogov Y. A., Barber T. M., Meersmann T., & Pavlovskaya G. E. (2021). Sodium NMR relaxation times of human skin as potential biomarkers for Type 2 Diabetes Mellitus. *Proc. Intl. Soc. Mag. Reson. Med. 29*, 1791 (Fomina et al., 2021). MQF data were analysed by Mrs. Daria Fomina using previously published methodology (Eliav & Navon, 2016b). Statistical analysis of all experimental data was performed by Mrs Daria Fomina.

3.1 Introduction

3.1.1 The biological role of sodium

In biological tissues sodium is located in two environments: within the cells (intracellular sodium with a concentration of 5-15 mM) and out of the cells in the extracellular matrix (concentration 140-150 mM) (Alberts et al., 2015). The intracellular fluid constitutes approximately 60-70% of the tissue volume and the extra-cellular fluid volume fraction (including the vascular compartment) accounts for the rest (Guyton & Hall, 2006). In healthy tissues, cells maintain this large gradient of sodium concentration between the intracellular and extracellular compartments across the cell membrane. The sodium flux in and out of cells is supported by several kinds of transport proteins but most importantly by the Na^+/K^+-ATPase (Figure 3.1) (Skou & Esmann, 1992).

The Na^+/K^+-ATPase is a protein complex associated with the plasma membrane of every cell in living organisms. By pumping three sodium ions (Na^+) out of the cell and two potassium ions (K^+) into the cell in one cycle, it maintains the electrochemical gradients of these ions across the membrane that requires energy provided by adenosine triphosphate (ATP) hydrolysis (Michael Burnier, 2007). The sodium electrochemical gradient plays a vital role in protecting the cell from rupture due to osmotic pressure and also induces an electric potential that is used for transmitting

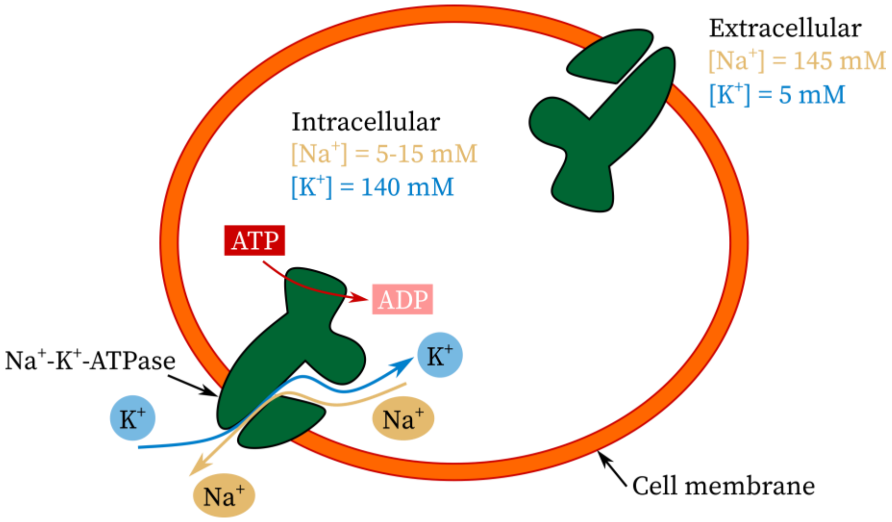

Figure 3.1. A diagram of the Na^+-K^+-ATPase.

nerve impulses and for transferring ions (such as protons, chloride, calcium, and phosphate), metabolites and nutrients (such as glucose and amino acids) and neurotransmitters (such as glutamate) across the cell membrane through different types of sodium-dependent transporters (Gagnon & Delpire, 2021). Therefore, disruption of the transporters which highly depend on the electrochemical gradient created by the Na^+/K^+- ATPase leads to a wide variety of pathological conditions. For example, a lack of ATP reduces a function of the Na^+/K^+-ATPase that increases the intracellular sodium concentration (Gagnon & Delpire, 2021; Murphy & Eisner, 2009). Excessive Na^+ may lead to tissue hypertrophy or cell death (Barros et al., 2002).

3.1.2 Sodium in the skin

Total body sodium has been compartmentalized into intracellular (IC) and extracellular (EC) sodium, the latter divided into intravascular (IV) and interstitial sodium (Bhave & Neilson, 2011). With an increase in salt intake, it was believed that sodium accumulates in the EC space followed by attraction of water due to the phenomenon of osmosis. However, a study (Olde Engberink et al., 2017) has shown that in healthy humans sodium content in the urine was about twice lower than the expected amount after infusion with hypertonic saline. It means that there might be non-osmotic storage of sodium in the body – in an additional third compartment.

The skin might serve as a potential depot of sodium. The skin consists of several tissue types: epidermis, dermis and hypodermis (or subcutaneous tissue) (Figure 3.2(a)). The epidermis is an external epithelium of a layered structure, which does not contain blood vessels, with a width in a range of 75-150 µm (up to 600 µm on palms/soles)

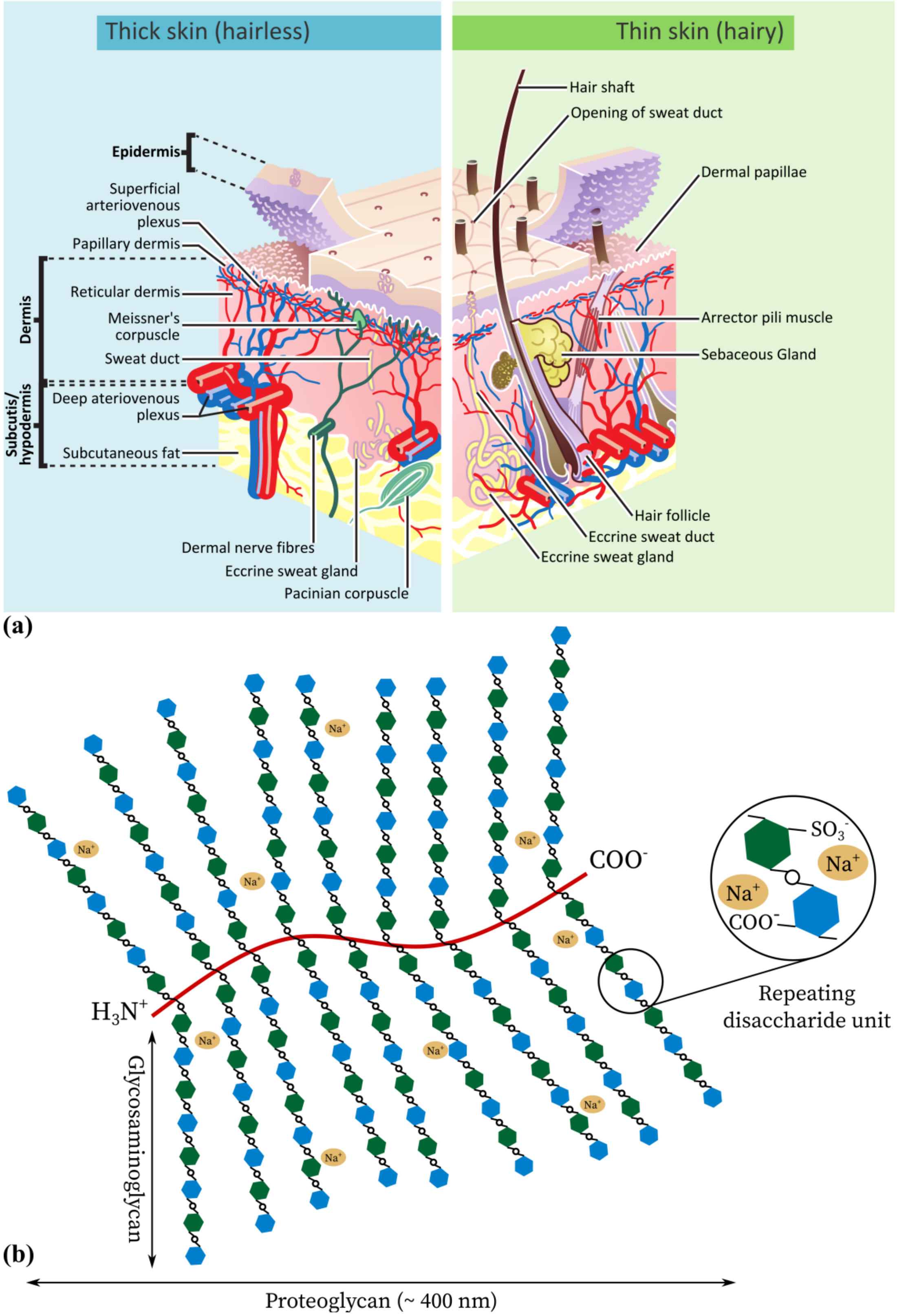

Figure 3.2. (a) Skin layers and structures within. Image is taken from (Madhero88 & Komorniczak, 2012). No modifications to the image were made. (b) A diagram of a typical proteoglycan in the skin dermis (adapted from (Nijst et al., 2015)).

(Tobin, 2006). The dermis is 2-4 mm thick and is considered a connective tissue. A significant portion of its volume is made up of a fibrous extracellular matrix (ECM) which consists of collagens (mainly types I, III and V) (Smith & Melrose, 2015), elastic fibres, and an extrafibrillar matrix consisting of about 75% of water (Téllez-Soto et al., 2021), glycoproteins, and proteoglycans. ECM is interspersed between vascular, lymphatic and neural networks and much fewer cells – fibroblasts. The fibroblasts are responsible for the production and degradation of the ECM components. The proper formation and maintenance of a normal, healthy collagen matrix alignment in the ECM depend on specific proteoglycans. Proteoglycans are formed by the binding of a protein to glycosaminoglycans (GAGs) (Figure 3.2(b), (Comper & Laurent, 1978)). GAGs are big (hundreds of kDa) polysaccharides with a negative charge provided mainly by sulphate groups, able to bind water and ions. Some physiologically important GAGs include dermatan sulphate, chondroitin sulphate, keratin sulphate, heparan sulphate, heparin, and hyaluronic acid (HA) (Smith & Melrose, 2015). HA is one of the GAGs that is not attached to any protein (Anderegg et al., 2014). A foundation of the dermis is the subcutaneous tissue or hypodermis. The subcutaneous layer, also known as the subcutis, is a skin layer abundant in adipose tissue and serves as a reserve for energy and fluids and as a support for the epidermis and dermis. Within the subcutis, there are clusters of fat cells called lipocytes or adipocytes, which are arranged into lobules separated by fibrous connective tissue called septa. Nerves, blood vessels, and lymphatic vessels emerge into the septa (Ita, 2020).

An abundance of PGs in the skin dermis (for example, decorin, biglycan (Li et al., 2013) and versican (Zimmermann et al., 1994) confirmed by immunostaining of the skin) and their GAGs and HA (Oh et al., 2011) can provide a significant negative charge density capable of binding sodium. In rats, it was found that Na^+ may be stored osmotically inactive in the skin (without water accumulation) which increases the total skin sodium concentration and its storage may be regulated by changing the degree of GAGs' polymerization (Titze et al., 2004). In humans, it was shown that skin sodium content increases with NaCl loading in a diet (Selvarajah et al., 2017) similar to the animal study mentioned previously. Discoveries like these led to a current change in a paradigm from an exclusively renal control of sodium homeostasis to an addition of extrarenal regulation represented by skin being a "third compartment" with the adjustable ability of sodium storage in response to altering salt intake (Selvarajah et al., 2018).

The mechanism of sodium accumulation in the skin needs to be explored. To achieve skin, firstly sodium needs to pass through the intestine wall to the bloodstream. Sodium can be transferred from the intestinal lumen to enterocytes by either a co-transport represented by sodium-glucose like transporters 2 – SGLT-2 (Wright et al., 2011), glucose transporters – GLUT, and Na^+/H^+ exchangers (Gurney et al., 2017) or by a passive transport through sodium channel ENaC (Cuppoletti & Malinowska, 2012). Later it is excreted to the ECF by Na^+/K^+ ATF-ase. After, sodium can diffuse into the capillaries to travel around the whole body to reach the skin interstitium. However, it is still unclear how sodium gets into the skin (Selvarajah et al., 2018). Two hypotheses exist: first is that skin can serve as a sodium depot to prevent vascular damage. On the other hand, an accumulation of sodium in the skin may be a consequence of vascular damage. Future investigations are required.

3.1.3 Sodium NMR as a diagnostic tool

As an alteration of local sodium concentration is an indicator of cell viability in an investigated region of biological tissue, sodium magnetic resonance imaging (^{23}Na MRI) has been implemented on a range of human organs *in vivo* to visualize them with and without different pathologies (Madelin, Lee, et al., 2014). An observed sodium concentration in a tissue is usually a weighted average of intra- and extracellular sodium concentrations. Some impairments are usually characterized by increased sodium content. For example, in patients with multiple sclerosis tissue sodium concentration (TSC) in lesions is significantly higher than in white matter that appears normal, but also TSC in the white and grey matter of the patients is much higher than that in healthy volunteers (Inglese et al., 2010). Several brain tumours (different grades of oligodendroglioma and astrocytoma) were studied and they all showed a significantly elevated sodium level on ^{23}Na MRI (Ouwerkerk et al., 2003). Application of sodium T_1 or T_2^* relaxation weighted imaging in addition to the regular ^{23}Na spin-density weighted imaging reveals a deeper characterization of brain tumours compared to the spin-density weighted imaging only (Nagel et al., 2011): tumours of the WHO grade IV could be differentiated from ones of the WHO grade I-III.

It was determined that the elevated sodium level is also associated with malignancy of breast lesions (Ouwerkerk et al., 2007). The mean tissue TSC in the case of myocardial infarctions is higher than in healthy cases (Ouwerkerk et al., 2008).

Sodium MRI was shown to be suitable for measuring a corticomedullary sodium gradient in a human kidney to assess its functionality (Maril et al., 2006; Rosen & Lenkinski, 2009). The gradients increased significantly in water deprivation conditions compared to normal ones (Maril et al., 2006). A sodium spatial distribution map was obtained for a human prostate which can serve as an indicator for prostate cancer prediction in the future (Hausmann et al., 2012). Sodium MRI was successfully used to evaluate GAG content in cartilage and its loss in osteoarthritis, and estimate the effectiveness of different tissue repair procedures after injuries (Zbýň et al., 2014). Fluid-suppressing techniques allow one to eliminate contamination from the synovial fluid in the determination of sodium concentration in the cartilage.

Multiple quantum filtering techniques (spectroscopy and imaging) allow one to detect MQ coherences that can only be generated by slow and/or anisotropically moving sodium ions ($\tau_c > 1/\omega_0$). Therefore, they were also shown to be sensitive to different organ pathologies, especially those associated with structural degradation. The apparent short component of sodium T_2, T_{2short} (affected by tissue anisotropy), measured by ^{23}Na TQF spectroscopy in a muscle was significantly longer in patients with myotonic dystrophy (MyD) compared to controls (Kushnir et al., 1997). Also, the total sodium content measured as a ratio of ^{23}Na to ^{1}H (water) signals in the MyD patients increased by up to two-fold and its combination with T_{2short} is a sensitive marker of the disease severity. Sodium T_{2short} and quadrupolar interaction ν_Q ($= \omega_Q/2\pi$) were studied in osteoarthritic (OA) and osteoporotic (OP) cartilage (Keinan-Adamsky et al., 2010). Sodium quadrupolar interaction was found to be increased in the OA cartilage relative to controls. For the OP cartilage, ν_Q together with $1/T_{2short}$ were significantly larger than for control and the OA cartilage. The measured effects might be explained by the depletion of PG (Borthakur et al., 2002) and decalcification in OA and OP correspondingly. Analysis of the DQF and DQF-MA behaviour vs creation time τ of sodium from annulus fibrosus and nucleus pulposus of a spinal disc might serve as a diagnostic tool for detecting a degeneration of the disc (Ooms et al., 2008).

In cartilage, TQF imaging allows one to exclude sodium signals from surrounding tissues like synovial fluid, blood and bone marrow (Borthakur et al., 1999; Reddy, Insko, et al., 1997). During ischemic stroke, using SQ and TQ ^{23}Na MRI a time window can be established during which the tissue damage is reversible by treatment (F. E. Boada et al., 2012). However, as the TQF technique is very sensitive to RF and magnetic field inhomogeneities, a method was proposed to separate intra- and extra-cellular sodium using ^{23}Na MRI with the help of ^{1}H double inversion recovery MRI (Madelin, Kline, et al., 2014).

3.1.4 Sodium NMR in the skin

Sodium magnetic resonance imaging and spectroscopy were used to investigate sodium content in the skin in health and disease. Using ^{23}Na MRI, it was found that men had higher sodium content in the skin than in the muscle, with the opposite result for women, and this difference increases with age (Kopp et al., 2012; Wang et al., 2017). Skin sodium concentration was shown to be an indicator of some pathological conditions. Refractory hypertension was associated with skin Na^+ accumulation and skin sodium content increases with age in both healthy men and women (Kopp et al., 2013). Dahlmann et al. also supported the latter finding, additionally showing the same results in patients with end-stage renal disease (ESRD) undergoing haemodialysis (HD) (Dahlmann et al., 2015). Furthermore, they demonstrated that sodium can be partially removed from the skin by HD and the patients with a higher amount of VEGF-C factor (vascular endothelial growth factor C) in the plasma ended up with lower tissue sodium concentration after the treatment. HD patients over 60 years old had an elevated level of skin sodium compared to age-matched healthy controls (Dahlmann et al., 2015). It was also found that higher blood pressure and left ventricular hypertrophy (LVH) are positively correlated with increased skin sodium content in patients with CKD (Schneider et al., 2017). Sodium was found to be increased in the fibrotic skin of patients with systemic sclerosis (SSc) compared with skin from controls and non-fibrotic SSc skin (Kopp et al., 2017). In patients with acute heart failure, sodium content in the skin successfully decreased after treatment with a diuretic without a change in the water content of the tissue (Hammon et al., 2015). This finding supports the hypothesis that sodium might be stored non-osmotically in the skin.

To support MRI data, chemical analysis of skin tissue should be performed. Analytical methods such as inductively coupled plasma optical emission spectrometry (ICP-OES), flame photometry and so on, are very powerful for the estimation of the content of different elements in biological samples (Grochowski et al., 2019; Kopp et al., 2012; Selvarajah et al., 2017; Titze et al., 2004). Na^+ concentration was determined in the human skin, muscle and artery and compared with GAGs' content (Fischereder et al., 2017). Elevated skin and arterial sodium levels are associated with increased GAGs' content, supporting an earlier study in animals (Titze et al., 2004).

Sodium in the skin has been studied by NMR relatively rarely compared to other organs, partially because the skin is a very thin tissue and high resolution (< 0.5 mm) is required to visualize it using sodium MRI. This requires high magnetic fields and coil designs developed specifically for certain positioning on the human body (Linz et al., 2014). Blood sodium concentrations alone do not give a full picture of the sodium distribution in the body to monitor certain conditions (Kopp et al., 2013). Therefore, studying sodium NMR relaxation in the skin is of particular interest in this thesis.

3.1.5 Type 2 Diabetes Mellitus

Diabetes is a long-term metabolic disorder characterized by the inability of the body to produce insulin or the inability of cells to respond to insulin which leads to a significant increase in blood glucose levels. It is estimated that 537 million people between the ages of 20 to 79 years worldwide have Diabetes (IDF, 2021). If unmanaged, high glucose levels usually result in serious, life-threatening complications such as cardiovascular diseases, peripheral neuropathy, kidney failure, blindness, and amputation of lower limbs. Fortunately, Diabetes can be controlled by appropriate medicine, diet and exercise, which can increase the quality of life and prevent complications (IDF, 2021).

There are two main types of Diabetes: (1) type 1 Diabetes which is an autoimmune disease when insulin-producing beta-cells of the pancreas are being destroyed, and (2) type 2 Diabetes (T2DM) which is mainly caused by insulin resistance. The prevalence of type 2 Diabetes is about 90%. It is not completely understood what triggers the development of type 2 Diabetes but there is a strong connection with obesity and overweight, increasing age, ethnicity, family history, and polygenic and environmental factors (IDF, 2021).

Cases of both non-insulin-dependent type 1 and type 2 Diabetes can be characterized by sodium retention that leads to hypertension and kidney failure (Rose & Valdes Jr, 1994; Weidmann & Ferrari, 1991). Sodium retention can be mainly caused by two mechanisms: (1) insulin-dependent mechanism through stimulation of the renal tubular Na^+/K^+-ATPase and (2) insulin-independent mechanism due to hyperglycaemia that results in hyperfiltration of glucose in glomeruli which stimulates a sodium-glucose like transporter 2 (SGLT2) in a proximal tubule of the kidney. To regulate blood glucose levels in Diabetes, SGLT2 has become a major target of drug developers (Wright et al., 2011). Impairment of sodium homeostasis might play an important role in the development of type 2 Diabetes.

Skin sodium content in T2DM has been studied by sodium MRI. As mentioned earlier, sodium in the skin and muscle was found to be increased in arterial hypertension (Kopp et al., 2013). In patients with T2DM, there is an even higher sodium content in both tissues compared with non-diabetic hypertensive subjects (Kannenkeril et al., 2019). Haemodialysis (HD) patients with type 2 Diabetes Mellitus also had higher skin sodium content in comparison to participants on HD but without T2DM (Kopp et al., 2018). With *ex vivo* skin samples from control and T2DM patients, using ^{23}Na GE and TQF MRI, it was shown that free and bound sodium are located in the dermis of the skin; diabetic patients accumulate more free sodium but less bound sodium, which indicates that the sodium binding capacity of their skin is reduced compared to controls (Hanson et al., 2021). Therefore, T2DM can be characterized as a condition with a heavy sodium overload but reduced buffering function of the skin which leads to renal and cardiovascular complications (Hanson et al., 2022).

3.1.6 Registration of SQ and MQ coherences

A typical pulse sequence for detecting the sodium coherences with the rank $l > 1$ (DQ or TQ coherences) usually consists of three pulses θ_1, θ_2, and θ_3 with corresponding phases φ_1, φ_2, and φ_3, and can be described by the following equation [3.1] (Navon et al., 2001):

$$\theta_1(\varphi_1) - \tau - \theta_2(\varphi_2) - t_{MQ} - \theta_3(\varphi_3) - t_{acq}. \qquad [3.1]$$

The pulse sequence is depicted graphically in Figure 3.3. Firstly, SQ coherences ($\hat{T}_{1,\pm1}$) are generated by the first pulse $\theta_1 = 90°$. During an evolution time τ, SQ coherences of the higher rank can be formed: in isotropic media, only odd rank

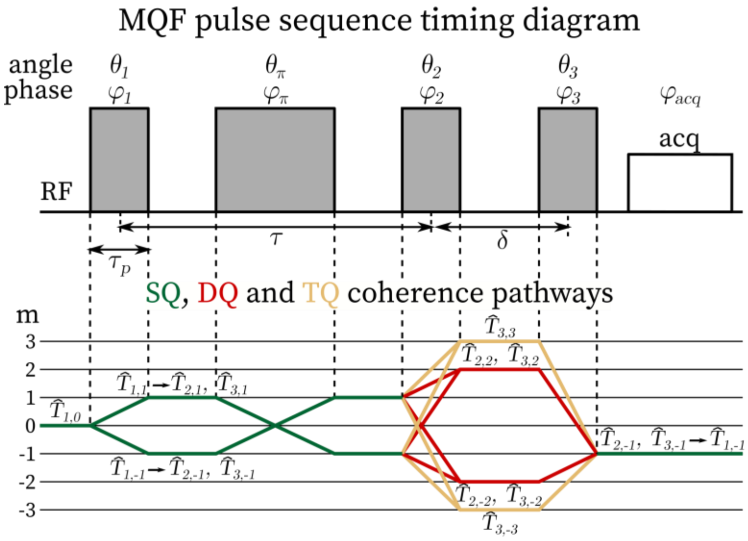

Figure 3.3. Timing diagram of a general pulse sequence to excite DQ and TQ coherences. Corresponding coherence pathways are shown underneath.

coherences described by the tensor $\hat{T}_{3,\pm1}$ develop under the quadrupolar relaxation; in the anisotropic media in the presence of non-zero quadrupolar interaction, odd rank tensors $\hat{T}_{2,\pm1}$ can occur as well. In the middle of τ, a $\theta_\pi = 180°$ pulse can be applied to refocus magnetic field inhomogeneities and chemical shifts. After the θ_2 pulse, high-rank SQ coherences are transformed into DQ and TQ coherences ($\hat{T}_{2,\pm2}$, $\hat{T}_{3,\pm2}$, and $\hat{T}_{3,\pm3}$) which evolve during the evolution time, t_{MQ}. As MQ coherences cannot be detected directly, the third pulse θ_3 is applied to convert them back to $\hat{T}_{2,-1}$, $\hat{T}_{3,-1}$ which then during evolution time develop under the influence of relaxation or quadrupolar interaction into the observable coherence $\hat{T}_{1,-1}$ which can be detected during the acquisition time t_{acq}. Different orders of coherences can be detected by choosing combinations of flip angles of RF pulses and the phase cycle. As in the case of non-vanishing quadrupolar interaction, the tensors $\hat{T}_{2,\pm2}$ and $\hat{T}_{3,\pm2}$ are coupled (Van Der Maarel, 2003), double-quantum filtration (DQF) detects the contribution from both of these tensors. Hence, using eq. [2.51], a signal after the DQF can be expressed as in eq. [3.2] (Navon et al., 2001):

$$
\begin{aligned}
S(\tau, t_{acq}, \omega_Q) = &-\frac{3}{2}\sin^2\theta \sin(\omega_Q \tau)\, e^{-\frac{\tau}{T_{2short}}} \sin(\omega_Q t_{acq}) e^{-\frac{t_{acq}}{T_{2short}}} \\
&+\frac{3}{8}\sin^2\theta\,(3\cos^2\theta - 1)^2 \\
&\cdot \left[e^{-\frac{\tau}{T_{2long}}} - \cos(\omega_Q \tau)\, e^{-\frac{\tau}{T_{2short}}}\right] \\
&\cdot \left[e^{-\frac{t_{acq}}{T_{2long}}} - \cos(\omega_Q t_{acq})\, e^{-\frac{t_{acq}}{T_{2short}}}\right],
\end{aligned}
\qquad [3.2]
$$

where θ is a flip angle of the pulses θ_2 and θ_3, and using eq. [2.39], ω_Q in the laboratory frame can be defined as in eq. [3.3]:

$$
\omega_Q = C_Q \frac{3\cos^2\theta - 1}{2}. \qquad [3.3]
$$

Free induction decay (FID) after triple quantum filtration (TQF) is given as in eq. [3.4]:

$$
\begin{aligned}
S(\tau, t_{acq}, \omega_Q) = \frac{9}{16}\sin^4\theta \cdot &\left[e^{-\frac{\tau}{T_{2long}}} - \cos(\omega_Q \tau)\, e^{-\frac{\tau}{T_{2short}}}\right] \\
&\cdot \left[e^{-\frac{t_{acq}}{T_{2long}}} - \cos(\omega_Q t_{acq})\, e^{-\frac{t_{acq}}{T_{2short}}}\right].
\end{aligned}
\qquad [3.4]
$$

Transfer functions $\frac{3}{2}\sin^2\theta$ and $\frac{3}{8}\sin^2\theta\,(3\cos^2\theta - 1)^2$ for the tensors $\hat{T}_{2,-1}$, $\hat{T}_{3,-1}$ correspondingly from the DQF experiment and $\frac{9}{16}\sin^4\theta$ for only $\hat{T}_{3,-1}$ from the TQF

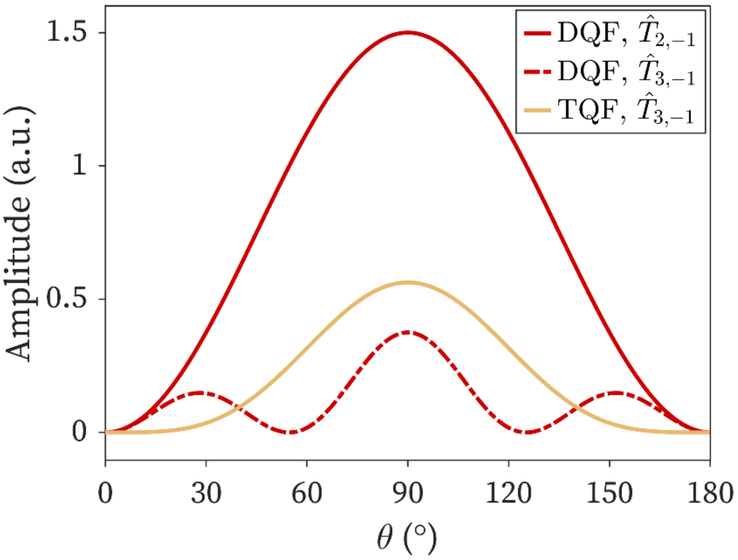

Figure 3.4. Transfer functions vs pulse flip angle θ for the tensors $\hat{T}_{2,-1}$, $\hat{T}_{3,-1}$ (DQF) and $\hat{T}_{3,-1}$ (TQF) in the MQF pulse sequence.

experiment are plotted in Figure 3.4. It can be seen that if the pulses are $\theta_2 = \theta_3 = 90°$, maximum contributions from both $\hat{T}_{2,-1}$ and $\hat{T}_{3,-1}$ can be detected in the DQF pulse sequence. If $\theta_2 = \theta_3 = 54.7°$ (magic-angle – MA), $\hat{T}_{3,-1}$ vanishes and only the contribution of $T_{2,\pm2}$ is detected, which arises exclusively from the anisotropic residual quadrupolar interaction (RQI) (Eliav et al., 1992; Eliav & Navon, 1994). The tensor $\hat{T}_{3,\pm3}$ arising due to the slow motion can be detected by the TQF sequence with its maximum amplitude at $\theta_2 = \theta_3 = 90°$ (Navon et al., 2001).

3.2 Hypothesis and Aims

Sodium in the skin especially in T2DM has mainly been studied by ^{23}Na magnetic resonance predominantly by imaging techniques. The aim of the thesis is to apply sodium MR single and multiple quantum spectroscopy in an ultra-high field of 9.4 T to study the relaxation behaviour of sodium, determine its short and long components of transverse relaxation time, T_{2short} and T_{2long}, and quadrupolar interaction ω_Q to assess the sodium molecular environment and the order of the skin tissue in patients with type 2 Diabetes compared to controls. It is hypothesized that the sodium molecular environment in the skin of T2DM patients is different from control patients and sodium relaxation times and ω_Q can be potential biomarkers of the disease.

3.3 Materials and Methods

Sections 3.3.1-3.3.3 introduce the components of the experimental setup in 9.4 T. Section 3.3.4 describes the MR sequences used in experiments and the parameters of the sequences for individual sets of measurements.

3.3.1 Spectrometer

Experiments were performed using an ultra-high field NMR spectrometer (Avance III, UltraShield 400WB Plus, Bruker, Rheinstetten, Germany) which contains a superconducting magnet generating a magnetic field of 9.4 T (resonance frequency 400 MHz for ^{1}H and 105.86 MHz for ^{23}Na) (Figure 3.5). The magnet is equipped with an active shimming system operating at room temperature, a temperature control unit, and a set of amplifiers. The latter contains a selective amplifier (proton amplifier) specifically designed to amplify the higher frequencies associated with ^{1}H, and a

Figure 3.5. Ultra-high field 9.4 T NMR spectrometer by Bruker. Temperature inside the bore can be controlled by the temperature control unit.

broadband amplifier (also named X-BB) used to amplify a wide range of frequencies besides ^{1}H. The X-BB amplifier was used to perform experiments on a resonance frequency of sodium (^{23}Na). The spectrometer is operated by the software TopSpin 3.2 (Bruker).

3.3.2 Probes

^{23}Na NMR experiments were conducted using a single-channel sodium microimaging probe with a 25 mm internal diameter and 40 mm length manufactured by Bruker (Figure 3.6). The probe contains a volume saddle coil, and it operates in both transmit and receive modes. The probe is attached to a probe base which is universal for all probes provided by Bruker in our laboratory. The probe base has regulators that extend to trimmer capacitors of the probe to make tuning and matching of the probe possible outside the magnet bore. The base also supports a dual-channel option.

Figure 3.6. ^{23}Na probe by Bruker with an internal diameter of 25 mm used for sodium experiments.

3.3.3 Skin samples

Human skin samples were provided by Arden Tissue Bank after skin reduction surgery from 15 patients. Exclusion criteria for age, weight, and sex were not imposed. The necessary ethics permits for this study were in place and obtained in collaboration with the Clinical Diabetes research group of the University of Warwick and UHCW NHS Trust. Patients were subdivided into two groups: control and diabetic. The main criterion for the diabetic group of patients was existing T2DM only. Group characteristics are summarized in Table 3.1.

13 human skin samples from 6 control patients and 10 samples from 6 diabetic patients were scanned. 4 samples from control patients and all samples from diabetic patients were obtained from the foot/leg. The remaining 9 samples from the control patients were taken from the abdomen (Table 3.1). Samples were vacuum-packed individually and delivered on ice within 4 hours after surgery. An example of the skin sample used for the experiments is shown in Figure 3.7.

All the samples were positioned inside the magnet in a way that the z-axis of the sample in Figure 3.7 was parallel to the z-axis of the magnet bore and the probe (the longest side of the skin sample was perpendicular to the xy-plane). All the samples were scanned at 37°C.

Table 3.1. Characteristics of the studied patients' group. A number of samples taken from each patient is indicated. Samples were obtained from two body parts: foot/leg and abdomen.

Control					**Diabetic**				
Patient ID	**Age**	**Gender**	**Samples**	**Location**	**Patient ID**	**Age**	**Gender**	**Samples**	**Location**
C1	27	female	1	abdomen	**D1**	61	Male	2	foot/leg
C2	62	female	2	abdomen	**D2**	71	Male	1	foot/leg
C3	53	female	2	abdomen	**D3**	73	Male	2	foot/leg
C4	46	female	2	abdomen	**D4**	56	Male	2	foot/leg
C5	33	female	4	foot/leg	**D5**	61	Male	2	foot/leg
C6	49	female	2	abdomen	**D6**	-	Female	1	foot/leg
		Total:	9	abdomen			**Total:**	10	foot/leg
			4	foot/leg					

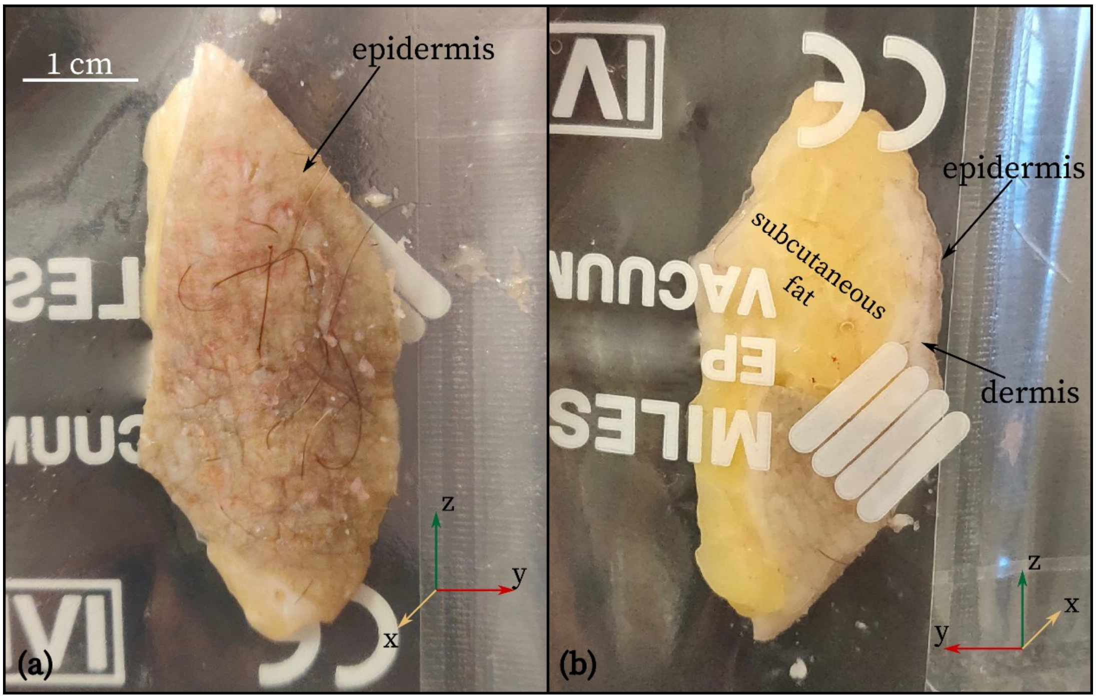

Figure 3.7. A photograph of a human skin sample obtained from the control patient taken from the foot. Epidermis, dermis and subcutaneous fat are pointed with arrows. (a) Top side, (b) bottom side. All the samples were positioned inside the magnet in a way that the z-axis of the sample was parallel to the z-axis of the magnet bore (skin perpendicular to the xy-plane). The white letters seen in the photo belong to the vacuum packaging.

3.3.4 Methods

This subsection describes pulse sequences used in the experiments conducted in 9.4 T. In these sequences, spatial encoding was not used, therefore, the signal was acquired from a whole sample inside the coil. Experiments with the skin samples were performed in domestic collaboration.

3.3.4.1 Flip angle calibration

The flip angle was calibrated for each skin sample, firstly together with the phantoms (if scanned with the phantoms), and secondly when the phantoms were removed. A flip angle of the pulse depends on the amplitude of the B_1 field of a probe and a pulse duration τ_p as in eq. [3.5] (Haacke et al., 1999):

$$\theta = \gamma B_1 \tau_p. \qquad [3.5]$$

RF power was left constant at 200 W (the same magnitude of B_1), and τ_p was changed in the "pulse-acquire" sequence to find the duration of a 180° pulse. This was determined where the first registered point of the FID becomes zero. Then this pulse duration was divided by 2 to obtain a duration of 90° pulse. For different skin samples, the length of the 90° pulse varied in a range of 40-69 μs.

3.3.4.2 Spectroscopy

3.3.4.2.1 CPMG pulse sequence

The Carr-Purcell-Meiboom-Gill sequence, or CPMG, is shown to significantly reduce the effect of diffusion while measuring T_2. This method follows an equation $90° - \tau - \{180° - 2\tau\}_n$ (Carr & Purcell, 1954; Meiboom & Gill, 1958) where 2τ is the echo time (TE). However, on the spectrometer used in this thesis, the sequence was implemented as follows: to acquire n-th echo, an excitation 90° RF pulse and a train of n 180° RF pulses are applied (Figure 3.8). The time between 90° and 180° pulses is half of the echo time. Each 180° pulse refocuses spins in a transverse plane that leads to the formation of an echo at the TE (or TE/2 after the 180° pulse) but acquisition happens only after the last 180° pulse. With increasing the number of 180° pulses, heating effects may appear causing phase and frequency shifts of the spectra. However, it was established that these shifts are smaller than one-third of the line width, thus they can be neglected. CPMG was conducted with TE = 2 ms, 32 echoes, and 32 scans; receiver gain (RG) was set to 32, 101 or 1030 depending on the sodium signal intensity of the samples. All measurements were performed at 37°C, close to body temperature.

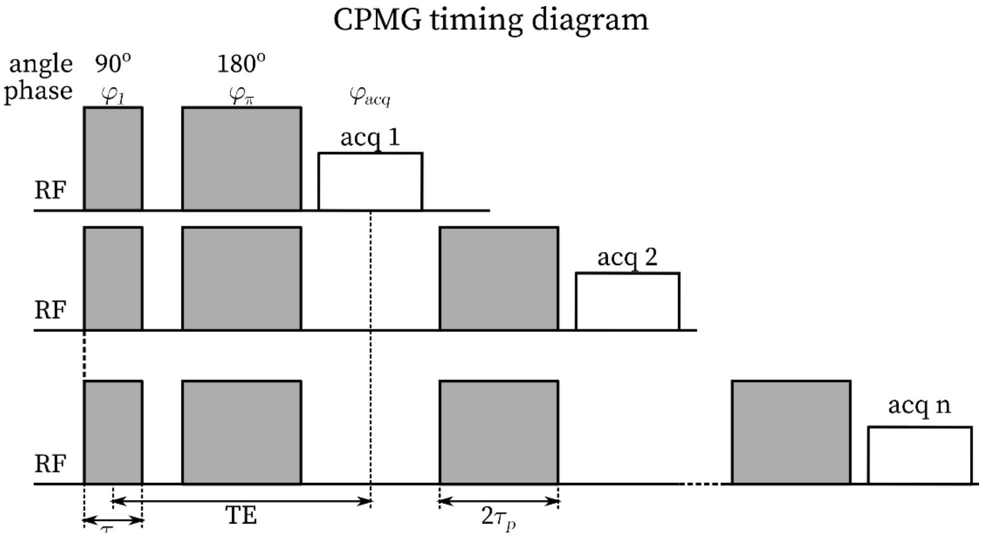

Figure 3.8. CPMG pulse sequence timing diagram performed on Bruker spectrometer.

3.3.4.2.2 Double-Quantum Filtering with Magic Angle

Double-quantum filtering (DQF) can detect contributions from coherences described by the tensors $\hat{T}_{2,\pm2}$, $\hat{T}_{3,\pm2}$ which arise due to residual quadrupolar interaction and slow-motion regime in anisotropic media correspondingly. The timing equation of the DQ filter pulse sequence is $\theta_1(\varphi_1) - \tau/2 - (\pi) - \tau/2 - \theta_2(\varphi_2) - \delta - \theta_3(\varphi_3)$, where flip angles are $\theta_1 = \theta_2 = \theta_3 = 90°$, τ is the creation (or preparation) time, and δ is the evolution time. A 180° pulse (π-pulse) may be applied between θ_1 and θ_2 pulses to refocus B_0 inhomogeneities. If the last two pulses of the sequence are set to $\theta_2 = \theta_3 = 54.74°$ (magic angle), the contribution from the slow-motion regime is suppressed ($\hat{T}_{3,\pm2}$), leaving the coherences only from the anisotropic environment to detect (Figure 3.9). Therefore, the DQ filter with magic angle, DQF-MA, is a unique and selective tool to study these environments.

A 30-step phase cycle was applied for DQF-MA: all possible combinations of phases φ_1, φ_2, and φ_π, where they can take values of 0°, 90°, 180° and 270°, and $\varphi_3 = 0°$, $\varphi_{acq} = 0°, 180°$.

DQF-MA experiments were conducted with the same lengths of 90° and 180° pulses as in the CPMG experiment. The length of the 54.74° pulse was calculated accordingly. A time between 90° and 180° pulses t_{p-p} (and also between 180° and the first 54.74° pulse) was varied from 100 μs to 500 ms in 23 steps logarithmically. Therefore, 23 FIDs were obtained from each sample in 1440 scans. From the timing

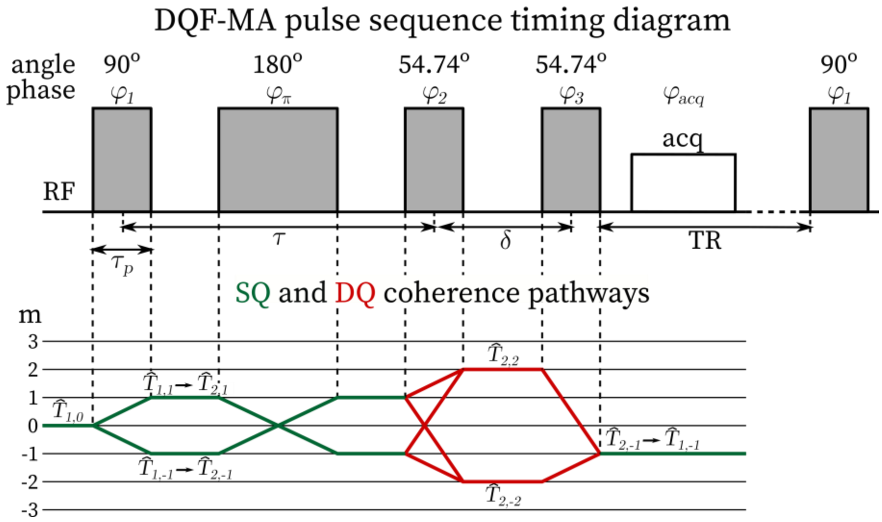

Figure 3.9. DQF-MA sequence timing diagram with coherence pathways ($\theta_1 = 90°$, $\theta_2 = \theta_3 = 54.74°$).

diagram in Figure 3.9, t_{p-p} is related to the preparation time τ and 90°, 180° and 54.74° pulse lengths by the equation: $t_{p-p} = (\tau - \tau_{90^\circ}/2 - \tau_{180^\circ} - \tau_{54.74^\circ}/2)/2$. Repetition time (TR) was 200 ms.

The first aim of the experiment was to investigate the interactions of the sodium nuclei with the macromolecules such as collagens, GAGs and PGs, in the skin tissue by measuring the short component of the relaxation time T_{2short} and residual quadrupolar interaction ω_Q. The second aim was to examine if the values of T_{2short} obtained from the fitting of DQF-MA build-up curves were in agreement with the CPMG experiments.

3.3.4.2.3 Triple-quantum filtering

Triple quantum filtered (TQF) spectroscopy is used to detect the coherence $\hat{T}_{3,\pm3}$ derived due to the slow-motion regime. A timing diagram of the TQF pulse sequence is similar to DQF (Figure 3.10) where $\theta_1 = \theta_2 = \theta_3 = 90°$ but a 48-step phase cycle was applied where the phases φ_1 is running through the values 30°, 90°, 150°, 210°, 270°, 330°; φ_2 holds values of 0°, 60°, 120°, 180°, 240° and 300°, but φ_π takes values of both φ_1 and φ_2; $\varphi_3 = 0°$; φ_{acq} alternates between 0° and 180°. TQF spectroscopy was performed to resolve the long component of sodium relaxation, T_{2long}, as T_{2short} and ω_Q can be derived from DQF-MA.

TQF spectroscopy was performed with the following parameters: lengths of all 90° pulses and the 180° pulse were the same as in the CPMG experiment, with varying time between pulses t_{p-p} from 100 µs to 500 ms (as in DQF-MA); TR = 200 ms.

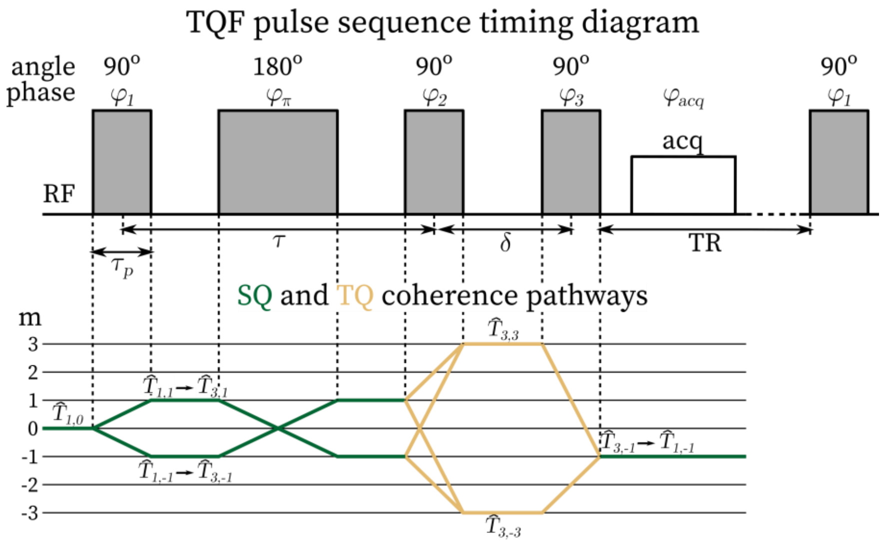

Figure 3.10. TQF sequence timing diagram with coherence pathways.

Another aim to conduct a TQF spectroscopy experiment is to determine a preparation time τ_{opt} which gives a maximum signal for the TQ coherence. Later, this τ_{opt} was used to perform TQF imaging (Hanson et al., 2021).

3.3.4.3 Data processing

3.3.4.3.1 CPMG

During the Fourier Transform (FT) of sodium CPMG echoes, line broadening of 20 Hz was applied for each CPMG echo train and then the echoes' spectra were integrated over the frequency domain. The integration range was constant for each experiment (20 ppm) for each sample and was broader than the peak width at its base. Integration was preferred to the peak intensity due to the changing contributions of short and long relaxation components with the echo time (Brown & Wimperis, 1994). As the samples were scanned with different RG, integral values obtained in the previous step were divided by RG value.

Three diabetic samples (sample 2 of patient D4, sample 1 of patients D5 and D6) had asymmetric CPMG spectra with an extra small peak present on the right side of the main sodium peak (Figure 3.12). To separate this additional component, spectral deconvolution was performed in Igor.Pro before the integration. Two peaks were fitted with Gaussian line shapes. The line shapes were chosen Gaussian but not Lorentzian to compensate for distribution of chemical shifts arising due to significant lengths (3-4 cm) and widths (2-3 cm) of the skin samples, as an excitation was performed without slice selection. "Pulse-acquire" experiments of these samples were used as a reference to determine the widths of the Gaussians which were then used to fit CPMG echoes and were kept constant for every value of TE.

The additional peak on the right was determined to be wider and smaller in height than the main sodium peak. Then, the integral of the main sodium peak was calculated, plotted vs TE and fitted to determine the original sodium relaxation times which are not contaminated with signal excitations outside the RF probe.

To perform fitting of the CPMG echo train for each sample, the following model was used. For slow-moving sodium interacting with macromolecules in the skin, relaxation is biexponential with short and long T_2 times (T_{2short} and T_{2long}) with 60 and 40% contributions respectively (eq. [3.6]):

$$I_{bi}(t) = I_o\left(0.6 \cdot exp\left(-\frac{t}{T_{2short}}\right) + 0.4 \cdot exp\left(-\frac{t}{T_{2long}}\right)\right). \qquad [3.6]$$

The skin samples contained a physiological liquid – extracellular fluid (ECF). Considering a slow exchange between slow sodium in the skin with ECF sodium, there is a separate term for ECF sodium that relaxes monoexponentially with its own time constant T_2: $I_1 exp\left(-\frac{t}{T_2}\right)$. Bearing in mind that the fraction of ECF sodium is much smaller than the fraction of bound sodium in the skin biopsies: $I_1 \ll I_0$, and the relaxation time of ECF sodium T_2 is much longer than T_{2long} of the bound sodium, an approximation was made (eq. [3.7]):

$$I_1 exp\left(-\frac{t}{T_2}\right) \approx constant. \qquad [3.7]$$

Therefore, a final fitting model is described by the following equation [3.8]:

$$I_{bi}(t) = I_o\left(0.6 \cdot exp\left(-\frac{t}{T_{2short}}\right) + 0.4 \cdot exp\left(-\frac{t}{T_{2long}}\right)\right) + offset. \qquad [3.8]$$

The parameters I_0, $offset$, T_{2short} and T_{2long} were obtained by fitting the experimental data to eq. [3.8] using the Levenberg-Marquardt algorithm in the software Igor.Pro 8 (WaveMetrics®, USA). Constraints were applied for T_{2short} to be less than 5 ms according to the literature (Madelin, Lee, et al., 2014). The heating effects mentioned previously did not affect fitting results.

3.3.4.3.2 DQF-MA spectroscopy

Firstly, the line broadening (LB) was applied to each of the 23 FIDs from the DQF-MA spectroscopy experiments with the factor $LB = 150$ Hz for every sample to improve SNR. Also before FT, the data was zero-filled once up to 1024 complex points. After FT, the complex pseudo-2D spectrum was processed using a homemade routine in MATLAB. In particular, 23 spectra for each skin sample were summed up to make a projection. Then this projection was phased in a way that its real part has a shape of an antiphase pair of two spectral lines in an absorption mode (Navon et al., 2001). Then the obtained phase was applied to all individual 23 spectra. Next, the amplitude of the signal was determined as a sum of absolute values of positive and negative peaks' heights for every value of τ.

The time evolution of the DQF-MA signal is affected only by a short component of the T_2 relaxation, T_{2short}, and the residual quadrupolar interaction ω_Q as in eq. [3.9]:

$$S_{DQF-MA}(\tau, t_2, \omega_Q) = -A\sin(\omega_Q\tau)\, e^{-\frac{\tau}{T_{2short}}} \sin(\omega_Q t_2)\, e^{-\frac{t_2}{T_{2short}}}. \qquad [3.9]$$

T_{2short} and ω_Q can be determined from a fitting of a build-up curve (eq. [3.10]):

$$S_{DQF-MA}(\tau, \omega_Q) = A\sin(\omega_Q\tau)\, e^{-\frac{\tau}{T_{2short}}} \qquad [3.10]$$

of the spectra intensities vs τ.

3.3.4.3.3 TQF spectroscopy

FID obtained after TQ filtration can be described by the equation [3.11]:

$$\begin{aligned} S_{TQF}(\tau, t_2, \omega_Q) = A\left[e^{-\frac{\tau}{T_{2long}}} - \cos(\omega_Q\tau)\, e^{-\frac{\tau}{T_{2short}}}\right] \times \\ \times \left[e^{-\frac{t_2}{T_{2long}}} - \cos(\omega_Q t_2)\, e^{-\frac{t_2}{T_{2short}}}\right]. \end{aligned} \qquad [3.11]$$

Using T_{2short} and ω_Q obtained from the fitting of the DQF-MA build-up curve for each skin sample, a TQF build-up curve $S_{TQF}(\tau, \omega_Q)$ can be fitted vs τ with only two free parameters, amplitude A and T_{2long} (eq. [3.12]):

$$S_{TQF}(\tau, \omega_Q) = A\left[e^{-\frac{\tau}{T_{2long}}} - \cos(\omega_Q\tau)\, e^{-\frac{\tau}{T_{2short}}}\right]. \qquad [3.12]$$

3.3.4.4 Statistical analysis

Data are presented as means with standard deviations (SD). Statistical analysis was performed using Igor.Pro and consisted of several steps: firstly, the data were tested for normality and random selection. To test if the data is randomly distributed in its sequence, a serial randomness (SR) test was used. Two tests were applied to determine the normality of the data: the Kolmogorov-Smirnov (KS) test and the Jarque-Bera (JB) test. In Igor.Pro a default JB test works for a number of data points in the range of [7; 2000]. As the control group of foot samples had only 4 samples, the test was performed manually. Skewness, kurtosis, and JB statistics were calculated using Excel (Microsoft, Redmond, Washington, USA). JB cumulative distribution function (CDF) for $n = 4$ was simulated using the Monte-Carlo method in Igor.Pro. Then JB statistics was compared with the critical value of JB CDF at the 0.95 level.

If data in the group is a normally distributed random selection, the next step is to compare variances of the groups using ANOVA. If the hypothesis of equal variances cannot be rejected, the statistical significance of differences between groups should be established using an unpaired two-tailed t-test. If the normality of the data can't be established properly, for example, due to a small sample size, or the data does not follow a normal distribution, the Wilcoxon Rank Test is performed.

Bar charts to show data distribution within the groups were built in Prizm (GraphPad Software©, USA). The results of the statistical analysis, p-values, are indicated on the graphs.

3.4 Results

This section describes the results of the single quantum and multiple quantum spectroscopy experiments performed in 9.4 T with the samples of human skin *ex vivo*.

3.4.1 Single quantum spectroscopy

This subsection includes the results of CPMG spectroscopy (Subsection 3.4.1.1) of the skin samples. The pulse sequence and its parameters were described in Subsection 3.3.4.2.1. Data processing procedures were given in Subsections 3.3.4.3-3.3.4.4.

3.4.1.1 CPMG

A typical ^{23}Na NMR pseudo-2D spectrum of human skin obtained by using the CPMG pulse sequence is presented in Figure 3.11. This spectrum contains Fourier transforms of all the echoes obtained at a different echo time TE. As described in Subsection 3.3.4.3.1, these spectra were integrated, and integral values were plotted vs TE and fitted with the equation [3.8].

The shape of the spectra shown in Figure 3.11 is symmetrical. However, sample 2 of patient D4, the sample 1 of patients D5 and D6 possess asymmetrical spectra with a tail or an additional small peak on the right side of the main peak. Examples of these spectra are shown in Figure 3.12(a) and the asymmetries are indicated by arrows. The frequency axes of the spectra are zoomed in 4 times on both spectra to show the features more explicitly. These spectral attributes might indicate off-resonance excitation of some physiological fluid outside the RF coil.

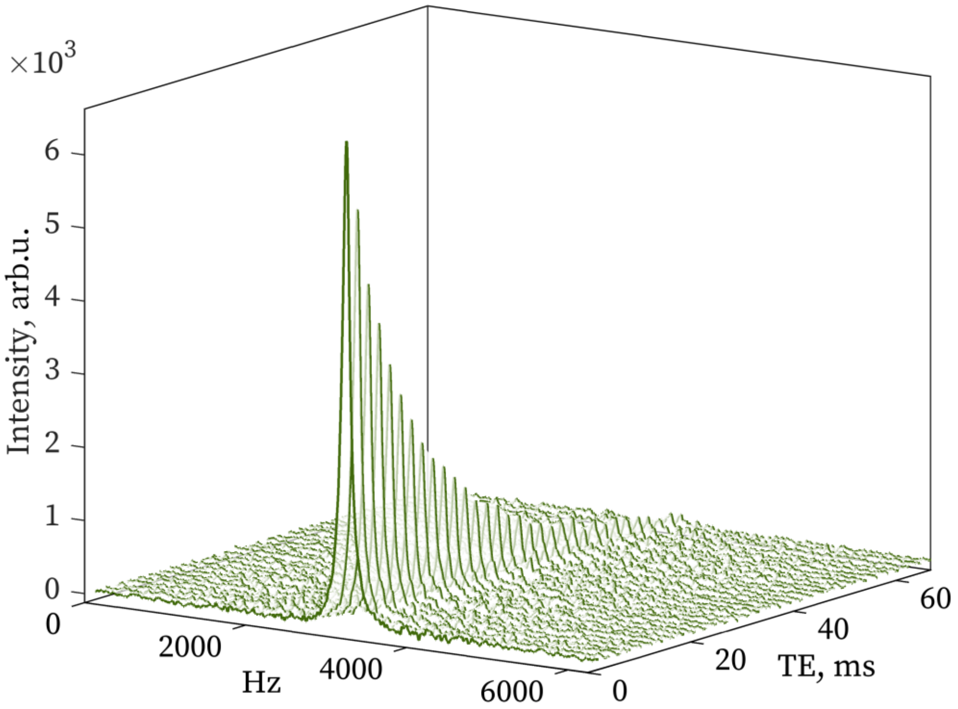

Figure 3.11. ^{23}Na NMR Fourier transformed CPMG echoes obtained from the human skin sample from an abdomen of a control patient as a function of the TE.

For the samples with asymmetric spectra, spectral deconvolution was performed (Subsection 3.3.4.3.1). Figure 3.12(b) shows how echo 5 of the D5 patient's sample 1 is decomposed into two Gaussians: peak 1 corresponds to the primary sodium peak, while peak 2 represents the signal excited outside the RF probe. Time evolution of peak 1 only was considered.

Plots of the echo integrals as functions of TE for foot/leg samples, one from the control and one from the diabetic patients are shown in Figure 3.13(a). Values of the fitting coefficients, T_{2short} and T_{2long}, for a range of samples from control and diabetic patients are presented in Table B.1. Bar charts showing the mean values ± standard deviation (SD) are given in Figure 3.14.

Figure 3.13((b) and (c)) shows a semilogarithmic dependence of echo integrals on the echo time of the same pair of skin samples as in Figure 3.13(a). The experimental data points on these graphs are fitted with a logarithm of a monoexponential decay described by eq. [3.13]:

$$\ln\big(I(t)\big) = -\frac{t}{T_2} + \ln(I_0). \qquad [3.13]$$

It can be seen from Figure 3.13 ((b)-(c)) that the relaxation curve of the sodium signal in the skin is not monoexponential, it is biexponential: several first points deviate from a straight fitting line revealing two distinct relaxation time components. Therefore, the fitting model described by eq. [3.8] is validated. Additionally, both biexponential and linear fits can be compared by R^2-statistics: R^2 = 0.9927 for the control and R^2 =

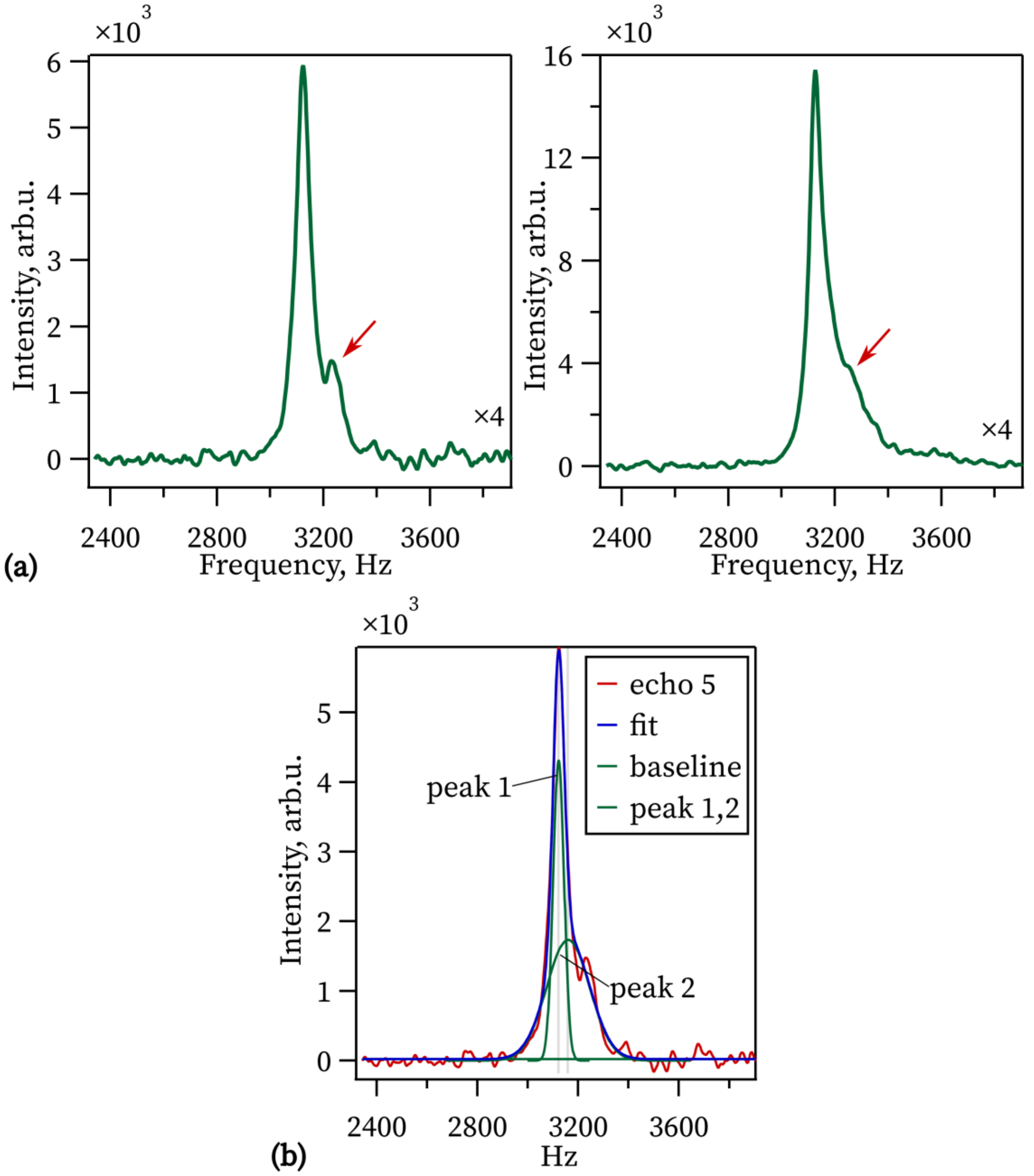

Figure 3.12. (a) Examples of fifth echoes in CPMG train for two diabetic foot/leg samples (sample 1 of the patients D5 and D6). The x-axis was zoomed in 4 times for a better representation of the spectral features: additional peaks on both graphs are indicated by red arrows. (b) Spectral deconvolution of the 5th echo of sample 1 of the patient D5 with two Gaussians: peak 1 represents the main sodium peak, peak 2 corresponds to the signal excited outside the rf probe. Two light grey lines show the positions of maximums of peaks 1 and 2.

0.9973 for the diabetic patient of the biexponential fit (Figure 3.13(a)) is higher than $R^2 = 0.9558$ and $R^2 = 0.9853$ for the control and diabetic patients correspondingly of the linear fit.

According to the performed statistical analysis (described in Subsection 3.3.4.4), all the data within the groups (control abdomen, control foot/leg and diabetic foot/leg) is

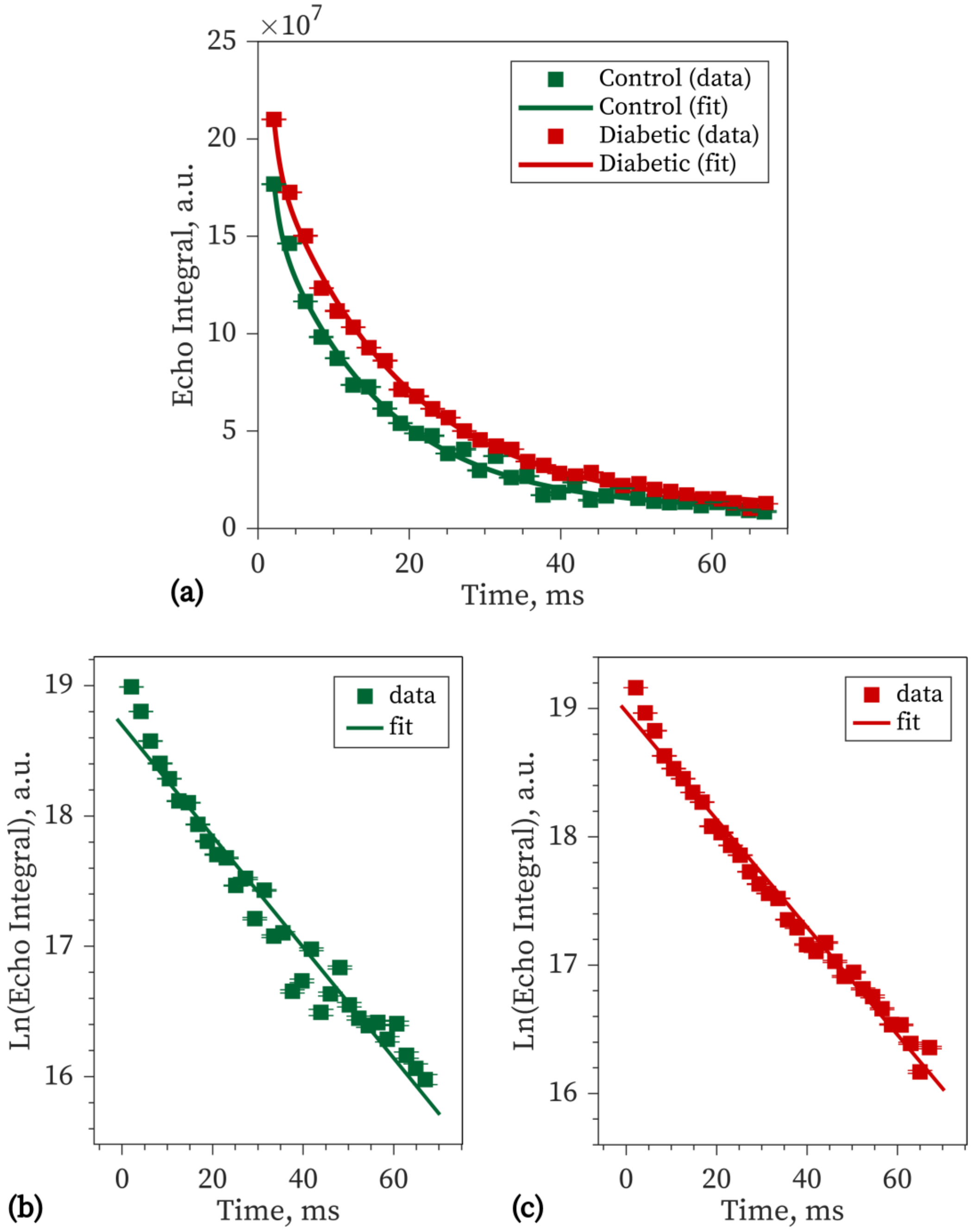

Figure 3.13. Sodium CPMG echo integrals of the foot/leg skin samples from control (green) and diabetic (red) patients as a function of echo time (TE) in (a) original ($R^2 = 0.9927$ and 0.9973 correspondingly) and (b)-(c) semilogarithmic scale ($R^2 = 0.9558$ and 0.9853 correspondingly). Squares represent experimental data; solid lines correspond to the calculated fitting function [3.4].

a normally distributed random selection. Based on the results of ANOVA, equal variances were assumed between groups of foot/leg and abdomen samples from control patients and between groups of samples from control (abdomen and foot/leg samples together) and diabetic patients for both T_{2short} and T_{2long}. Therefore, an unpaired two-tailed t-test was performed to estimate the significance of the difference between the groups. The results of the t-test, p-values, are shown in Figure 3.14.

For samples from the control patients, no significant difference was found between two skin locations, foot/leg and abdomen, for both T_{2short} and T_{2long} (Figure 3.14(a)). Therefore, abdomen and foot/leg samples from control patients were combined in one control group and compared with foot/leg samples from diabetic patients.

In the patients with T2DM, the 33% lengthening of T_{2long} was observed compared to controls (Figure 3.14(b)) which was significant ($p < 0.0001$). T_{2short} was found to be indifferent to the presence of Diabetes Mellitus.

In the CPMG experiments described above, the sodium signal is the sum of signals obtained from the different parts of the skin samples. The composition of the skin samples *ex vivo* was studied using high-resolution proton imaging to identify tissue elements and then sodium gradient echo (GE) imaging was performed to determine sodium localization (Hanson et al., 2021). Main skin layers like the epidermis, dermis,

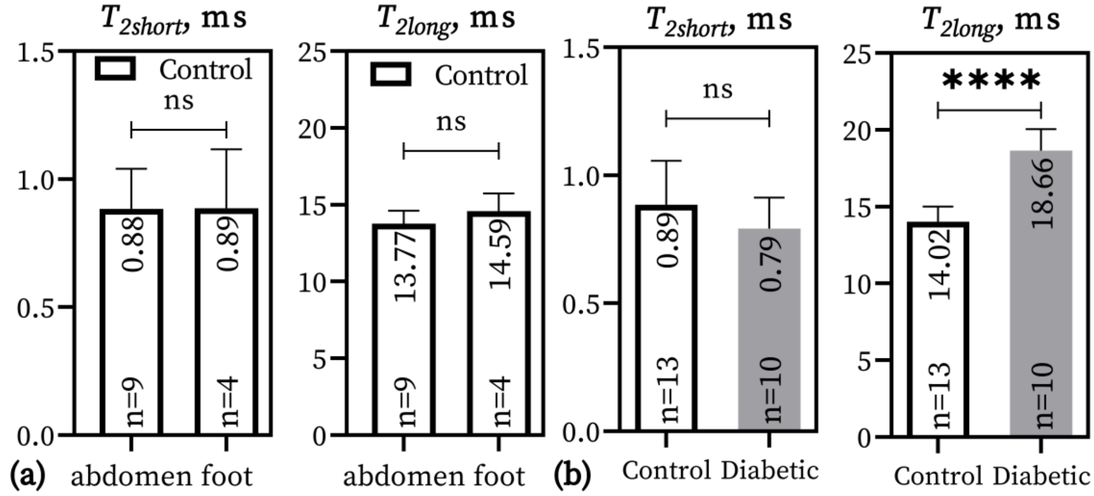

Figure 3.14. Mean ± SD of sodium T_{2short} and T_{2long} obtained from biexponential fitting of CPMG (a) for samples collected from the foot/leg and abdomen from control patients and (b) for all samples from control and diabetic patients (samples from foot/leg and abdomen from control patients are presented together in one control group). ****$p < 0.0001$, ns – nonsignificant.

hypodermis and also micro blood vessels could be identified on the axial proton images with specially developed contrast (Figure 3.15). When the proton image was overlayed with a nonselective axial sodium GE image, it can be seen that the dermis area has the highest signal intensity (Figure 3.16). Therefore, it is assumed that most of the sodium signal in the spectroscopic measurements is coming from the dermis. Some of the sodium signal that appears in the area of subcutaneous fat might originate from the physiological fluid of the tissue.

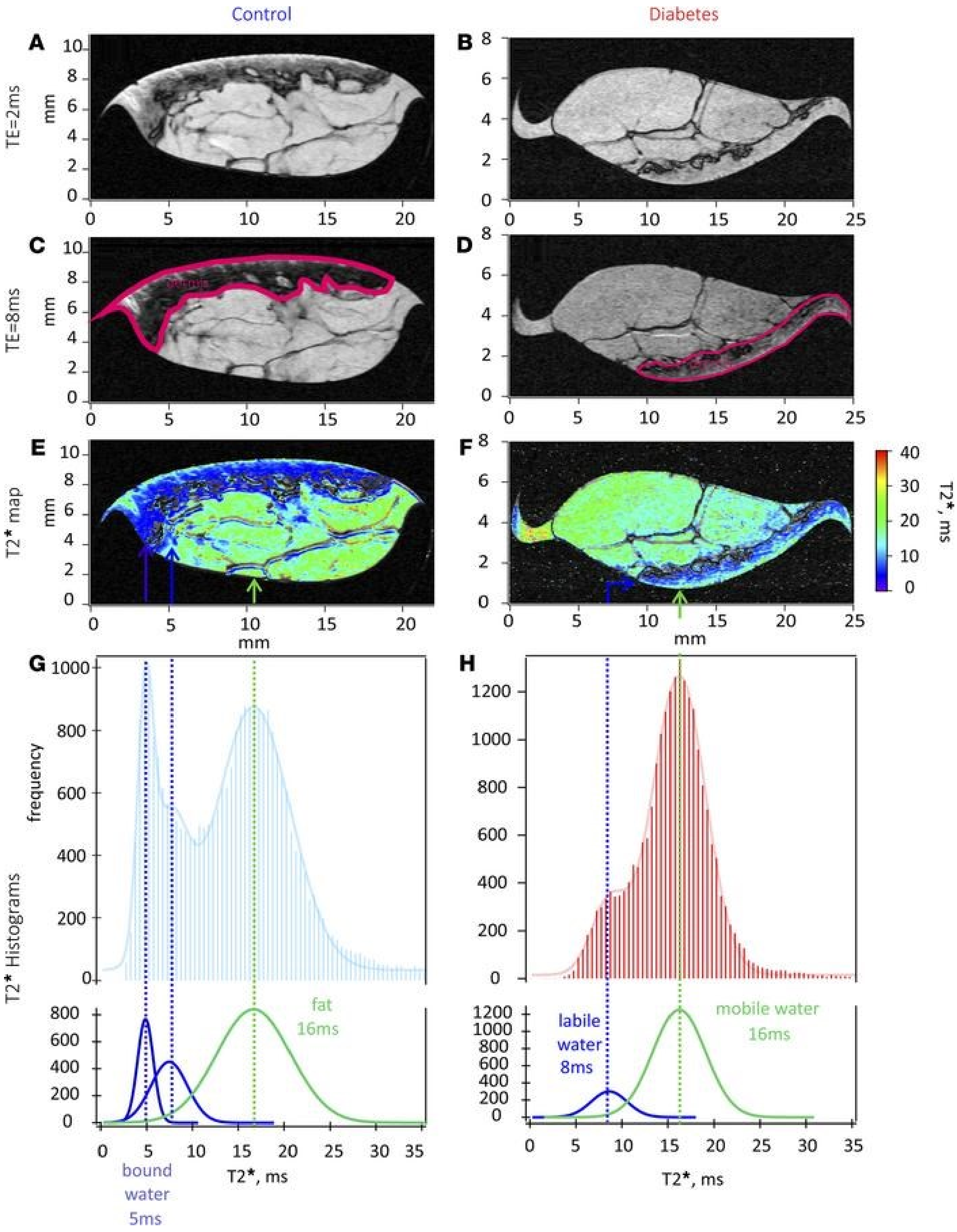

Figure 3.15. (A)-(B): Anatomical ^{1}H images of the human skin acquired at 9.4 T with TE = 2 ms from control (A) and diabetic (B) patients. (C)-(D): The increase of TE to 8 ms shows better contrast of skin layers (dermis is darker) in the same skin samples. (E)-(F): T_2^* maps for control (E) and diabetic (F) skin samples overlaid with anatomical images to emphasize short T_2^* values in the dermis layer and long T_2^* values in the adipose tissue. (G)-(H): Distributions of proton T_2^* values corresponding to each skin layer are shown for control (G) and diabetic (H) skin samples. The control sample has an additional peak of immobile water at $\overline{T_2^*}$ = 5 ms. Reproduced from (Hanson et al., 2021).

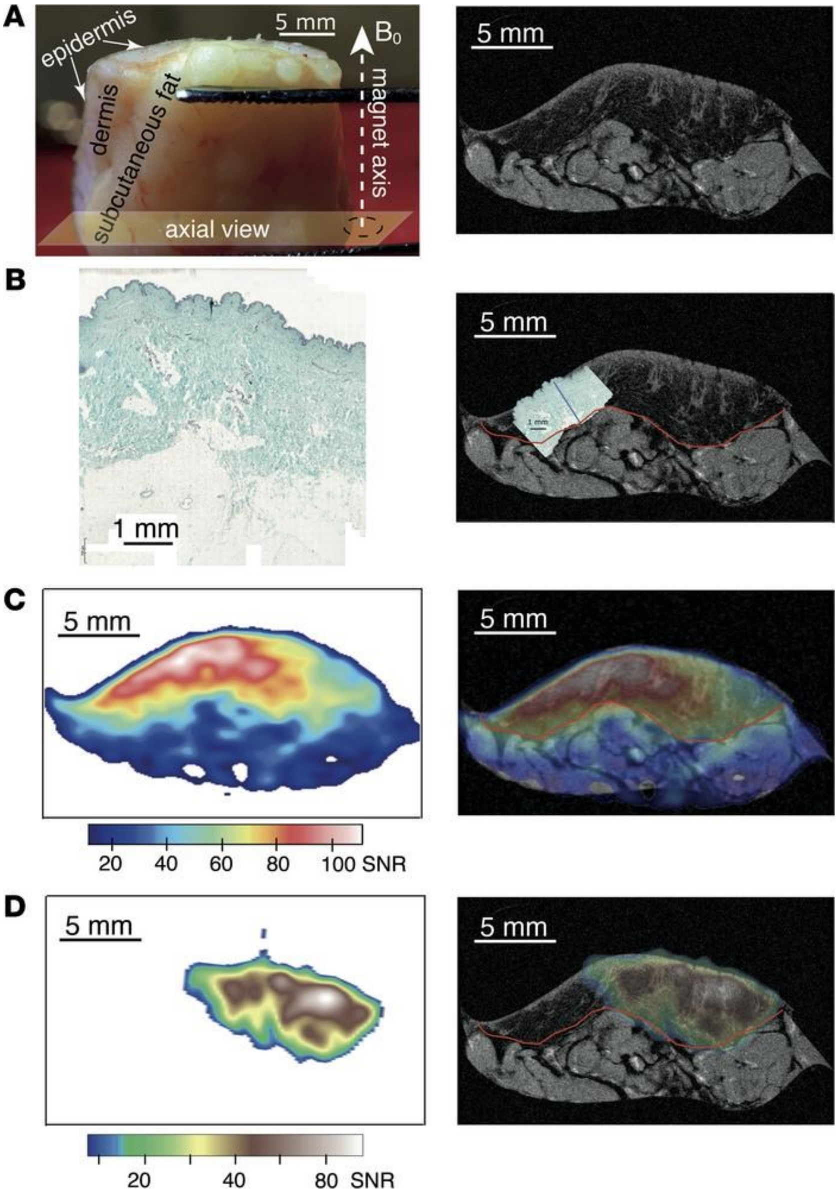

Figure 3.16. (A) A photograph of a typical skin sample indicating different skin structures and an MRI axial view (left) and a high-resolution axial ^{1}H MRI slice ($11 \times 11 \times 100\ \mu m^3$) revealing the anatomy of the diabetic skin sample (right). (B) A slice of histological GAG staining of a typical skin specimen (i.e., diabetic) (left) which is scaled and overlaid onto the ^{1}H MRI slice of the diabetic sample to demonstrate a prevailing localization of GAGs in the dermis layer (right). The depth of histological GAG staining is indicated by the blue line, while the red line highlights a boundary of the dermis layer. (C) A non-selective ^{23}Na MR image (left) and its overlay with an anatomical ^{1}H MRI slice (right) show the localization of free sodium in the diabetic skin sample. (D) A non-selective TQF ^{23}Na MR image (left) overlayed with an anatomical ^{1}H MR image (right) localises bound sodium in the diabetic skin sample. Note that both free and bound sodium colocalize predominantly with the dermis layer where GAGs are situated. Reproduced from (Hanson et al., 2021).

3.4.2 Multiple Quantum Spectroscopy

This section describes Double Quantum Filtered with Magic Angle (DQF-MA) and Triple Quantum Filtered (TQF) spectroscopy experiments in the skin samples *ex vivo*. The sequences and their parameters were given in Subsections 3.3.4.2.2 and 3.3.4.2.3 correspondingly. Data processing procedures were described in Subsections 3.3.4.3.2-3.3.4.3.3 and 3.3.4.4.

3.4.2.1 DQF spectroscopy with Magic Angle

In this Subsection, the results of the ^{23}Na DQF-MA measurements in the skin samples are presented. Statistical differences between different categories of samples (abdomen vs foot/leg in the control group, the control vs diabetic group) were investigated. Also, a comparison of DQF-MA T_{2short} values with CPMG T_{2short} values was made.

A representative DQF-MA spectrum of a skin sample obtained from a lower limb of a control patient at $\tau = 0.4$ ms is shown in Figure 3.17(a). As was mentioned in Subsection 3.3.4.3.2, its real part was phased as two antiphase spectral lines in an absorption mode and the amplitude of the signal was determined as a sum of absolute values of positive and negative peaks' heights for every value of τ. A dependence of the sodium signal amplitude on the preparation time τ is shown in Figure 3.17(b). The red curve is a fit to equation [3.10]. The relaxation time T_{2short} and the residual quadrupolar interaction ω_Q can be obtained from the fit. Figure 3.18 presents a dependence of ω_Q on τ for the same sample as in Figure 3.17. Data points are connected by straight lines to guide the eye. For each τ, values of ω_Q were determined as difference in frequency between positive and negative peaks (Kemp-Harper et al., 1994). It can be seen from Figure 3.18 that the distribution of ω_Q is present in the skin and its components are evolving at different speeds. Similar behaviour was observed for all the skin samples. Also, for a long τ SNR decreases dramatically, and precise determination of peak positions becomes difficult. Therefore, for these spectra with τ > 3.5 ms, it was impossible to determine ω_Q. Thus, the single value of ω_Q obtained from the fitting of the build-up curve is a weighted average of all ω_Q present in a skin sample. As $LB = 150$ Hz was applied, and the value of ω_Q defines the size of the splitting of the satellite transitions (Eliav & Navon, 1994), an actual value of ω_Q is masked by the line broadening of the spectra. Therefore, LB should be subtracted from the ω_Q values found from the fitting to receive an “actual” value of the residual quadrupolar coupling ω'_Q.

The values of T_{2short} and ω'_Q with their errors and for every sample in the control and diabetic groups are summarized in Table C.1. The mean values of T_{2short} and ω'_Q with their standard deviations are calculated in Table 3.2 and also presented as bar charts in Figure 3.19. T_{2short} and ω'_Q values were in the range of 0.48-1.23 ms and 0-578.1 Hz correspondingly. For the DQF-MA fitting, two skin samples from patients D2 and D6 of the diabetic group were discarded: the former due to bad SNR which did not allow a fitting procedure to be performed correctly, and the latter was removed because the phantoms were not extracted from the coil before performing the MQF experiments. Therefore, only 8 diabetic samples were considered in the statistical analysis.

Values of T_{2short} for control abdomen, control foot/leg and diabetic foot/leg samples were identified as normally distributed random samples by SR, KS, and JB tests. The hypothesis of equal variances was not rejected by ANOVA for every pair of compared

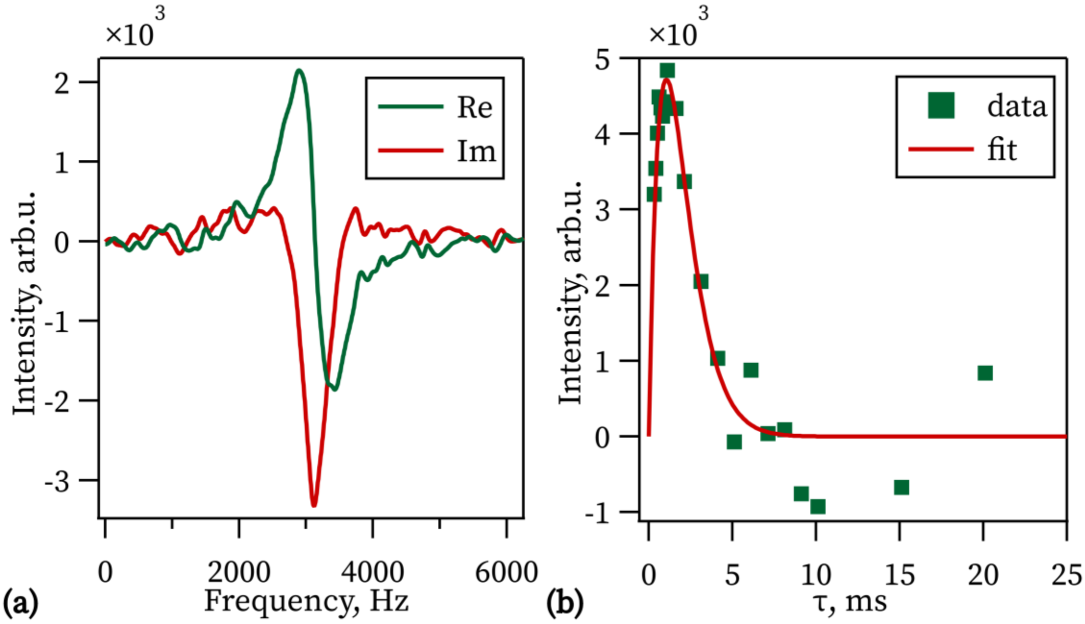

Figure 3.17. (a) DQF-MA spectrum of ^{23}Na in a human skin sample obtained from a foot/leg of a control patient at $\tau = 0.4$ ms. (b) ^{23}Na signal amplitude measured by DQF-MA pulse sequence as a function of the preparation time τ – a build-up curve, for the same skin sample. The data was fitted to equation [3.10]. The τ axis was limited to 25 ms out of 100 ms for a better representation of the rise and fall of the curve.

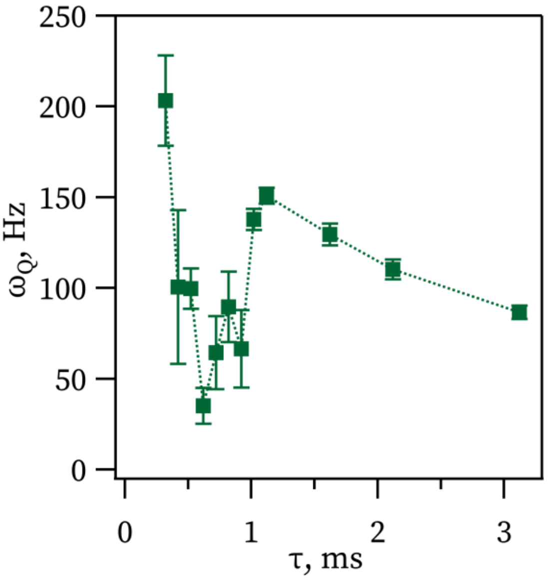

Figure 3.18. ω_Q vs τ for the same sample as in Figure 3.17. Data points are connected by straight dotted lines to guide the eye.

groups. Therefore, a two-tailed t-test was performed to assess the significance of the differences between the groups in pairs. The results of the t-tests are indicated in Figure 3.19(a). An average T_{2short} of the foot/leg samples was more than 30% higher than the average T_{2short} of the abdominal samples within the control group ($p < 0.05$). Although the values of T_{2short} for the foot/leg samples from the control and diabetic groups are not significantly different from each other, there is a trend of decreasing T_{2short} for the case of T2DM. In addition, the control abdomen samples were found not significantly different from the diabetic foot/leg samples.

T_{2short} fitting results of the DQF-MA were compared with T_{2short} values additionally determined by CPMG (Subsection 3.4.1.1). The DQF-MA values of T_{2short} alongside the CPMG values of T_{2short} are shown in Table 3.2. T_{2short} values obtained with the two methods were in agreement within the margins of errors.

Values of ω'_Q for control abdomen, control foot/leg and diabetic foot/leg samples were identified as normally distributed random samples by the SR and KS tests. However, the JB test rejected the hypothesis of a normal distribution for the control abdomen and the foot/leg samples as separate groups and when they were combined in one control group. As the ω'_Qs' normality for these samples was determined by the KS test, also T_{2short}s were normally distributed, and the values of ω'_Q for the diabetic samples

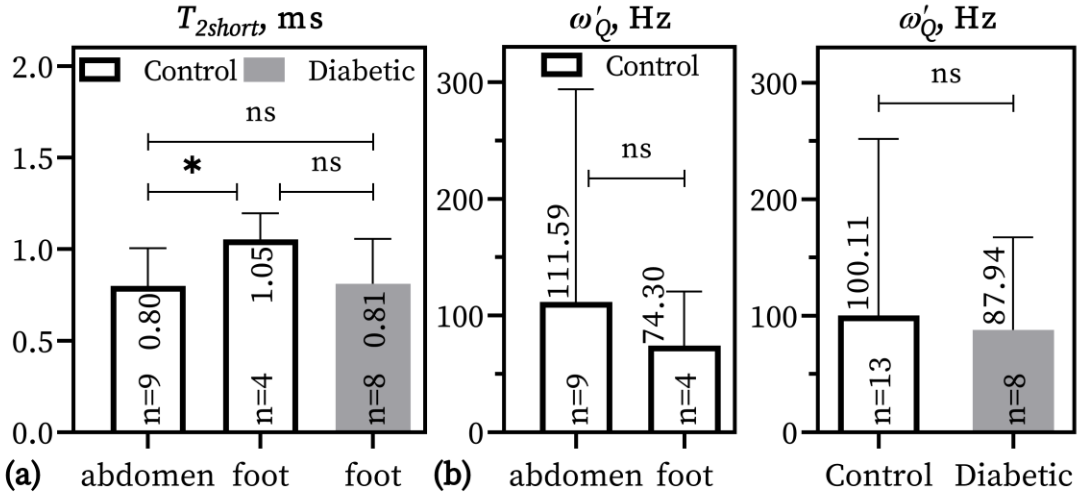

Figure 3.19. Summary of sodium mean T_{2short} (a) and ω'_Q (b) values with their SD obtained from fitting of sodium DQF-MA build-up curves with eq. [3.10] for the control and diabetic patients, abdomen and foot/leg samples. *p<0.05, ns – non-significant.

followed the normal distribution, it was assumed that ω'_Qs of the control samples are also normally distributed.

When comparing the abdomen and foot/leg samples from the control patients, ANOVA determined inequality of variances and the Wilcoxon Rank test was performed. Nevertheless, when these samples were united into one control group, the result of the ANOVA test supported the hypothesis of equal variances with the diabetic group. Therefore, a two-tailed t-test was performed to estimate the significance of the differences between these groups. The results of the Wilcoxon Rank test and the t-test are indicated in Figure 3.19(b). No significant difference was found between the abdomen and foot/leg samples in the control group; hence they were united in the one control group as mentioned earlier. Also, ω'_Qs from the control samples were found not significantly different from the ones of the diabetic foot/leg samples. From these results, it can be assumed that the degree of order in control and diabetic skin is the same.

3.4.2.2 TQF spectroscopy

This Subsection presents the results of TQF spectroscopic measurements of the skin samples. Statistical differences between different categories of samples (abdomen vs foot in the control group, the control vs diabetic group) were examined. Furthermore, TQF T_{2long} values were compared with the values of T_{2long} obtained from CPMG.

A representative TQF spectrum of a skin sample obtained from the abdomen of a control patient at $\tau = 1.615$ ms is shown in Figure 3.20(a). A typical dependence of the sodium signal intensity of the real part of the spectrum on the preparation time τ is shown in Figure 3.20(b). The red curve represents a fit to the equation [3.12]. The relaxation time T_{2short} and the residual quadrupolar interaction ω_Q' obtained from the fitting of the DQF-MA build-up curve were used as fixed parameters in the fitting to obtain T_{2long}.

The values of T_{2long} with their errors and for every sample in the control and diabetic groups are summarized in Table C.1. Values of T_{2long} for control abdomen, control foot/leg and diabetic foot/leg samples were identified as random and normally distributed samples by the SR, KS, and JB tests. ANOVA did not reject the hypothesis of equal variances between the groups in comparison: control abdomen vs control foot/leg and united control vs diabetic. Therefore, two-tailed t-tests were performed to find a level of significance for differences between the groups. The mean values of T_{2long} with their standard deviations and separately for foot/leg and abdomen samples in the control and diabetic groups are summarized in Table 3.2 and also presented as bar charts in Figure 3.21 together with the results of the t-tests. No significant difference was found between the abdomen and foot/leg samples in the control group

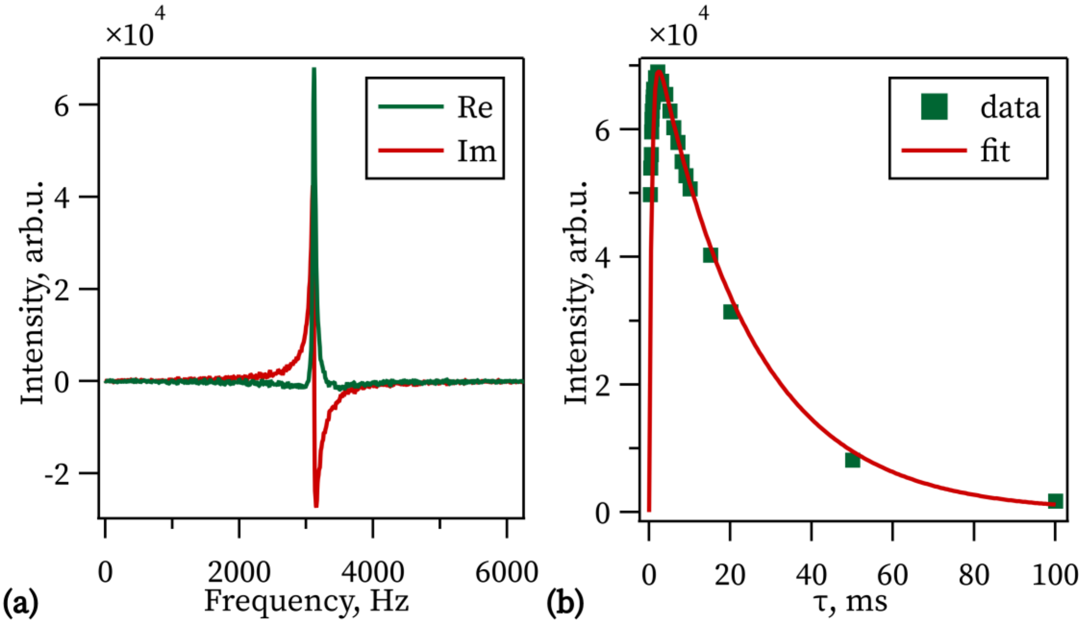

Figure 3.20. (a) TQF spectrum of ^{23}Na in a human skin sample obtained from an abdomen of a control patient at $\tau = 1.615$ ms. (b) ^{23}Na signal amplitude measured by TQF pulse sequence as a function of the preparation time τ – a build-up curve, for the same skin sample. The data was fitted to equation [3.12].

Table 3.2. Summary of ^{23}Na mean T_{2short}, T_{2long} and ω'_Q values with their SD obtained from fitting of sodium CPMG, DQF-MA and TQF data. Values are presented for the control and diabetic patients, abdomen and foot/leg samples separately.

Experiment	Patient group	Location	T_{2short}, ms	T_{2long}, ms	ω'_Q, Hz
CPMG	Control	abdomen	0.88±0.16	13.77 ± 0.85	-
		foot/leg	0.89±0.23	14.59 ± 1.14	-
	Diabetic	foot/leg	0.79±0.12	18.66 ± 1.39	-
DQF-MA/ TQF	Control	abdomen	0.80±0.21	23.42 ± 3.10	111.60±182.40
		foot/leg	1.05±0.14	25.81 ± 1.20	74.30±46.26
	Diabetic	foot/leg	0.81±0.25	27.42 ± 3.52	87.94±79.42

(Figure 3.21(a)), therefore, these samples were combined in one control group and compared with the diabetic foot samples (Figure 3.21(b)). T_{2long} values were found in the range of 20.5-33.8 ms. T_{2long} values of the diabetic group were found to be increased relative to the control group by about 11% ($p < 0.05$).

To validate TQF T_{2long} fitting results, values of T_{2long} were also determined by CPMG (Subsection 3.4.1.1). Table 3.2 shows fitting results of the TQF build-up

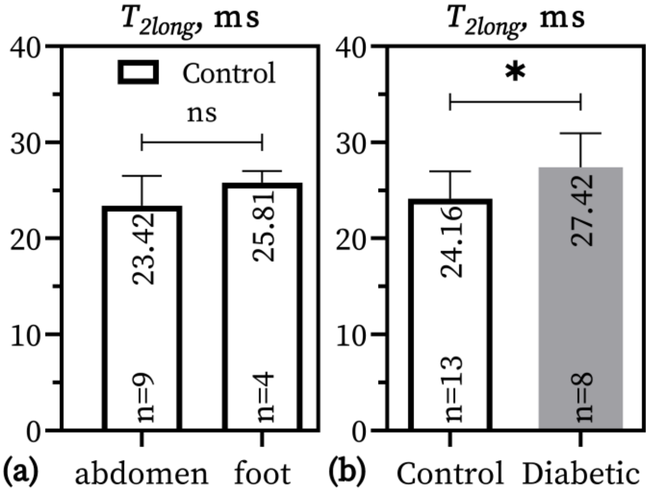

Figure 3.21. (a) Summary of sodium mean T_{2long} values with their SD obtained from fitting of sodium TQF build-up curves with eq. [3.12] for the abdomen and foot/leg samples in the control group. (b) Control group contains both skin locations and is compared with the diabetic patients. *$p<0.05$, ns – nonsignificant.

curves compared with T_{2long} values from CPMG. The former ones are larger by 50-87%.

As in the case of CPMG, TQF spectroscopy was executed without the slice selection and the obtained signal is a superposition of all sodium participating in slow motion

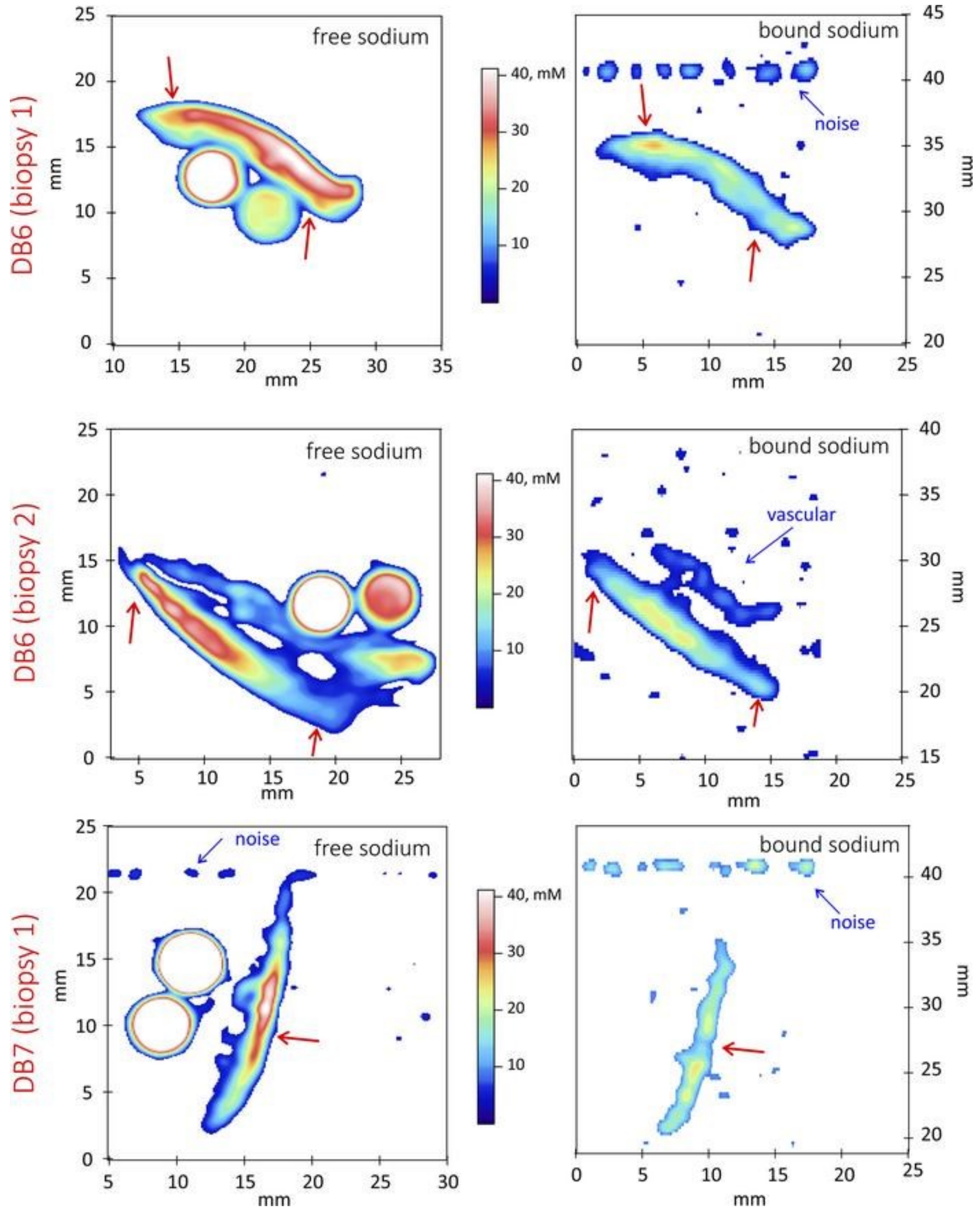

Figure 3.22. Evaluation of free and bound sodium concentration obtained from sodium imaging with saline standards for 3 skin samples gathered from 2 different patients. Free and bound sodium are denoted by red arrows, suggesting heterogeneity in sodium deposition in the skin. Additionally, the right middle panel depicts the bound sodium in the endothelial tissue of a large blood vessel. Blue arrows highlight the incidental noise detected at sodium frequency. Sodium levels are determined within ± 7 mM using saline standards. Reproduced from (Hanson et al., 2021).

across the skin sample. To visualize the location of this slow-moving sodium in the skin, TQF imaging can be performed (Hanson et al., 2021). TQF images of some diabetic samples are presented in Figure 3.22. These samples were scanned with calibration phantoms that were the water solutions of NaCl. The calibration phantoms cannot be seen on the TQF images as the triple quantum filtration suppresses motionally narrowed sodium in saline solutions. The signal from the phantoms hereby serves as an internal check for monitoring the filtering efficiency of the TQF sequence. In addition, it can be seen that bound (slow-moving) sodium collocates with free sodium in the dermis (Figure 3.22) (Hanson et al., 2021). This makes the TQF signal more sensitive to sodium in the dermis than to the other surrounding tissues like subcutaneous fat and physiological fluids.

3.5 Discussion

In this Chapter, a variety of methods were used to characterize human skin from the control patients, as well as patients suffering from type 2 Diabetes Mellitus. This section discusses the results of the main findings of this Chapter. To the best of the author's knowledge, single quantum and multiple quantum spectroscopy were implemented on human skin samples *ex vivo* for the first time in a preclinical 9.4 T Bruker spectrometer. Firstly, ^{23}Na transverse relaxation rates, T_{2short} and T_{2long}, were measured by CPMG and compared with results obtained with DQF-MA and TQF spectroscopy. Secondly, residual quadrupolar interaction constant ω_Q and T_{2short} of sodium involved in anisotropic motion were measured for human skin samples for control and diabetic cases by DQ-MA filter. Thirdly, TQF spectroscopy was performed to determine T_{2long} of sodium in the skin. All the measured parameters were compared between different skin locations and between patients with T2DM and their control counterparts.

3.5.1 Single quantum spectroscopy

3.5.1.1 CPMG

One of the main findings of our current research is that sodium T_{2long} determined from CPMG decay is longer in the skin of patients with T2DM compared to control patients. Regardless of age, weight, sex of the patients, location of the skin and other preexisting conditions, skin sodium T_{2long} has appeared to be a sensitive indicator of the presence of T2DM. Effects of patients' parameters listed in Table 3.1 and medication on sodium relaxation times are a subject of future investigations.

Deviation of the experimental data from the monoexponential decay is clearly shown in Figure 3.13((b) and (c)). The representation of the data on a semilogarithmic scale validates the biexponential fitting model described by eq. [3.8]. In addition, the R^2-statistics of the biexponential fit of the data in the original scale is higher than the one of the linear fit (eq. [3.13]) of the data in the semilogarithmic scale.

As the CPMG experiment was performed without the slice selection, i.e. the signal is obtained from the whole sample, measured values of T_{2short} and T_{2long} are superpositions of relaxation times arising from different domains: intracellular and extracellular sodium within the dermis and epidermis, fat and liquid phases.

It can be seen from Figure 3.11 that skin possesses a type "c" spectrum as no splitting can be observed. Type "c" can be obtained at a certain exchange time between type "a" sites and type "d" domains in a Chan discrete exchange model (Springer, 2007). Type "d" domains can be represented by physiological fluids, while type "a" sites may arise from the interaction of sodium ions with orientated macromolecules (GAGs, PGs, collagen, etc.). However, the magnitude of C_Q is not high enough for a full splitting to be observed. For cartilage, it was found that anisotropy experienced by sodium ions mainly comes from collagen fibres (Eliav & Navon, 1994). Cartilage was shown to have regions with high parallelism of collagen fibres (Bi et al., 2005) in contrast to the skin, whose collagen fibres have a more random orientation (Van Zuijlen et al., 2003). Overall, due to less ordering compared to the cartilage tissue, skin possesses a sodium spectrum between the types "c" and "b".

3.5.2 Multiple Quantum Spectroscopy

This section discusses the results of Double Quantum with Magic Angle spectroscopy (Subsection 5.1.2.1) and Triple Quantum filtered spectroscopy (Subsection 5.1.2.2).

3.5.2.1 DQF spectroscopy with Magic Angle

DQF spectroscopy with magic angle is a unique tool to study the residual quadrupolar couplings in loosely ordered samples like biological tissues. Compared to the standard DQF experiment, the DQF-MA pulse sequence detects a signal only from satellite transitions, as the contribution of the tensor $\hat{T}_{3,-1}$ is filtered out, allowing observation of the development of $\hat{T}_{2,\pm1}$ coherences arising exclusively from anisotropic environments (Eliav & Navon, 2016a).

Another method which is widely used to study quadrupolar couplings is the quadrupole echo pulse sequence (Duer, 2002). However, it is mainly used for nuclei with $I = 1$ as it fully refocuses the quadrupolar interaction. It also can be used for $I = 3/2$ nuclei but some considerations need to be taken into account (Eliav & Navon, 1995). The quadrupole echo is widely used in solids, crystal-like or powder samples which can be characterized by a slow exchange between different domains: $\bar{\omega}_Q\tau_e \gg 1$, where τ_e is time of the ion being found in a given domain (Springer, 2007). However, to study more complex systems where not all compartments contain non-zero $\bar{\omega}_Q$, DQF-MA is more appropriate because it records the dynamic of only satellite transitions and depends solely on T_{2short} and $\bar{\omega}_Q$ (Woessner & Bansal, 1998).

According to the eq. [3.2], the signal intensity of the DQF-MA spectrum can be measured as a function of the evolution time τ. This type of measurement eliminates the problem of losing the short component of the relaxation time due to the dead time of the spectrometer or a probe (Wimperis, 2011). Therefore, the measurement vs τ was chosen in this thesis.

Since the DQF-MA experiment relies on a flip-angle effect to selectively observe sodium ions involved in anisotropic motion, its performance can be significantly affected by pulse imperfections and B_0 inhomogeneities. Other versions of the DQF-MA pulse sequence where only the last or penultimate pulse is set as 54.78° were shown to have a better performance in the sense of suppression of $\hat{T}_{3,\pm2}$ in the case of the inhomogeneous B_0 (Gast et al., 2018). However, they are more sensitive to errors in flip angles than the classical sequence with $\theta_2 = \theta_3 = 54.78°$. The 180° pulse can be used in the middle of the preparation time τ to refocus B_0 inhomogeneities but it could also be a source of unsatisfactory suppression of third-rank tensors.

It is reported in this thesis that the short component of the sodium relaxation time T_{2short} of the foot/leg is significantly longer than T_{2short} of an abdomen sample. Hence, care should be taken in choosing a skin location when comparing the control group with a case of pathology. This result shows that skin from the abdomen and foot/leg has different viscous properties. These body parts experience different mechanical loads and therefore have different thicknesses of the dermis (Oltulu et al., 2018). The skin dermis contains much fewer cells than the epidermis and the extracellular compartment of the dermis has a sodium concentration (about 140 mM) much higher than the intracellular compartment (approximately 10 mM) (Alberts et al., 2015). We can assume that the sodium signal in our measurements is dominated by extracellular sodium. Therefore, we can suspect that the skin of different body parts has different densities of macromolecules' network (collagens, PGs and GAGs) to match the mechanical load.

Although the values of T_{2short} for the foot/leg samples from the control and diabetic groups are not significantly different from each other, there is a trend of decreasing T_{2short} for the case of Diabetes Mellitus. Similarly with the human articular cartilage where a decrease in T_{2short} was found to be associated with proteoglycans' depletion (Insko et al., 1999; Keinan-Adamsky et al., 2010), one can assume that the shortening of T_{2short} in the skin of diabetic patients might indicate a prevailing PG degradation.

The abdomen samples from the control patients were found not significantly different from the foot/leg samples from the diabetic patients. This fact diminishes the differentiation between the abdomen and foot/leg skin. Hence, skin location might be an important criterion when comparing sodium dynamics in pathological cases and their control counterparts.

As the DQF-MA signal is generated exclusively from the satellite transitions relaxing with T_{2short} without any contribution from T_{2long}, thence the DQF-MA experiment is more univocal in the determination of T_{2short} than CPMG. Also considering that the echo time in CPMG $TE = 2$ ms is longer than the mean value of T_{2short} (< 1.05 ms), the CPMG train of echo integrals does not have enough data points, especially at the beginning of the decay, to resolve T_{2short} adequately compared to the DQF-MA build-up curve. Therefore, the difference between the two skin locations for T_{2short} obtained from CPMG could not be observed.

It was found that ω_Q's from the abdomen and foot in the control group belong to the same distribution. As the value of ω_Q' indicates the extent of macromolecular organization within the tissue (Eliav et al., 1992), based on these findings, it can be inferred that the level of order in both control and diabetic skin is comparable. However, there is a trend of diminishment for the foot samples. This result supports the finding of the elongation of the leg T_{2short} compared to the abdominal T_{2short}. In the DQF-MA spectrum, ω'_Q corresponds to a difference between peaks in frequency for every value of the creation time τ (Navon et al., 2001), and it was observed that it changes with τ (Figure 3.18) due to the heterogeneity of the skin and the distribution of quadrupolar interactions within the tissue. Therefore, ω'_Q obtained from the fit of the build-up curve is a weighted average of all ω'_Q in the investigated system (Keinan-Adamsky et al., 2010). Therefore, the difference between the two skin locations might not be properly resolved.

3.5.2.2 TQF spectroscopy

TQ filter gives the highest signal intensity among other multiple-quantum filters (Springer, 2007), but its ability to discriminate the quadrupolar interaction when $T_{2short} \neq T_{2long}$ and type “b” spectra from type “c” ones is poor (Wimperis, 2011), as the TQF signal originates regardless of the presence of the electric field gradient (Van Der Maarel, 2003). Therefore, in this thesis, the TQF experiment was used to determine only the T_{2long} component.

Multiple-quantum filtration (DQF-MA and TQF in this case) gives T_{2short} and T_{2long} which are the same relaxation characteristics obtained from single-quantum experiments like CPMG. The main disadvantage of the MQF is its much lower SNR compared to ordinary SQ experiments. Nevertheless, the use of MQF grants many advantages. The first one is that the ability to record the sodium signal by DQF-MA and TQF shows a piece of direct evidence that the sodium ions in the skin are outside the extreme-narrow motion regime. Moreover, DQF-MA specifically demonstrates that some sodium is involved in RQI. Second, the function $f_{13}^{(\pm1)}$ which contains the subtraction of one exponential function from another has more turning points than the $f_{11}^{(\pm1)}$ function composed of a sum of two exponents. Therefore, it is believed that $f_{13}^{(\pm1)}$ should give a more reliable fit than $f_{11}^{(\pm1)}$ to separate two relaxation components, especially when T_{2short} and T_{2long} are close (however, it is not the case here). Third, a baseline of the MQF spectrum is usually less distorted than one of the SQ spectrum because the FID of the former starts from zero (Wimperis, 2011).

One can see from the eq. [3.4], the TQF spectrum signal intensities can be recorded as a function of the evolution time τ. This type of measurement eliminates the problem of losing T_{2short} due to a dead time of the spectrometer or a probe (Wimperis, 2011). Therefore, the measurement vs τ was performed in this thesis.

However, performing a multiple-quantum experiment or even an ordinary spin-echo for *in vivo* or *ex vivo* samples can be tricky due to the B_1 inhomogeneities. Usually, a nominal 180° pulse is used in the middle of the evolution interval τ to prevent the measured relaxation times from being compromised by an inhomogeneous B_0 field. But in real experimental conditions, a 180° flip angle may not be reached for the whole sample. The distribution of flip angles occurs within the sample and apart from the desired coherence pathway $p = \pm 1 \rightarrow \mp 1$, other pathways will contribute to the signal. A refocusing pulse with a flip angle $\theta \neq 180°$ still forms an echo, but the density operator components $\hat{T}_{1,\pm 1}$ and $\hat{T}_{3,\pm 1}$ will have different contributing amplitudes. This results in the triexponential transverse relaxation with rates $R_f^{(1)}$, $R_s^{(1)}$ and $\frac{1}{2}\left(R_f^{(1)} + R_s^{(1)}\right)$ which relative amplitudes depend on the actual flip angle θ of the refocusing pulse that makes them spatially inhomogeneous (Brown & Wimperis, 1994). A solution for TQ filtration specifically might be not to use a 180° pulse but to introduce a specific phase cycle that eliminates all unwanted coherence pathways except $\Delta p = \pm 2$.

The problem of contamination described above may serve as a possible explanation for the mismatch of T_{2long} values obtained by CPMG with the ones gained from TQF build-up fitting. Another possible reason can be a structure of the fitting functions for the CPMG decay and the TQF build-up curve (eq. [3.8] and [3.12] correspondingly). Following the second paragraph of this section, eq. [3.12] have more extrema than eq. [3.8] (one point vs none) which is believed to give a more reliable fit. Also, an offset term is introduced in the CPMG fitting equation [3.8] to compensate for sodium relaxation in a physiological fluid phase. A contribution of this offset towards the maximum intensity of the CPMG train is determined automatically, not especially regulated and it is much larger than the noise. This can lead to a shorter T_{2long} than its true value which is unknown. In contrast, the TQF build-up fitting function [3.12] does not contain any offset as the sodium signal from the liquid phase does not pass the filter. These make the TQF experiment superior to CPMG in studying sodium involved exclusively in slow anisotropic motion in the skin. In addition, the CPMG train might also not be long enough to observe the whole echo decay. In the described experiments, the signal evolution is measured up to 64 ms. In comparison, TQ coherence evolution is tracked up to 100 ms, almost twice as long as in CPMG. Thereby, an unmeasured signal would be masked in the offset term. As a consequence, T_{2long} obtained from CPMG will be shorter than from TQF.

In this work, it was shown that sodium's long relaxation rate T_{2long} obtained by TQF spectroscopy is longer in diabetic patients by ≈ 11% relative to control patients and this difference is significant. As it was discovered with the human articular cartilage where lengthening of T_{2long} was found to occur with proteoglycan degradation (Insko et al., 1999), we may presume that the reduction of the binding capacity of GAGs in the skin of diabetic patients leads to an increase in T_{2long} in the skin due to deprivation of proteoglycans from the skin tissue matrix in the case of T2DM. It is also known that the collagen network in diabetic skin is structurally different from one in healthy skin (Argyropoulos et al., 2016). It may be assumed that an impaired organization of the collagen matrix can be an additional mechanism of change in sodium relaxation parameters (Eliav & Navon, 1994).

3.6 Conclusion

The main findings of this Chapter are: (1) sodium relaxation time T_{2short} measured by the DQF-MA sequence can serve as a probe for a skin location on a human body; (2) the long component of sodium relaxation time T_{2long} (and potentially T_{2short} and ω_Q') in the skin may serve as a biomarker for type 2 Diabetes Mellitus. The latter can be explained in several ways: (a) there is a reduced density of the macromolecular network and its damaged architecture in ECM of the skin of diabetic patients; (b) extracellular volume fraction is increased in the skin of patients with T2DM compared to their control counterparts. In the former case, macromolecule maintenance might be shifted towards proteoglycan degradation that changes the 3D collagen organization compared to control/healthy skin. In the latter case, the sodium balance between intra- and extracellular compartments could be disturbed. Both of these situations are indicators of tissue pathology (skin in this case) that opens a new insight into the pathophysiology of type 2 Diabetes Mellitus.

4 Sodium NMR in the inhomogeneous magnetic field of 0.5 T

A 24-mm probe used for experiments in this Chapter was developed by Dr G. Pavlovskaya. Using this probe, sodium measurements were performed for several phantoms with different concentrations of NaCl: aqueous solutions of saturated, 0.93 M, 0.5 M, 0.25 M and 0.125 M NaCl under international collaboration (Unpublished data, 2018). The measurements were conducted at 6.1-6.108 MHz in the magnetic field of 0.542 T with the gradient G_0 = 4.7 ± 0.2 T/m. For the saturated NaCl, SNR = 81.7 was achieved in 6 minutes. For 0.93 M NaCl, SNR = 42 was acquired in 21.3 min. For the sample 0.5 M NaCl, SNR = 13.5 was obtained in 20.5 min. For the 0.25 M aqueous solution of NaCl, SNR = 14 was gained in 32 min. For the lowest sodium concentration, 0.125 M NaCl, SNR = 7.8 was obtained in 1 hour 22 min. In addition, T_2 relaxation measurements were performed for the saturated NaCl phantom and 0.93 M NaCl water solution. T_2 was obtained 37.5 ± 1.4 ms for the saturated NaCl. For 0.97 M NaCl water solution, T_2 was found 41 ± 18 ms. The results mentioned above helped in developing an idea of constructing a wider probe to perform sodium measurements in a similar set of phantoms to increase SNR and reduce the measurement time.

Magnetic field measurements of the Oxford magnet in the z direction were performed by Mrs D. Fomina together with Dr Evgeny Petrovsky under international collaboration. Magnetic field measurements in the xy plane and simulations were performed by Mrs D. Fomina. A 40-mm probe and sodium chloride phantoms for this probe used for experiments in this Chapter were made by Mrs D. Fomina. Experiments with the 40-mm probe and data processing of all experiments were performed by Mrs D. Fomina. In addition to the 40-mm coil mainly used for the sodium measurements, the 24-mm probe (Unpublished data, 2018) was used for purposes of comparison.

4.1 Introduction

As described in Sections 3.1.1-3.1.2, sodium performs a variety of roles in a human organism. Mechanisms of sodium regulation in the human skin are not completely understood and they are of great interest for investigation. Sodium NMR has been shown to be a useful and powerful tool for studying sodium in skin tissue. However, performing sodium spectroscopy or imaging to study skin *in vivo* using conventional whole-body MRI scanners seems to be impractical due to the small thickness of the tissue. Also, in some situations, a patient cannot be put inside an MRI scanner due to some physiological conditions or external equipment such as a haemodialysis machine. But, as described in previous sections, it might be very important to monitor sodium concentration for efficiency and effectiveness of the intervention in patients with several diseases like hypertension and type 2 Diabetes Mellitus. To overcome the practical difficulties of measuring skin sodium with whole-body MRI scanners, portable NMR devices can be developed. The portable NMR devices should have a size and weight of several orders of magnitude reduced compared to the MRI scanner and they must be mobile to be delivered to a patient. These features can be achieved by using permanent magnets to create the main polarizing magnetic field. The idea of a portable NMR device was developed from the inside-out NMR approach where a probe and the permanent magnet are located near (or inside) the sample and not the sample inside the magnet.

Firstly this inside-out NMR approach was introduced in 1991 and it was used in borehole investigations, which are of considerable importance in oil well logging and drilling (Coates et al., 1999). Later the NMR-MOUSE (MObile Universal Surface Explorer) was built in 1995 (Figure 4.1): a small single-sided NMR sensor weighting of the order of 2.5 kg with a magnetic field gradient higher than 10 T/m at a field strength of about 0.5 T was discovered to be useful for materials testing, measuring signal of protons and its relaxation (Eidmann et al., 1996). Later, similar single-sided sensors were constructed. A shim unit was introduced to the NMR-MOUSE to increase an exciting volume by reducing the gradient, which also makes the field more homogeneous in a plane perpendicular to the gradient (Landeghem et al., 2011). The permanent magnets create a strong magnetic field gradient which is very useful in acquiring high-resolution 1D profiles of materials. On the other hand, the gradient reduces sensitivity which is of extreme importance when measuring nuclei other than protons, for instance, ^{23}Na. In this regard, special methods should be used to increase the sensitivity and, consequently, SNR. They are described in the following sections.

To study solids and solid-like materials in inhomogeneous magnetic fields, very large gradients need to be applied to deal with broad spectral lines. One of the first techniques developed for this purpose was STRAFI – STRAy Field Imaging (McDonald & Newling, 1998). A fringe field of a superconducting magnet serves as a polarizing B_0 field (Figure 4.1). The signal is collected from a very thin slice defined by the naturally created large magnetic field gradient and the length of an RF pulse (eq. [4.1]). If needed, a sample can be mechanically moved through the sensitive slice to obtain 1D profiles or spatial maps of other parameters like T_1, T_2 and diffusion coefficients. The magnetic field gradient is usually so large that it generally overpowers all couplings (dipolar, quadrupolar) and interactions in the spin Hamiltonian, therefore STRAFI is very useful for imaging solids.

Within the region of interest in a STRAFI experiment, the high curvature of the magnetic flux does not allow one to achieve the best resolution. Specifically for studying planar samples, new geometries of permanent magnets were developed to produce particularly flat excitation slices and homogeneous gradients within them. The planar samples include a broad spectrum of materials, including polymer films, paints, and human skin. This new kind of type of imaging system was called GARField (Gradient At Right angles to Field) (Glover et al., 1999) (Figure 4.1). GARField uses specifically designed shapes of the permanent magnets, namely magnets with curves poles, which generate lines of magnetic flux running parallel to the sensitive plane with constant magnitude. The magnetic field gradient is orthogonal to the sensitive plane.

Albeit, both techniques, NMR-MOUSE and GARField, can be attributed to STRAFI. However, while STRAFI utilizes the stray field of a superconducting magnet, NMR-MOUSE and GARField use permanent magnets as sources of the polarizing magnetic field. In addition, the mutual direction of the main magnetic field $\vec{B}_0$ and its gradient

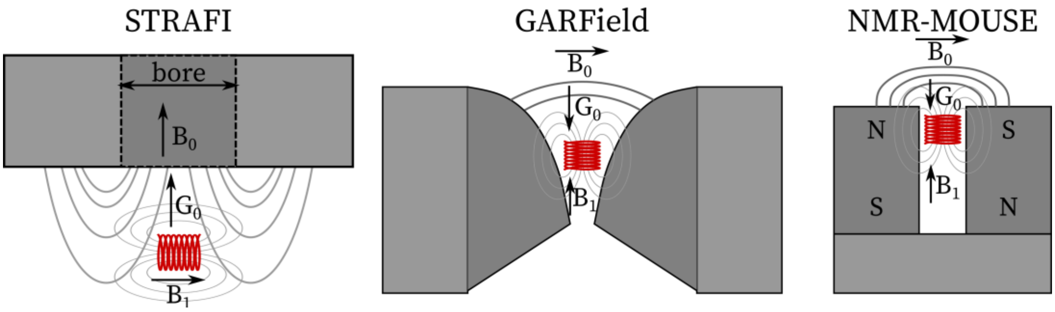

Figure 4.1. NMR techniques based on inhomogeneous fields: STRAFI, NMR-MOUSE and GARField. Field lines of the main magnetic field $\vec{B}_0$ are shown in dark grey, and ones of the $\vec{B}_1$ field of the coil (red) are shown in light grey. Directions of $\vec{B}_0$, its gradient $\vec{G}_0$ and $\vec{B}_1$ are indicated by arrows.

$\vec{G}_0$ is different in these imaging systems: in STRAFI $\vec{B}_0$ is parallel to $\vec{G}_0$, when in the systems with permanent magnets $\vec{B}_0$ is perpendicular to $\vec{G}_0$ (Figure 4.1).

4.1.1 NMR methods in inhomogeneous fields

This Subsection describes methods that are commonly used to perform NMR measurements in the inhomogeneous magnetic field B_0. A more extensive description can be found in (Casanova et al., 2011).

In the inhomogeneous magnetic field B_0, the gradient G_0 determines the thickness of the excited slice Δz as in eq. [4.1]:

$$\Delta z = \frac{\Delta f}{\gamma G_0}, \qquad [4.1]$$

where Δf is an excitation bandwidth and γ is a gyromagnetic ratio of a nucleus. Excitation bandwidth Δf is inversely proportional to the pulse length (PL), therefore, all applied RF pulses become selective. A non-uniform spatial distribution of both B_0 and B_1 leads to a non-uniform spatial distribution of flip angles across the investigated sample (eq. [3.5]): if it is 90° for spins at the centre of the excited slice, it is quite different at the edges of the slice. With increasing the frequency offset, the efficacy of excitation decreases fast. Therefore, the observed total magnetization may be regarded as a complex superposition of the responses of the spins to a varying flip angle and phase. This results in that not all longitudinal magnetization of the sample experiences a 90° rotation and there is some residue along the z-axis. This residual longitudinal magnetization relaxes with T_1 and it is not influenced by the presence of a B_0 gradient, while a created transverse magnetization relaxes with T_2 and it is additionally dephased by the field gradient G_0. This creates an undesired interference of different coherence pathways. Unwanted coherence pathways can be eliminated by specially developed phase cycles.

Due to a continuously present gradient that creates a distribution of resonance frequencies, additional spreading of the transverse magnetization occurs during the application of the RF pulse, thus a signal appears attenuated already at the end of the pulse. Moreover, the xy magnetization dephases further after the pulse and the FID decays very fast, in time of the order of the dead time of the RF probe. Consequently, in inhomogeneous fields, the FID cannot be detected in a simple “pulse-acquire” experiment.

A refocusing of the dephased magnetization is possible by applying at least two pulses with a time interval τ between them: the formation of an echo will occur at the time 2τ. In inhomogeneous fields, the following pulse sequences are widely used: the quadrature echo (or solid echo), spin echo and the Carr-Purcell-Meiboom-Gill (CPMG) (Callaghan, 1991; McDonald, 1997).

4.1.1.1 Spin echo

Originally a spin echo was discovered by Hahn who used two 90° pulses (Hahn, 1950). But later Carr and Purcell proposed to use a 180° pulse for refocusing which helped to obtain a higher signal (Carr & Purcell, 1954).

A timing diagram of the spin echo pulse sequence is presented in Figure 4.2. In stray field experiments, it is more advantageous to double the amplitude of the 180° RF pulse with respect to the 90° pulse and keep the same length. To a sufficient extent, this provides an equal bandwidth of the pulses and, therefore, maintains the same excitation volume for each pulse. In some cases when an application of high RF power is limited, it consequently leads to a reduction in power for the 90° pulse (assuming the highest power for the 180° pulse) which results in longer pulses, which in turn excite narrower slices in the sample.

Due to the dephasing of the magnetization during the first 90° RF pulse, one can define a zero-time point for the sequence at the centre of the 90° pulse. As an echo is generated at a time of $\tau + \tau_p/2$ after the refocusing pulse, where τ is the distance

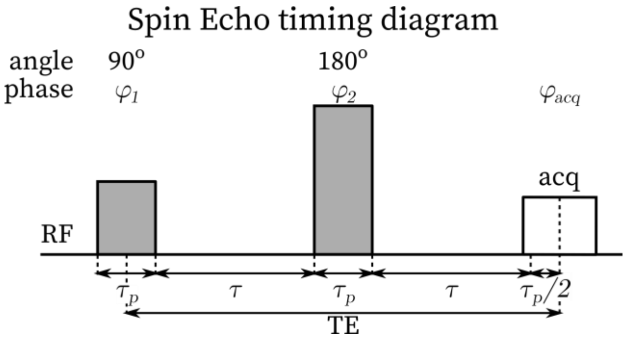

Figure 4.2. A timing diagram of the spin echo pulse sequence. The 90° and 180° pulses have the same length τ_p, but amplitude of the 180° pulse is twice of that of the 90° pulse. Echo forms at a time TE.

between pulses (Figure 4.2), the sequence is symmetrical about the centre of the 180° pulse and the echo time TE is equal to $\tau + \tau_p$.

As mentioned above, in the presence of a constant gradient of the static magnetic field the resonance offset created by the gradient defines the effect produced by an applied RF pulse. Therefore, as for the 90° pulse, only on-resonance spins experience a perfect 180° rotation. Even assuming a homogeneous B_1, during a real experiment, there is a simultaneous detection of signals with different frequencies that interfere strongly with each other in the time domain. This results in a detectable echo bandwidth about twice as small as the excitation bandwidth of the RF pulse (Casanova et al., 2011). As the latter depends on pulse duration, it is assumed that the former also depends on the length of the RF pulse. A quite accurate empirical assumption is that the echo width is approximately equal to the pulse length. Consequently, an acquisition window should be about the length of the excitation RF pulse to maximize the sensitivity (Casanova et al., 2011).

The spin echo pulse sequence is an important method especially to measure very short T_2 relaxation times of the order of several dead times of the RF probe. The performance of the spin echo is not affected by magnetic field inhomogeneities, resonance offsets, and distributions of flip angles across the sample, thereby a pure T_2 decay can be measured as in homogeneous fields. However, in the case of liquid samples in the presence of a strong static gradient, pure T_2 is heavily affected by diffusion and errors due to imperfect 180° pulses (Mitchell et al., 2006). In the presence of diffusion, the signal dependence on TE can be described as in eq. [4.2] (Casanova et al., 2011):

$$S(TE) = S_0 \exp\left(-\frac{TE}{T_2} - \frac{1}{12}\gamma^2 G_0^2 D \cdot TE^3\right), \qquad [4.2]$$

where D is a diffusion coefficient.

4.1.1.2 CPMG

In most cases, a very short echo time ($\ll T_2$) can be set in a spin echo experiment that allows one to acquire a multitude of echoes after the application of a train of refocusing pulses with the appropriate phase. This sequence of pulses is CPMG, and it is used to measure T_2 in a single shot (Meiboom & Gill, 1958). To avoid an accumulation of distortions arising from imperfect RF pulses and the influence of the resonance offset,

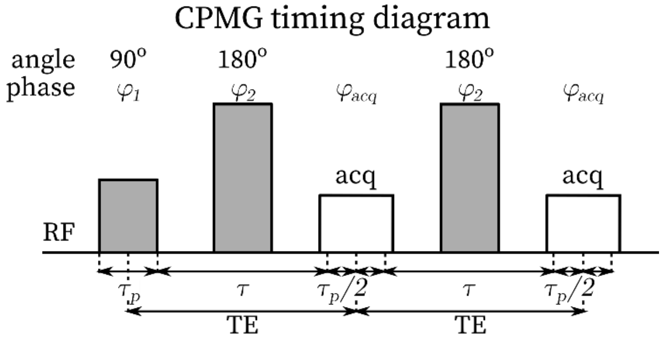

Figure 4.3. Timing diagram of the CPMG pulse sequence. Only two echoes are shown.

the phase of the refocusing pulses should be shifted by $\pi/2$ with respect to the first 90° pulse. This makes the CPMG sequence very robust either in homogeneous or inhomogeneous fields. The timing diagram of the sequence is shown in Figure 4.3.

It was demonstrated that in inhomogeneous magnetic fields where a nonuniform spin excitation is generated, the echo signals detected during the refocusing train are a complicated superposition of coherence pathways that leads to a formation of direct, indirect and stimulated echoes (Goelman & Prammer, 1995; Hürlimann & Griffin, 2000). Imperfect pulses and distribution of flip angles in a sample create a magnetization that is stored along the z-axis in addition to the desired magnetization in an xy-plane. As this longitudinal magnetization is a subject of T_1 relaxation and the remaining transverse magnetization relaxes with T_2, an experimentally measured decay time is T_{2eff} which contains contributions from both T_1 and T_2 relaxation times. If we define rotation of the magnetization around an effective axis $\hat{n}(\Delta\omega_0, \omega_1)$ which depends on the resonance offset $\Delta\omega_0 = \omega_{rf} - \gamma B_0$ (ω_{rf} is the frequency of an RF pulse) and amplitude of the RF pulse $\omega_1 = \gamma B_1$, and do not consider transient effects affecting the first echoes, a CPMG signal decay can be approximated by eq. [4.3]:

$$\frac{\vec{M}(mTE)}{M_0} \simeq \left\{ \int \left(\vec{M}_{xy}^{0+} \cdot \hat{n} \right) \hat{n} \cdot f(\Delta\omega_0) d(\Delta\omega_0) \right\} \exp\left(-\frac{mTE}{T_{2eff}} \right), \qquad [4.3]$$

where m is an echo number, $\vec{M}_{xy}^{0+}$ is an initial complex magnetization $M_{xy}(t = 0) = M_x + iM_y$, $f(\Delta\omega_0)$ is an offset distribution function over the sample, and T_{2eff} is defined as in eq. [4.4] (Hürlimann & Griffin, 2000):

$$\frac{1}{T_{2eff}} = \langle n_\perp^2 \rangle \frac{1}{T_2} + \langle n_z^2 \rangle \frac{1}{T_1}, \qquad [4.4]$$

where the angle brackets indicate an average of the square of the projections of $\hat{n}$ onto the xy-plane and the z-axis correspondingly.

An accumulating interference of coherence pathways leads to a signal decay that differs from a monoexponential decay, especially for long decay times. This effect is more pronounced in situations with an increasing difference between T_1 and T_2. However, even for a large T_1/T_2 ratio, an error in estimating true T_2 from a fitting of a CPMG echo train does not exceed 12% (Goelman & Prammer, 1995). This shows that even in the presence of a strong static gradient of a magnetic field, the CPMG pulse sequence can be successfully used to measure the transverse relaxation time. Also, the error in determining T_2 can be reduced if considering only a part of the echo decay of the order of T_2.

As in the case of the Hanh echo, the signal decay in CPMG is additionally attenuated by diffusion. When the gradient G_0 is not very high and only direct echoes contribute to the signal, the signal depends on TE in the following manner as in eq. [4.5]:

$$S(mTE) = S_0 \exp\left\{-\left(\frac{1}{T_2} - \frac{1}{12}(\gamma G_0 \cdot TE)^2 D\right) \cdot mTE\right\}. \qquad [4.5]$$

The equation [4.5] shows that the increase in the static gradient and the diffusion coefficient shorten the signal decay measured by a CPMG sequence in the case of self-diffusion of molecules. A way to reduce this shortening is to decrease the echo time TE. However, this can be accomplished only up to a certain extent, as the stronger the gradient is, the shorter the signal decay is.

When a CPMG sequence is implemented in inhomogeneous field conditions, the RF pulse length and the minimum echo time must be optimized carefully. In these conditions, the acquired signal intensity is a value averaged over the sensitive volume, and the pulse duration needs to be set to maximize the signal intensity which can be obtained by integrating the echoes (Mitchell et al., 2006). The B_1 distribution generated by the RF coil defines the position of the maximum intensity. Regarding the echo time, the maximum number of echoes should be obtained during the echo train to maximize the sensitivity and increase SNR. It can be achieved by setting the shortest TE but one needs to avoid signal contamination arising from the dead time of the resonance circuit.

The CPMG pulse sequence is a very powerful method to use in inhomogeneous fields as it is capable of measuring a wide range of transverse relaxation times and echoes can be summed up to increase SNR, especially when it is operated at the shortest echo time as mentioned earlier.

4.1.2 NMR in the inhomogeneous field for biomedical applications

Single-sided NMR has been shown to be useful in measurements of human tissues, especially skin and tendons. Skin depth profiling gives distributions of a proton T_2 and diffusion coefficient which helps to differentiate between different skin layers (Landeghem et al., 2011). T_2 relaxation time was measured in the different depths in the skin and Achilles tendon by NMR-MOUSE and served as an indicator for tissue differentiation *in vivo* (Miltner et al., 2003). It was shown that a high macroscopic order of tendon tissue causes orientation dependence of T_2 relative to $\vec{B}_0$ (Haken & Blümich, 2000).

Applying CPMG with different echo times allows one to obtain a different contrast between studied tissues. This technique was applied to measure depth profiles of the skin of the palm and forearm: the contrast between different skin structures (layers of epidermis and dermis) is obtained by diffusion weighting and the use of a specially designed weighting function (Casanova et al., 2006). It was shown that the dermis is more affected by diffusion than the epidermis. Obtained profiles show a thinner epidermis of the lower arm compared to the palm of the human body. The time evolution of the absorption of cosmetic creams into the skin was studied in both skin locations.

It is possible to miniaturize a permanent magnet and a coil to fit in a standard catheter to investigate the walls of the coronary arteries (Blank et al., 2005). A device like this might be useful to study vulnerable coronary plaques which are too small to be properly resolved by conventional MRI.

GARField imaging systems with specially shaped magnets to straighten the magnetic field profile were used to study skin hydration and the effects of different skin-care product ingredients on human skin *in vitro* and *in vivo* (Backhouse et al., 2004; Ciampi et al., 2011; Dias et al., 2003; McDonald et al., 2005). One-dimensional depth-resolved T_1, T_2 and self-diffusivity maps were obtained for the skin of several healthy volunteers *in vivo* (Ciampi et al., 2011; McDonald et al., 2005).

Applications of STRAFI were mainly developed in the area of solids and solidifying/drying materials (building materials, polymers and films), as the strong B_0 gradient allows one to overcome the problem of very broad spectral lines caused by short T_2^* relaxation times of the samples or quadrupolar couplings (Bodart et al., 1997; McDonald, 1997; Mitchell et al., 2006). Therefore, applications in biomedicine have been limited to teeth and bones (Baumann et al., 1993; Randall, 2011).

4.1.2.1 Sodium NMR in an inhomogeneous field

A single-sided NMR device was built to measure sodium in ancient objects of art to study salt disposition (Zia, 2016). Applying the inverse Laplace transform, one can study distributions of T_2 relaxation times in a sample that correlates with the pore sizes and degree of dissolution of sodium ions in water inside the pores. As the measurements were made with saturated salt solutions, high concentrations of sodium ions allowed one to perform signal measurements in an adequately fast manner (about 5 minutes) which gave $SNR \approx 4$. However, measuring sodium in a biological tissue faces several complications: several orders of magnitude lower sodium concentration and an appearance of short T_2 relaxation component which contributes to 60% of the signal and is hard to detect. In a range of concentrations close to ones in biological tissues, sodium quantification using a portable NMR sensor was performed in different types of cheese with sodium concentrations in a range of 0.18 – 1 g/100 g (Greer et al., 2019) which corresponds to 84-462 mM (considering an average density of cheese as 1.073 g/cm^3 (Iezzi et al., 2013)). To the best of the Author's knowledge, there are no sodium measurements performed by a portable NMR device on biological tissues *in vitro* or *in vivo* yet. Some preliminary work should be done to assess the feasibility of these measurements: estimation of a measurement time and size of an excited volume to achieve an optimal SNR.

4.1.3 SNR

NMR in inhomogeneous fields suffers from low sensitivity due to high field gradients. However, the sensitivity can be increased significantly, and measurement times can be decreased at the same time by applying multi-echo techniques like CMPG pulse trains. Echoes generated by these pulse trains can be summed up which gives an undeniable advantage compared to single echo methods like spin echo.

The sensitivity can be characterized by SNR. An analytical expression for SNR was extensively studied and given by (Hoult & Richards, 1976). However, in the single-sided NMR or STRAFI, objects under investigation can be much larger than the detecting coil. Therefore, instead of having a volume with a uniform B_1 across a sample, one should introduce a definition of a sensitive volume which depends on both B_1 and B_0 spatial distributions. Also, a delicate balance needs to be found between the strength of the polarizing field B_0 and its gradient: the stronger field enhances the sensitivity, but the higher gradient reduces the excitation volume. Also, off-resonance effects need to be taken into account. It needs to be found out to what extent these factors affect SNR.

Based on the expression of SNR given by (Hoult & Richards, 1976), a more general equation [4.6] can be obtained (Casanova et al., 2011):

$$SNR = \frac{N_V \gamma^3 \hbar^2 I(I+1)}{6\sqrt{2}(k_B T)^{\frac{3}{2}}} \cdot \frac{B_0^2}{\sqrt{\Delta f R}} \int_{V_s} \left(\frac{B_1}{i}\right)_{xy} \Gamma(B_0, B_1, \Delta f_L) dr^3, \qquad [4.6]$$

where N_V is the spin density in the unit volume, γ is a gyromagnetic ratio that defines nucleus sensitivity, $\hbar$ is a reduced Planck's constant, I is the nuclear spin, k_B is Boltzmann's constant, Δf is an acquisition bandwidth (inversely proportional to the acquisition time), Δf_L is an RF-circuit bandwidth, R is the resistance including the probe, the sample and electrical components of the transmit/receive tract of an NMR spectrometer, V_S is a sample volume, $\left(\frac{B_1}{i}\right)_{xy}$ is the component of the RF field per unit of current perpendicular to the magnetic field $\vec{B}_0$, and $\Gamma(B_0, B_1, \Delta f_L)$ is a dimensionless complex function of the signal response to a particular sequence of pulses (single pulse, spin echo, CPMG, etc.). A spatial dependence of Γ defines the sensitive volume. Spatial integration dr^3 is performed over the sample volume V_S.

The integral in eq. [4.6] can be solved numerically under several assumptions which are related to the single-sided sensor and/or STRAFI. In the case of a strong B_0 gradient, the excited volume V_{exc} is proportional to the excitation bandwidth of the RF pulse Δf_{exc} as in eq. [4.7]:

$$V_{exc} \cong V^* \Delta f_{exc}, \qquad [4.7]$$

where V^* is the magnetic field homogeneity factor which can be expressed as in eq. [4.8]:

$$V^* = \frac{l^2}{\gamma G_0}, \tag{4.8}$$

where l is the dimension of the RF coil in a plane perpendicular to the gradient G_0. V^* indicates a volume per frequency unit. Then, in the case of a homogeneous B_1 over the excited volume, one can obtain eq. [4.9]:

$$SNR = \frac{N_V \gamma^3 \hbar^2 I(I+1)}{6\sqrt{2}(k_B T)^{\frac{3}{2}}} \cdot \frac{B_0^2}{\sqrt{\Delta f R}} \cdot V^* \Delta f_{exc}(B_1, \Delta f) \left(\frac{B_1}{i}\right)_{xy}. \tag{4.9}$$

4.1.3.1 SNR in CPMG pulse sequence

The excitation bandwidth Δf_{exc} can be defined either by the length of RF pulses, the circuit bandwidth, or both. If all the pulses (90° and 180°) in the CPMG have the same length τ_p, then the bandwidth of the pulse sequence is defined as in eq. [4.10]:

$$\Delta \nu_0 = \frac{1}{2\tau_p}. \tag{4.10}$$

The CPMG bandwidth is twice as narrow as the bandwidth produced by a single pulse due to a mixture of different coherence pathways (Casanova et al., 2011). The number of echoes n_e that can be collected and summed up to increase SNR is limited by T_2 of the sample and the echo time TE. The minimum TE is limited by the dead time t_{dead} of the probe and acquisition time t_{acq}. The average of the echoes' amplitudes collected by the time of TE is approximately two-thirds of the initial echo amplitude, therefore, the SNR of the CPMG experiments can be expressed as in eq. [4.11] (Casanova et al., 2011):

$$SNR_{CPMG} = \frac{2}{3}\sqrt{n_e} \cdot SNR = \frac{2}{3}\sqrt{\frac{T_2}{2t_{dead} + t_{acq}}} \cdot SNR. \tag{4.11}$$

The dead time t_{dead} is the time needed for a voltage induced in the RF probe due to the application of the RF pulse V_{pulse} to decrease towards the level of an RMS voltage of the noise V_{noise} and it is defined by the circuit parameters as L (inductance) and R (coil resistance) as in eq. [4.12]:

$$t_{dead} = \frac{L}{2R} \ln \frac{V_{pulse}}{V_{noise}}. \tag{4.12}$$

The logarithm of the ratio $\frac{V_{pulse}}{V_{noise}}$ can be considered constant (~ 25) for different coils and in a wide range of RF power.

Using eq. [3.5], the 90° and 180° pulses can be defined from eq. [4.13]:

$$\gamma B_1 \tau_{90^\circ} = \frac{\pi}{2}, \qquad \gamma B_1 \tau_{180^\circ} = \pi, \tag{4.13}$$

where the magnetic field created by the RF coil B_1 can be defined through the coil efficiency $\left(\frac{B_1}{i}\right)_{xy}$ and the RF power P_{RF} as in eq. [4.14]:

$$B_1 = \frac{1}{2}\left(\frac{B_1}{i}\right)_{xy}\sqrt{\frac{P_{RF}}{R}}. \tag{4.14}$$

It can be seen from eq. [4.14] that the higher the coil efficiency $\left(\frac{B_1}{i}\right)_{xy}$, the higher B_1 and the shorter the RF pulses for a given flip angle (eq. [3.5]). However, as higher B_1 requires higher V_{pulse}, this results in a longer deadtime of the RF probe (eq. [4.12]).

The RF circuit bandwidth Δf_L is defined by R and L and SNR is maximized when Δf_L is matched to the excitation bandwidth Δf_{exc} as in eq. [4.15]:

$$\left[\Delta f_L = \frac{R}{\pi L}\right] = \left[\Delta f_{exc} = \frac{1}{\tau_{180^\circ}}\right]. \tag{4.15}$$

From here, the coil resistance R_{max} that gives a maximum SNR can be found from eq. [4.16]:

$$R_{max} = \left[\frac{\gamma L}{2}\left(\frac{B_1}{i}\right)_{xy}\right]^{\frac{2}{3}} P_{RF}^{\frac{1}{3}}. \tag{4.16}$$

Considering all the above, a final equation for the SNR of the CPMG pulse sequence can be given as in eq. [4.17]:

$$SNR_{CPMG} = \frac{N_V \gamma^3 \hbar^2 I(I+1)}{6\sqrt{2}(k_B T)^{\frac{3}{2}}}\sqrt{\frac{T_2}{\pi k_d}} \cdot V^* B_0^2 \left(\frac{B_1}{i}\right)_{xy}\left(\frac{\gamma (B_1/i)_{xy}}{2L^2}\right)^{1/3} P_{RF}^{1/6}, \tag{4.17}$$

where the coefficient k_d is defined as in eq. [4.18]:

$$k_d = \frac{9}{4}\left(\ln\frac{V_{pulse}}{V_{noise}} + \pi\right). \qquad [4.18]$$

It is interesting to note that the SNR of the CPMG pulse sequence in the inhomogeneous fields depends on the inductance of the coil L and the applied RF power W_{rf}, which does not happen in homogeneous fields. The RF coil sensitivity is defined as in eq. [4.19]:

$$SNR_{coil} = \frac{(B_1/i)_{xy}^{4/3}}{L^{2/3}} \qquad [4.19]$$

which can be maximized by changing the coil size and number of turns and adding additional resistance to the circuit if needed as long as the total coil resistance does not exceed the specified value of R_{max} (eq. [4.16]).

In the case of signal averaging (number of scans $N > 1$), which is common practice in time domain NMR, the SNR of the signal obtained in N scans is given by eq. [4.20] (Nalcioglu & Cho, 1984):

$$SNR_N(t) \sim \sqrt{N} \cdot SNR_1(t) \qquad [4.20]$$

where $SNR_1(t)$ is the SNR when $N = 1$.

4.2 Aims

There are several steps towards the construction of a setup to measure sodium concentration, relaxation, or both, in biological tissues that need to be accomplished:

- To identify a source of the polarizing magnetic field: it can be a fringe field of a superconducting magnet or a permanent magnet.
- To create an RF circuit containing a coil for the excitation and signal acquisition for the chosen field geometry.
- To assess the excitation volume of the magnet-coil setup.
- To assess the total measurement time and SNR for phantoms with a sodium concentration close to one in biological tissues.
- To measure sodium signals from a sample of biological tissue *in vitro* and then *in vivo* using the constructed setup.

In the scope of this Chapter of the thesis, the following aims were set:

- To use a 9.4 T superconducting magnet with poor shielding as a source of an inhomogeneous polarizing field B_0.
- To construct a wider RF coil than the 24-mm probe that was used before in our laboratory (Unpublished data, 2018).
- To prepare phantoms with descending concentrations of sodium: from saturated to one close to biological tissue (around 140 mM in plasma).
- To measure a sodium signal from the phantoms with the constructed coil in a fringe field of around 0.5 T. 0.5 T field strength was chosen by some practical considerations which were: (1) 0.5 T is a maximum field strength of quadrupole permanent magnet assemblies constructed for our laboratory for sodium measurements in consideration of future work of constructing a portable mobile device based on permanent magnets; (2) 0.5 T is a field strength of a clinical scanner available at the University of Nottingham to have an opportunity to test the constructed sodium RF coils in a homogeneous field.
- To compare the performance of the constructed coils in terms of SNR and scanning time.

4.3 Materials and Methods

Sections 4.3.1-4.3.3 describe the experimental components in the inhomogeneous field of around 0.5 T. Section 4.3.4.2 describes the MR sequences used in experiments and the parameters of the sequences for individual sets of measurements.

4.3.1 Spectrometer

To perform STRAFI experiments, an ultra-high field NMR magnet Oxford (Oxford Instruments, Abingdon, UK) which is a poor-shielded superconducting magnet generating a magnetic field of 9.4 T in its centre (resonance frequency 400 MHz for ^{1}H and 105.86 MHz for ^{23}Na) (Figure 4.4(a)), a portable high-frequency spectrometer Kea^2 (Magritek, Wellington, New Zealand), an external linear pulse power amplifier LPPA 14020 (Dressler) with a maximum 2 kW output (Figure 4.4(b)); a laboratory computer with an operating system Windows 7 with Prospa V3.56 (Magritek) operating the spectrometer were used.

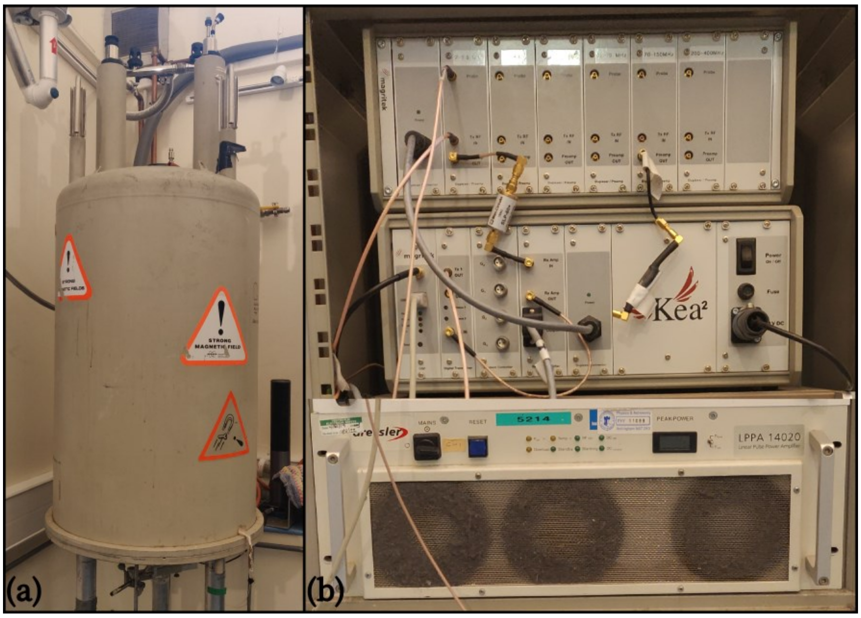

Figure 4.4. (a) The 9.4T poor-shielded NMR magnet Oxford and (b) a portable high-frequency spectrometer Kea^2 with an external amplifier LPPA 14020.

The poor shielding of the Oxford magnet provides a fringe field where a location of the sensitive slice can be found for a nucleus of interest by a choice of the corresponding resonance frequency, according to eq. [2.6]. Alternatively, when the position of a probe can be varied under the magnet, B_0 is changed accordingly, so that one can operate at a fixed frequency.

4.3.2 Probes

For the experiments in the 0.5 T fringe field, a home-built probe was used. According to the eq. [4.19], the contribution of the coil to the total SNR depends on the coil sensitivity B_1/i and the coil inductance L, parameters that can be adjusted during the coil construction process.

The home-built probe contains a saddle coil made from an isolated flat thin copper wire (1.3 mm width, 0.5 mm thickness) wound on a G10 fibreglass tube of the 39.4-mm external diameter (later on named the 40-mm probe) (diagram is shown on Figure 4.5(a)). The coil's length was 22 mm which is 1.8 times smaller than its diameter. A ribbon wire has lower AC resistance than a round wire of the same cross-section when the ratio of width to length is more than 2 (Terman, 1943) which is the case for the used copper wire. The noise induced by the inductor's resistance usually dominates in a lot of NMR experiments, therefore it should be kept low (Mispelter et al., 2015). Thus the coil has only two loops. The coil's capacitance is a less concerning factor as long as the coil's natural resonance is significantly above the desired Larmor frequency (Watzlaw et al., 2013) which was the case for this coil.

The lumped-parameter equivalent circuit of this RF probe is depicted in Figure 4.6 and includes fixed capacitance for both tuning C_t and matching C_m. Due to the coil's relatively small inductance, a large tuning fixed capacitance C_t = 4 nF (comprising of 4 ceramic plate capacitors of 1 nF each, manufacturing discontinued) was added in the series circuit for tuning to reach a frequency of around 5.6 MHz. The matching of the 40-mm coil at 5.6 MHz for ^{23}Na required 6 ceramic plate capacitors of 47 pF each

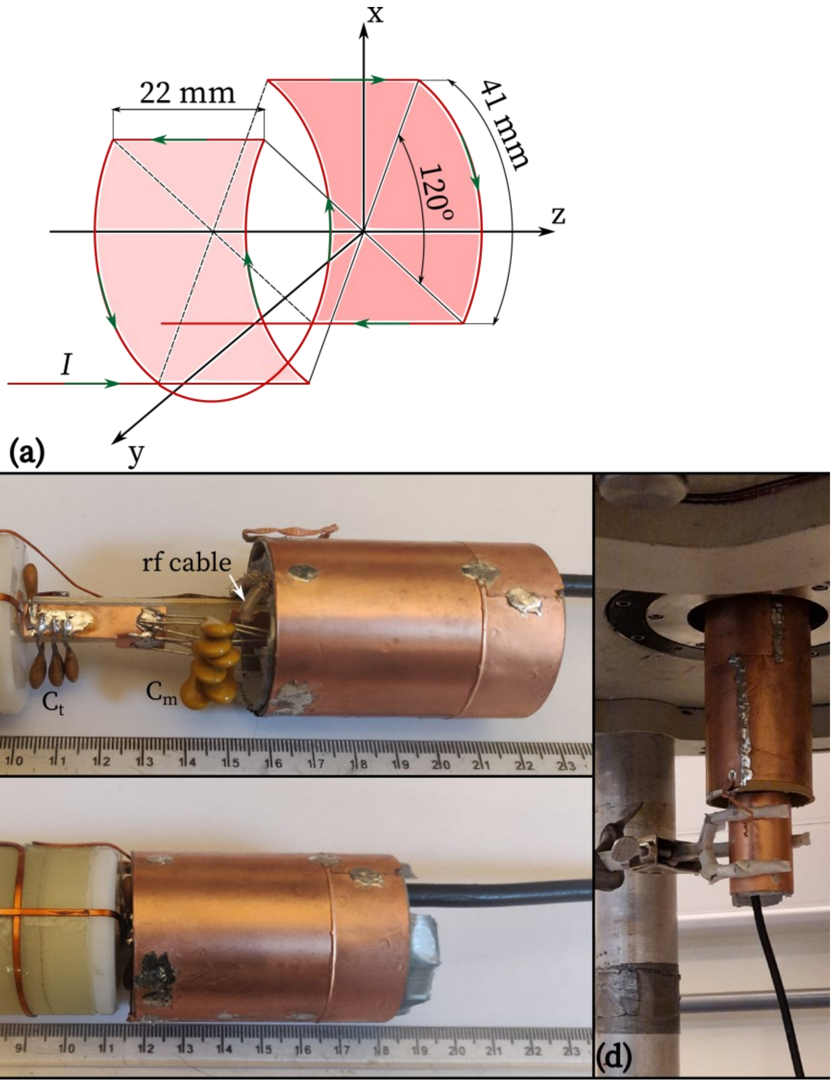

Figure 4.5. (a) A diagram of the home-built 40-mm sodium saddle coil's geometry indicating dimensions and an angle between the windings. A direction of the current *I* is shown by green arrows. (b) The home-made 40-mm sodium probe with the saddle coil used for fringe field experiments. (c) The 40-mm probe with the G10 shield on to cover the capacitors. (d) The sensor is under the magnet covered by the external copper foil shield and hold by a tripod.

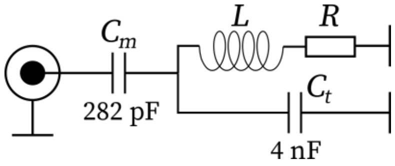

Figure 4.6. Resonant circuit for the 40-mm probe. R and L represent resistance and inductance of the coil correspondingly. C_t and C_m are tuning and matching capacitance respectively. Effective values of the capacitance are indicated (see text).

(overall capacitance C_m = 282 pF, manufacturing discontinued). Because of high C_t, a large variable capacitance is needed in the circuit to perform fine-tuning and fine-matching of the probe in a reasonable range (within 0.5-1 MHz), but it was not available.

The G10 tube of the coil base is mounted on a PTFE holder which holds onto a PTFE rod (10 mm in diameter). The probe also has a shield that covers an area of the tuning and matching capacitors and was grounded to the RF grounding terminal (Figure 4.5(c)). It was made of the same diameter G10 tube which was used for the coil base and was covered with a 40 μm-thick copper foil. A PTFE disk (38 mm in diameter and 6 mm thick) is mounted on the end of the rod to stabilize the G10 shield. A standard flexible 50 Ω coaxial cable (RG58) was used to drive the probe and receive the NMR signal.

The influence of capacitance adjustments on the resonant frequency and the power reflected by the probe were measured with a network analyser (NSA-1000A, 1-1000MHz, AVCOM of Virginia Inc, USA). With the values of C_t and C_m reported above, the minimum of the reflected power was pronounced in a frequency range of 5.35 – 5.75 MHz depending on a phantom, as the probe's tuning and matching changed with the load. The position of the probe under the magnet for every phantom was adjusted accordingly. Q was measured with the 5.17 M table salt phantom and was equal to 68.

The probe was also used with an external shield (Figure 4.5(d)) which was made in our laboratory before the start of my PhD. The shield is a cylinder made of thick cardboard which is covered by one layer of 40 μm-thick copper foil. The shield has an external diameter of 67.4 mm (with the foil) and an internal diameter of 63.6 mm. Edges of the copper foil are soldered together making it enclosed. The upper end of the shield was wrapped in a foam rubber that provides a tight and centred fit of the shield inside the magnet bore. The shield can be grounded to the RF grounding terminal of the probe. This configuration allows one to use the shield with different probes. The shield covers the coil with a sample inside and it slightly overlaps with the G10 shield (Figure 4.5(d)).

After tuning and matching the probe with different phantoms monitored by the network analyser, the probe was then placed under the NMR spectrometer and tested by registering a proton signal at the appropriate magnetic field at 5.5 MHz. After that, the probe's positions were adjusted under the magnet to perform sodium measurements. Results can be sound in Subsection 4.4.3.

The probe was held under the magnet by a tripod with electrically isolated clamps, as depicted in Figure 4.5(d). The probe was also used in both transmit and receive modes.

Volume coils can provide a homogeneous B_1 field along the central axis. NMR in a fringe field has to deal with a magnetic field gradient which is always "turned on". This means that a signal is collected from a slice whose thickness is limited by the gradient (and also limited by the length of an excitation pulse). Finding the position of the slice which corresponds to a certain frequency can be challenging. Therefore, using volume coils that are much longer than the slice thickness is beneficial as they reduce sensitivity to precise positioning.

An RF shield is expected to reduce noise which can interfere with the signal on the same frequency and other frequencies. The effectiveness of the shield depends on the resistivity ρ and magnetic permeability μ of the conductor it was made of and operating frequency ω. In most cases, the depth δ to which radiation can penetrate the shield (the so-called skin depth) can be calculated using the following formula (eq. [4.21]):

$$\delta = \sqrt{\frac{2\rho}{\omega\mu_0\mu_r}}, \qquad [4.21]$$

where μ_0 is the permeability of free space and μ_r is the relative permeability of the conductor. Copper is the most commonly used material for RF shielding. A copper foil with a 40 μm width used in the shield construction can protect from external electromagnetic interference with frequencies in a range of $[2.66, +\infty)$ MHz.

4.3.3 Phantoms

A set of NaCl solutions with different concentrations of sodium were made: 5.17 M, 2.78 M, 0.93 M, 0.5 M, 0.25 M, and 0.125 M. A 5.17 M solution was made using a table salt with an anticaking agent (sodium ferrocyanide). As the amount of sodium ferrocyanide in eatable table salt is less than 20 mg/kg (Soo Lim et al., 2018; Younes et al., 2018), it was considered negligible and not used in the calculations of NaCl molarity. For lower concentrations, NaCl powder of high purity was used (Sigma Aldrich, Gillingham, Dorset, UK). All phantoms were stored in plastic bottles with a 37.6-mm external diameter which had a tight fit inside the coil, thus, the filling factor for the 40-mm probe was maximized.

Agarose is a more electrically neutral polymer than kappa-carrageenan (Piculell & Nilsson, 1989) and it is a major component of agar (about 70%) (Zeece, 2020). Therefore, due to the higher costs of pure agarose, agar was chosen to prepare a tissue equivalent phantom with a high concentration of NaCl, 4.87 M, in 4% agar gel. An agar concentration of 4% means 4 g of agar powder per 100 g of water. Agar powder and NaCl (both Sigma Aldrich) crystals were added to deionized water in a glass beaker while stirring with a magnetic stirrer and heating on a hotplate. Before the heating, the whole beaker with the mixture was weighted on analytical scales. In addition, the beaker was covered with a glass plate to prevent excessive evaporation of water while heating on the hotplate. After the mixture boiled, the heating was reduced and stirring was continued until everything dissolved completely. Later, the whole beaker with the mixture was weighed again and hot water was added to the mixture to compensate for the evaporated water. After short mixing, the solution was transferred to the plastic bottle for the 40-mm probe to cool down and solidify.

In STRAFI experiments, the problem of sample levelling under the magnet can be significantly reduced by using samples long in the z-direction, therefore all samples' heights were much greater than the excitation slice. For both probes described in Subsection 4.3.2, phantoms were longer than the coil by at least 0.5 cm, but all the phantoms in a set had the same height.

4.3.4 Methods

4.3.4.1 Simulation of the magnetic field of the Oxford magnet

For a better understanding of the distribution of the fringe magnetic field of the Oxford magnet under its bore, a simulation was performed using an in-house routine in MATLAB based on the "Biot Savart magnetic Toolbox" for the numerical integration of the Biot-Savart law (Queval, 2022).

The Biot-Savart law can be presented in its integral and differential forms as in eq. [4.22]:

$$\vec{B}(\vec{r}) = \frac{\mu_0}{4\pi}\int_C \frac{I\overrightarrow{dl} \times \overrightarrow{r'}}{\left|\overrightarrow{r'}\right|^3}, \qquad d\vec{B} = \frac{\mu_0}{4\pi}\frac{I\overrightarrow{dl} \times \overrightarrow{r'}}{r'^2}, \tag{4.22}$$

where $\vec{B}(\vec{r})$ is a generated static magnetic field depending only on spatial coordinates, $\overrightarrow{dl}$ is a vector along the path C along which the integral is calculated (Figure 4.7). A magnitude of $\overrightarrow{dl}$ is the length of the differential element of the wire in the direction of a current I. Let's consider a vector $\vec{l}$ end of which points to coordinates (x_P, y_P, z_P) on the path C. Then the vector $\overrightarrow{r'} = \vec{r} - \vec{l}$ is the full displacement vector from the wire element $\overrightarrow{dl}$ at the point $\vec{l}$ to the point $\vec{r}$ at which the field is being computed ($\vec{r} = (x_M, y_M, z_M)$). The magnetic constant μ_0 has its usual meaning.

The cross product $\overrightarrow{dl} \times \overrightarrow{r'}$ can be presented as a determinant of a matrix as in eq. [4.23]:

$$\overrightarrow{dl} \times \overrightarrow{r'} = \begin{vmatrix} e_1 & e_2 & e_3 \\ dx_P & dy_P & dz_P \\ x' & y' & z' \end{vmatrix}, \tag{4.23}$$

where e_1, e_2 and e_3 are unit vectors along x, y and z axes correspondingly. The determinant is revealed in eq. [4.24]:

$$\begin{aligned}\overrightarrow{dl} \times \overrightarrow{r'} = e_1(dy_P \cdot z' - dz_P \cdot y') + e_2(dz_P \cdot x' - dx_P \cdot z') \\ + e_3(dx_P \cdot y' - dy_P \cdot x').\end{aligned} \tag{4.24}$$

Then $d\vec{B}$ from eq. [4.22] can be presented as $\nabla\vec{B}$ which has a definition as in eq. [4.25]:

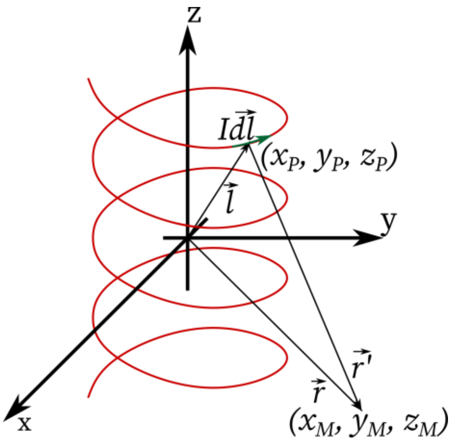

Figure 4.7. Schematic representation of the solenoid (path C shown in red) in a coordinate system for the numerical calculation of the Biot-Savart law.

$$\nabla\vec{B} = \frac{\partial B}{\partial x}e_1 + \frac{\partial B}{\partial y}e_2 + \frac{\partial B}{\partial z}e_3 = \begin{pmatrix} \frac{\partial B}{\partial x} \\ \frac{\partial B}{\partial y} \\ \frac{\partial B}{\partial z} \end{pmatrix}. \qquad [4.25]$$

Finally, using eq. [4.22], [4.24] and [4.25], the following differential equations can be obtained (eq. [4.26]):

$$\frac{\partial B}{\partial x} = \frac{\mu_0 I}{4\pi} \cdot \frac{dy_P \cdot z' - dz_P \cdot y'}{\left|\vec{r'}\right|^3} = dB_x,$$
$$\frac{\partial B}{\partial y} = \frac{\mu_0 I}{4\pi} \cdot \frac{dz_P \cdot x' - dx_P \cdot z'}{\left|\vec{r'}\right|^3} = dB_y, \qquad [4.26]$$
$$\frac{\partial B}{\partial z} = \frac{\mu_0 I}{4\pi} \cdot \frac{dx_P \cdot y' - dy_P \cdot x'}{\left|\vec{r'}\right|^3} = dB_z.$$

As $\vec{r'} = \vec{r} - \vec{l}$, $\left|\vec{r'}\right|^3$ can be represented as in eq. [4.27]:

$$\left|\vec{r'}\right|^3 = \left(\sqrt{(x_M - x_P)^2 + (y_M - y_P)^2 + (z_M - z_P)^2}\right)^3. \qquad [4.27]$$

When the equations [4.26] need to be solved numerically, the following substitutions are made: $dx_P = x_P^{k+1} - x_P^k$, $dy_P = y_P^{k+1} - y_P^k$ and $dz_P = z_P^{k+1} - z_P^k$, where k is a discretization index. Similarly, $x' = x_M - x_P^k$, $y' = y_M - y_P^k$, $z' = z_M - z_P^k$ and

$|\vec{r'}|^3 = \left(\sqrt{\left(x_M - x_P^k\right)^2 + \left(y_M - y_P^k\right)^2 + \left(z_M - z_P^k\right)^2}\right)^3$. Then the integral for $\vec{B}(\vec{r})$ will be just a sum of all separate field components dB_x, dB_y and dB_z.

4.3.4.2 Magnetic field measurements of Oxford magnet

The magnetic field of the Oxford magnet needed to be measured to provide the positioning of the probes under it as accurately as possible according to their resonance frequency. The magnetic field was measured along the central axis of the magnet (z-direction) with a gaussmeter (model 6010, F.W. Bell®, Portland, Oregon, USA) with an axial probe. Also, at a distance from the bottom of the magnet bore where the field equals 0.5 T, the magnetic field was measured in a horizontal (xy) plane with two gaussmeters: with the axial probe as used before and with a transverse probe (model GM07, Hirst Magnetic Instruments Ltd., Falmouth, UK). The measurements are also important to determine values of the magnetic field gradient in z and xy directions: G_0 and G_{xy} correspondingly. The gradient G_0 determines the thickness of the excited slice Δz according to eq. [4.1]. Excitation bandwidth Δf is inversely proportional to the pulse length, therefore, shorter pulses can excite a thicker slice. However, the minimum width of the 90° pulse is limited by the coil size and its efficiency.

The gradient G_{xy} determines the size of the area that the coil can collect the signal from: G_{xy} introduces a frequency offset which determines the line width of the spectrum. How wide the line width can be detected depends on the acquisition parameters.

4.3.4.3 Flip angle calibration

A flip angle calibration in the fringe field was performed by a pulse sequence "CPMGAdd" (Figure 4.8): it is a typical CPMG pulse sequence which produces a train of RF pulses. Unlike the Bruker spectrometer used in Chapter 3 , the pulses (one 90° and n 180° pulses) produced by Kea^2 have the same length but different amplitudes (the amplitude of the 180° pulse is 6 dB higher than that of the 90° pulse), and the acquisition happens after each 180° pulse, hence a whole train of echoes is produced in one scan. Specifically for "CPMGAdd", to increase SNR, the echoes are summed together in the time domain and then the result of summation is Fourier transformed.

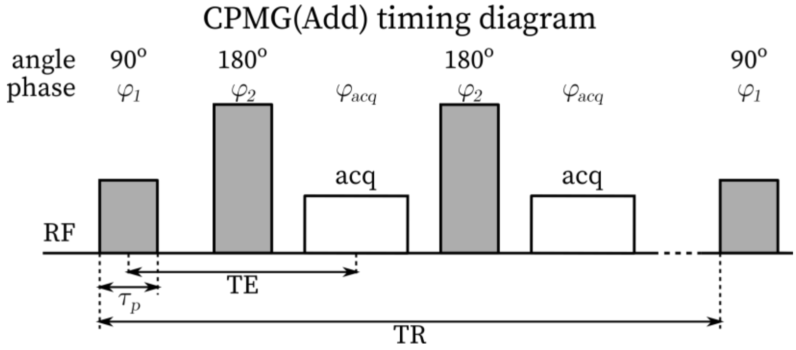

Figure 4.8. CPMG and "CPMGAdd" pulse sequence timing diagram. Only two echoes are shown. In CPMGAdd all echoes are summed up to increase SNR.

To determine an optimal 90° pulse, lengths or amplitudes of the pulses can be varied. If the pulses are not optimized, non-effective excitation happens along with inefficient refocusing which leads to a signal decrease. The maximum signal will be observed only when both optimal excitation and refocusing are implemented.

The constructed probe was undergoing a pulse calibration for both nuclei: ^{1}H and ^{23}Na. Parameters of the pulse calibrations are indicated in Table 4.1 along with the used phantoms for proton and sodium measurements. Pulse calibration was performed by repeating the "CPMGAdd" pulse sequence (Figure 4.8) with a changing pulse length. A time domain (TD) sine-bell squared filter was applied to the sum of echoes before the Fourier transformation unless stated otherwise.

The sine-bell squared filter is represented by the equation [4.28]:

$$filter_{sine-bell\,squared}(t) = \left\{\cos\left(\frac{\pi}{2}\frac{x-p_1}{N-p_1}\right)\right\}^2 \qquad [4.28]$$

where the parameter $p_1 = N/2$ and N is a number of complex points. An obtained spectrum after FT without zero-filling was extracted from Prospa and then phased and integrated in MATLAB. As a result, the integral values are plotted vs the pulse length. The pulse sequence parameters were adapted to the relaxation times of the used phantoms. The total scanning time for each value of pulse length T_{total} can be calculated as follows: $T_{total} = TR \times (number\ of\ scans)$. Results are found in Subsection 4.4.3.

The coil with a larger diameter requires a longer pulse for the same flip angle θ. To avoid the overheating of the spectrometer amplifier, Prospa has a limitation for a duty cycle inside the pulse sequence: the length of the 90° pulse can be no more than 20%

Table 4.1. Parameters of the “CPMGAdd” pulse sequence for pulse optimization for proton and sodium measurements.

Nucleus	Phantom	TE, μs	Echoes	SW, kHz	TR, ms	Scans
^{1}H	5.17 M table salt	260	64	500	10000	16
^{23}Na	5.17 M table salt	300	64	500	500	512

of TE. Therefore, with increasing the pulse length, TE should be lengthened as well. Consequently, signal loss can be observed which may lead to a decrease in SNR.

After the pulse calibration, measurements of sodium signal were performed using the “CPMGAdd” sequence with the found optimal 90° pulse (and consequently 180° pulse) for a range of phantoms to assess the time required to achieve an appropriate SNR for each concentration of sodium. All experiments were conducted at room temperature (20°C).

4.3.4.4 Calibration of the probe by ^{1}H measurements

The aim of proton measurements with the constructed probe was to demonstrate the performance of the probe with the nucleus of highest sensitivity (^{1}H) before moving towards experiments with sodium which has much lower sensitivity (Subsection 2.1.2).

Results of the proton pulse calibration for the 40-mm probe are shown in Figure 4.9 using a water solution of 5.17 M table salt as a sample. On the graph, an integral of the proton signal is plotted vs the pulse length. 16 scans were averaged to obtain each point of the plot without a TD filter, TR = 10 s which was found sufficiently long for a water solution of NaCl without any paramagnetic agent (see Table 4.1). The whole experiment took 1 h 7 min. The optimum pulse length was found to be 18 μs (Figure 4.9(a)). ^{1}H echo sum and its Fourier transform obtained with the optimum pulse are shown in Figure 4.9(b). SNR = 106 of the spectrum was obtained in 16 scans in 2 min 40 s without the TD filter as well. SNRs were calculated by the following formula (eq. [4.29]) (Wetterling et al., 2012):

$$SNR = \frac{S - \bar{N}}{\sigma(N)} \qquad [4.29]$$

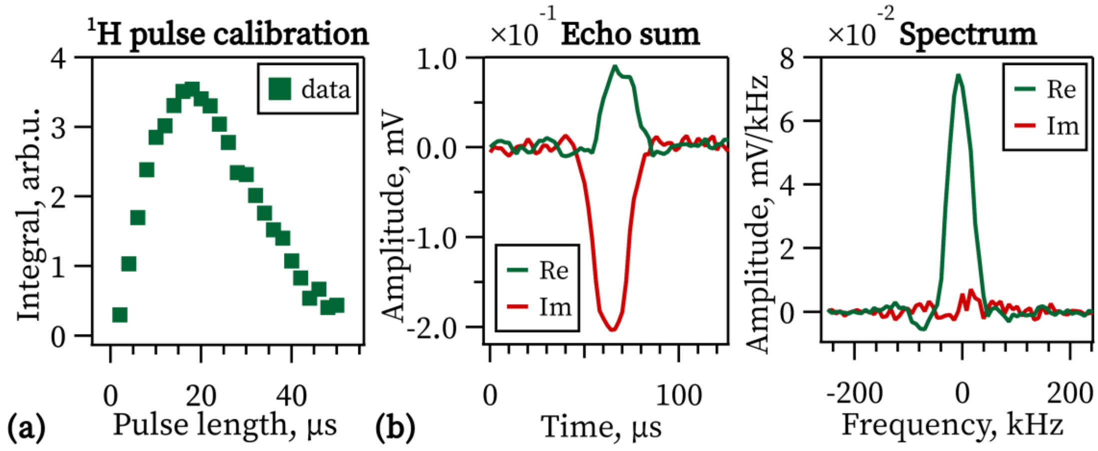

Figure 4.9. (a) ^{1}H pulse calibration for the 40-mm probe. An optimum 90° pulse length is 18 µs. (b) ^{1}H FID and spectrum obtained by CPMGAdd with the pulse length = 18 µs. 16 scans, without the TD filter, spectrum SNR = 106.

where S is the maximum spectral intensity of the signal, $\bar{N}$ is a mean signal outside the area of the signal peak representing noise, and $\sigma(N)$ is a corresponding standard deviation of the noise mean. Noise areas were manually determined for each experiment presented in this thesis.

Experiments were performed at 5.49 MHz. As the probe's tuning can't be adjusted, the probe itself was positioned at 0.129 T respectively. This means that the value of the field gradient G_0 was 0.58 ± 0.15 T/m. As CPMG RF pulses' length of 18 µs excite a range of frequencies of about 28 kHz (eq. [4.10]), which under the 0.58 ± 0.15 T/m field gradient generated at the probe's position corresponds to 1.1 ± 0.6 mm slice thickness.

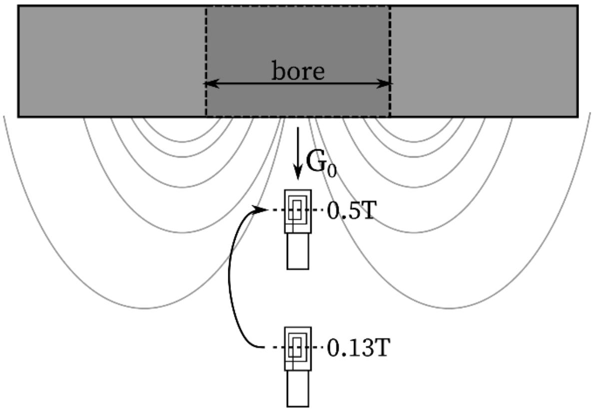

Figure 4.10. Probes' position in the fringe field of the Oxford magnet. Firstly, the probes were positioned at ≈ 0.13 T for ^{1}H measurements and then moved higher in field (≈ 0.5 T) for ^{23}Na measurements (indicated by the arrow). Light grey lines represent magnetic field lines. Only bottom part of the Oxford magnet is shown.

After calibration with ^{1}H measurements, the probe was moved to the higher magnetic field of the Oxford magnet to perform sodium signal acquisitions with approximately the same resonance frequencies as were used with ^{1}H measurements (Figure 4.10).

4.3.4.5 Sequence parameters for ^{23}Na measurements

After the 40-mm probe was calibrated by performing proton measurements (Subsection 4.3.4.4) and optimal 90° and 180° pulses that give maximum sodium signal for phantoms were found (Subsection 4.3.4.3), the CPMGAdd pulse sequence was used to acquire sodium signal from all the phantoms with different concentrations of NaCl. The measurements were performed with the following parameters: the length of the 90° pulse was PL = 60 μs, its amplitude PA = -17 dB; the amplitude of the 180° pulse is 6 dB higher than the 90° PA. For all phantoms, TE = 300 μs, 64 echoes were collected with SWH = 500 kHz. Other parameters as TR and number of scans were varied for different samples and their values are shown in Table 4.2. TR was varied depending on a scanning time available in the laboratory: for some samples (2.78 and 0.25 M), TR was shortened to reduce scanning time during the day. However, a full recovery of magnetization was expected for both samples as sodium T_1 in water solutions is shorter than 60 ms (Mitchell, 2016). The number of scans was increased to compensate for SNR reduction due to decrease in sodium concentration.

Table 4.2. TR and number of scans for the "CPMGAdd" pulse sequence for sodium measurements for phantoms with different concentrations of NaCl using the home-built 40-mm probe. Other sequence parameters are indicated in text.

Phantom	TR, ms	Scans
5.17 M table salt	500	3600
2.78 M NaCl	200	3600
0.93 M NaCl	500	7200
0.5 M NaCl	500	25600
0.25 M NaCl	300	25600
0.125 M NaCl	1000	32768

4.3.4.6 Measurement of a relaxation time

In the fringe field, the spin-spin relaxation time T_2 was measured using a standard CPMG sequence without the echo summation. The echo train was Fourier transformed without zero-filling, phased, and integrated using a homemade routine in MATLAB. For the NaCl solutions, the integral values were fitted vs TE using the Levenberg-Marquardt algorithm in Igor.Pro by an eq. [4.30]:

$$I_{mono}(t) = I_o exp\left(-\frac{t}{T_2}\right) \qquad [4.30]$$

with fitting parameters I_0 and T_2. For the agar sample, the integrals were fitted with an equation [3.8] for a biexponential relaxation.

Parameters of CPMG pulse sequence to determine T_2 of sodium are presented in Table 4.3. T_2 measurements were performed only for the phantom with the highest concentration of NaCl (5.17 M) of the aqueous solution and in the 4.87 M 4 % agar gel since lower sodium concentrations lead to dramatic increase in measurement time due to very low SNR.

Table 4.3. CPMG parameters to determine sodium T_2 in different samples using the 40-mm probe.

Phantom	TE, µs	Echoes	SW, kHz	TR, ms	Scans
5.17 M table salt solution	300	256	500	700	7200
4.87 M NaCl + 4% agar	300	128	500	3000	12800

4.3.4.7 Comparison of two coils with a different diameter

In addition to the 40-mm coil mainly used for the sodium measurements, the 24-mm probe (Unpublished data, 2018) was used for purposes of comparison. To compare SNRs between the probes, several conditions should be kept the same. The same pulse length found for the 40-mm probe was used with the 24-mm probe, and the power level was calibrated for it. The 24-mm probe was also used with the external shield to provide the same noise level. Other acquisition parameters like TE, number of echoes, dwell time (DW), number of complex points, RG and TR were kept the same as for the 40-mm probe. The experiments were performed using the same sample: the water solution of 5.17 M table salt.

4.4 Results

This section presents the results of simulations of the distribution of the magnetic field of the Oxford magnet (Subsection 4.4.1), actual measurements of the magnetic field using two gaussmeters (Subsection 4.4.2) and results of sodium measurements in the fringe field of 0.5 T (Subsection 4.4.3) with the 40-mm home-built probe.

4.4.1 Simulation of the magnetic field of the Oxford magnet

For the magnetic field simulation, the Oxford magnet was represented as a solenoid with a radius of 0.05 m and 0.8 m in length made of one layer of infinitely thin wires. The above dimensions approximate the size of the magnet bore. To simulate the superconductivity, the number of turns in the solenoid and the current strength were set in such a way that the field in the centre of the solenoid ($x = y = z = 0$) was approximately equal to 9.4 T. The calculated magnitude of the magnetic field $|\vec{B}_0| = \sqrt{B_x^2 + B_y^2 + B_z^2}$ is shown in Figure 4.11 in a xz plane ($\vec{B}_0$ is parallel to the z axis). The colour scale was set up in a way that the field value of 0.5 T is highlighted in red. Due to axial symmetry, the field pattern is the same in yz plane. This means that the 0.5 T field surface has a "bowl" shape. It can be seen that the lines of the equipotential

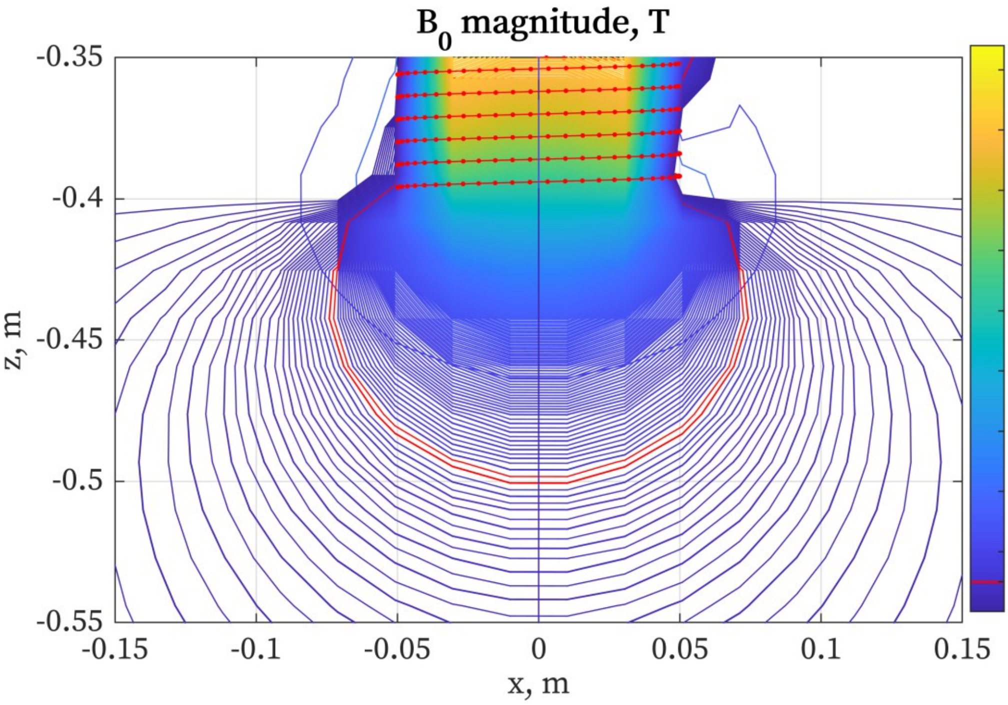

Figure 4.11. The simulated magnitude of the magnetic field $|\vec{B}_0|$ of the Oxford magnet, xz plane. A field line of 0.5 T is highlighted in red.

are normal to the z-axis and are convex. A most straightforward way to position a volume coil under the magnet is where a normal to this surface is parallel to the central axis of the magnet, i.e., at $x = y = 0$ and $z = z_{min}$ at $|\vec{B}_0| = 0.5$ T (Figure 4.11).

4.4.2 Magnetic field measurements at a level of 0.5 T

The magnetic field of the Oxford magnet was measured along the central axis of the magnet bore (z direction) to determine the distance at which the magnetic field of 0.5 T is located. The z component, B_z, of the magnetic field $\vec{B}_0$ is plotted as a function of the distance from the bottom of the magnet in Figure 4.12. A field line of 0.5 T is located approximately at 81 mm. In the region between 70 and 95 mm, the magnetic field has a gradient G_0 equal to 4.1 ± 0.2 T/m.

To determine a curvature of the magnetic field profile at 0.5 T, B_z was measured in xy plane with two gaussmeters. A measured area was a circle with a diameter of 60 mm, and its centre was positioned on the central axis of the magnet bore. The magnetic field was measured with a spatial resolution of 2.5 mm. Variations of B_z in the measured area are shown in Figure 4.13(a). Deviation of the field isolines (lines with the constant value of the magnetic field) from the circular shape and the presence of some "spikes" are related to the instrumental and measurement errors of the gaussmeters. The magnetic field map was recalculated into a frequency offset map for

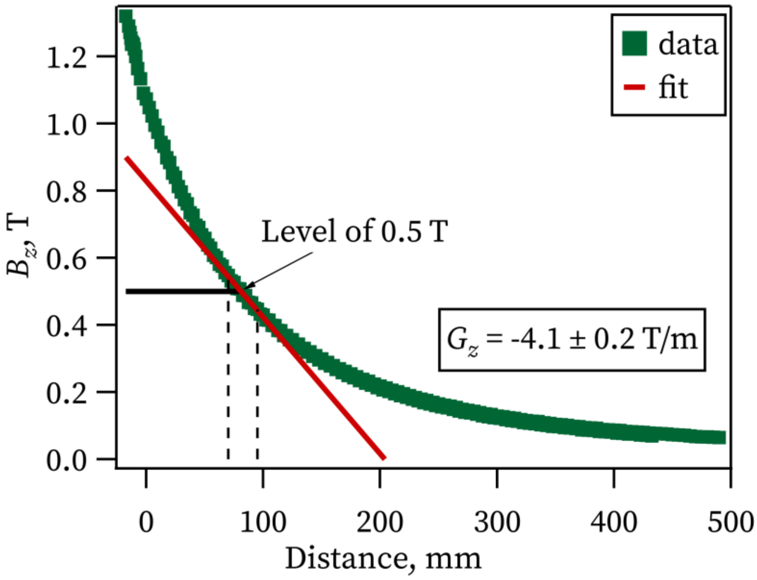

Figure 4.12. Dependence of the field B_z along the z direction. The field has a gradient G_0 of 4.1 ± 0.2 T/m between 70 and 95 mm from the bottom of the magnet bore. Negative distance means that the gaussmeter probe was inserted inside the bore.

sodium-23 and it is shown in Figure 4.13(b). The frequency offset map is normalized to a frequency of sodium at 0.5 T, 5.63 MHz, and red lines mark frequency increments of 20 kHz.

If positioned on the central axis of the magnet, the 40-mm probe would cover up to 80 kHz, whereas the 24-mm probe used for initial measurements (Unpublished data,

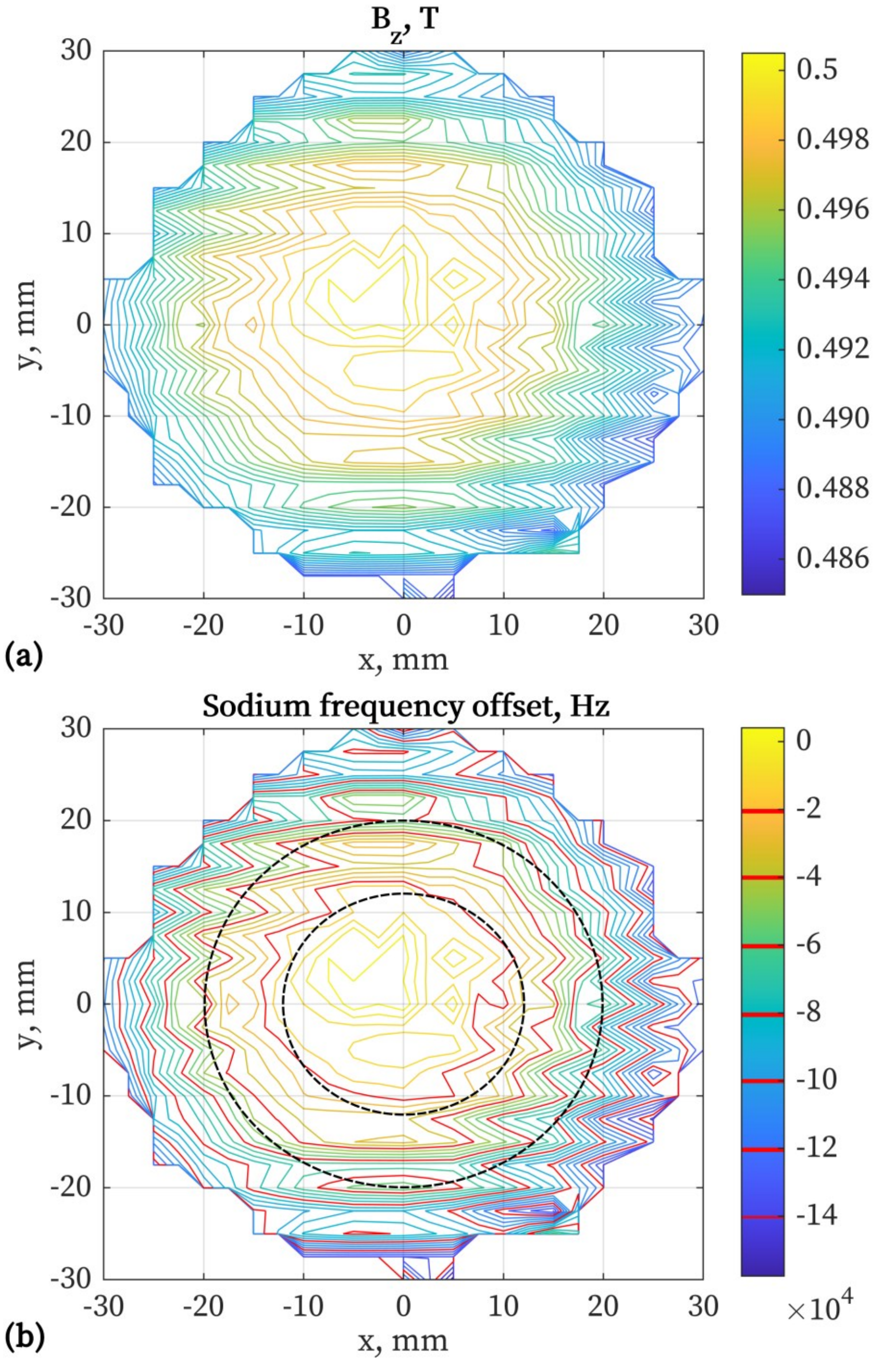

Figure 4.13. (a) A contour plot of B_z measured with two gaussmeters with a resolution of 2.5 mm. (b) Sodium frequency offset map normalized to the sodium frequency at 0.5 T (5.63 MHz). Red lines highlight frequency increments of 20 kHz. Two black dashed circles represent cross sections of the 40-mm and 24-mm probes.

2018) would cover 20 kHz of the frequency offset (Figure 4.13(b), two dashed circles). These frequency offsets will add additional broadening to the line width of the sodium spectrum.

4.4.3 Measurements of sodium signal in solutions of different concentrations of NaCl

This subsection describes experimental results obtained with the 40-mm homemade probe. The main aim of building the probe with a wider diameter was to perform measurements of the sodium signal in a fringe field with decreasing concentrations of NaCl in aqueous solutions and to compare experimental times and SNRs with measurements made with the 24-mm probe (Unpublished data, 2018). But before that, the probe was tested for signal acquisition from the most sensitive nucleus, ^{1}H, using the aqueous solution of 5.17 M NaCl as a sample (this was described in Subsection 4.3.4.4). SNRs and experimental times for ^{23}Na signal acquisitions performed by the 40-mm probe are given later in the current section.

Results of the pulse calibration for sodium, namely a signal integral plotted vs the pulse amplitude, performed with the 40-mm probe are shown in Figure 4.14(a) using a water solution of 5.17 M table salt as a sample. To provide the same flip angle ($\theta = \pi/2$) for sodium for the same B_1, a pulse length should be $\approx \gamma_{1H}/\gamma_{23Na} = 3.78$ times longer than one for protons (eq. [3.5]). Therefore, a pulse calibration for sodium was

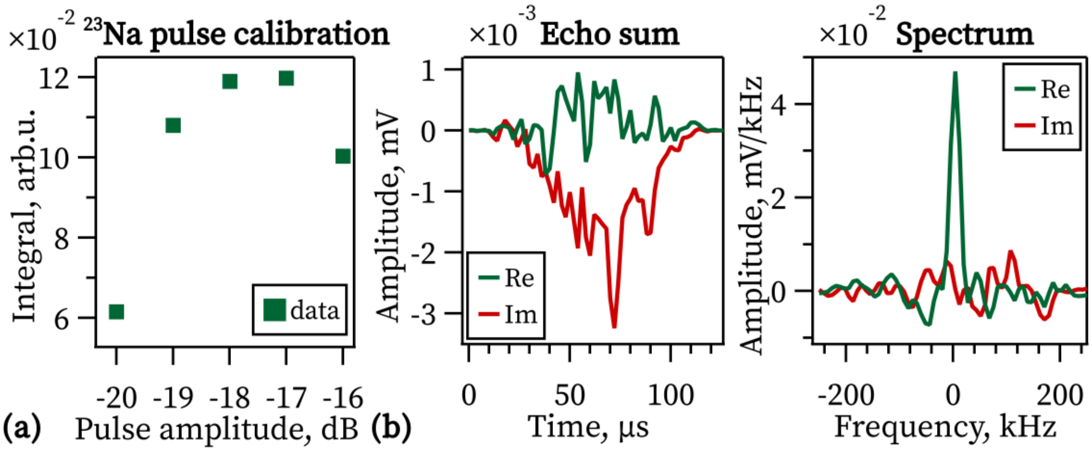

Figure 4.14. (a) ^{23}Na pulse calibration performed using the 40-mm probe and the aqueous solution of 5.17 M table salt as a sample. For a 60 µs duration, an amplitude of the 90° pulse that gives a maximum signal is -17 dB. Consequently, 180° pulse amplitude is -11 dB. (b) ^{23}Na FID and spectrum obtained by CPMGAdd with the optimal pulse amplitude. With the TD filter, 512 scans, SNR = 22.

performed with PL = 60 μs and the pulse amplitude was varied. A found 90° pulse amplitude that give a maximum signal was -17 dB. The amplitude of the 180° pulse was -11 dB correspondingly. ^{23}Na echo sum and its Fourier transform obtained with the optimum pulse are shown in Figure 4.14(b). A spectrum SNR = 22 was obtained in 512 scans after the application of the sine-bell squared filter in the time domain. With the 60 μs excitation pulse, 4.02 ± 0.19 T/m field gradient at the probe's position in 0.485 T, the thickness of the excitation slice is calculated to be 184 ± 18 μm.

After the pulse calibration, sodium measurements with the "CPMGAdd" protocol were performed for each phantom (see Subsection 4.3.3): 5.17 M table salt, 2.78 M, 0.93 M, 0.5 M, 0.25 M and 0.125 M NaCl. Pulse calibration was performed in advance only for the aqueous solution of 5.17 M table salt due to low sensitivity of sodium nuclei in lower concentrations, especially in inhomogeneous fields. Tuning and matching of the probe depended on the sodium concentration, thus the probe's position under the magnet was adjusted to match the resonance frequency. Sodium spectra obtained from the 3 most concentrated samples, the 5.17 M table salt, 2.78 M, and 0.97 M NaCl phantoms, were evaluated quantitatively (Subsection 4.5.3).

Results of the sodium measurements performed with the "CPMGAdd" protocol for all 6 calibration phantoms: water solutions of 5.17 M table salt, 2.78 M, 0.93 M, 0.5 M, 0.25 M, and 0.125 M NaCl, are shown in Figure 4.15. The sine-bell squared filter was applied in the time domain. As the probe's load changes with the salt concentration and there are no trimming capacitors in the circuit of the 40-mm probe due to high fixed capacitance, the position of the probe under the magnet was adjusted accordingly to provide a resonance of sodium nuclei. The magnetic field corresponding to the resonance frequency of the probe with the phantom was measured by the gaussmeter with an axial probe. All experiments were performed in a range of 5.38 – 5.56 MHz (0.477 – 0.494 T). For this difference in positioning in the magnetic field, the slice thickness for PL = 60 μs changes from 184 ± 18 μm to 177 ± 16 μm. The ratio of these thicknesses is 0.96 ± 0.14 which makes the difference in the slice thickness negligible. The number of scans, the experimental time and an achieved SNR are indicated in the legend of Figure 4.15 for each sample. It can be seen that with the sodium concentration going down, the influence of noise is increasing dramatically. Therefore, the measurement time was increased with the decrease in the sodium concentration. For concentration below 0.25 M, echo shapes become distorted due to the big influence of noise. For sodium concentrations below 0.93 M, it can be seen that the measurement time is more than an hour; especially for the 0.125 M phantom it reaches 9 hours which seems impractically long. However, when there was an opportunity to run experiments overnight with long TR to minimize the heating of the spectrometer and the sample, it was used. Nevertheless, an SNR of only 7.7 was achieved for the 0.125 M NaCl phantom, even after more than 32 thousand scans.

The "CPMGAdd" experiment was also performed on a sample of 4.87 M NaCl 4% agar gel as a tissue equivalent phantom. The experiment was performed with most of

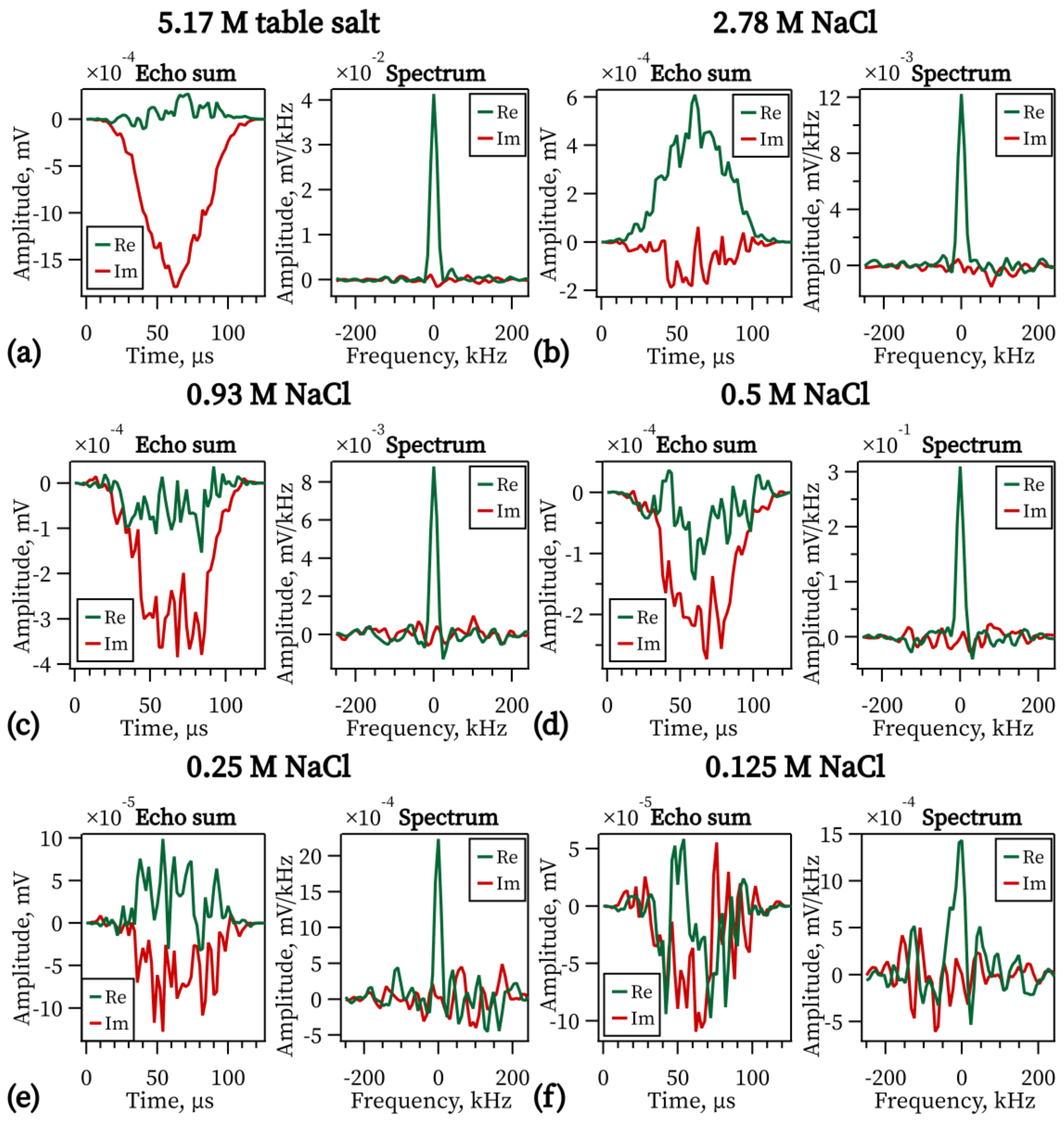

Figure 4.15. Sodium measurements with the 40-mm probe. (a) 5.17 M table salt. t_{acq} = 30 min, SNR = 74.7. (b) 2.78 M NaCl. t_{acq} = 12 min, SNR = 43.7. (c) 0.93 M NaCl. t_{acq} = 1 h, SNR = 33.9. (d) 0.5 M NaCl. t_{acq} = 3 h 33 min, SNR = 35.8. (e) 0.25 M NaCl. t_{acq} = 2 h 8 min, SNR = 11.8. (f) 0.125 M NaCl. t_{acq} = 9 h 6 min, SNR = 7.7.

the parameters being the same as for the 5.17 M table salt, except repetition time (TR), resonance frequency and hence the position under the magnet, and the number of collected echoes. As the sodium relaxation time T_2 in the agar gel was expected to be shorter than one in a water solution, it was experimentally confirmed that reduction of TR from 500 ms to 200 ms and number of echoes from 64 to 16 does not have a negative effect on SNR but even increases it. To keep the coil's best matching with the agar sample as with the water solution sample, the tuning needed to be changed: the coil with the agar sample needed to be positioned in a slightly higher magnetic field (0.487 T) compared to the sensor's position with the water solution (0.478 T). However, as calculated earlier for the field range of 0.477 – 0.494 T, the difference in the slice thickness is negligible. The same holds for the range 0.478 – 0.487 T. Results of the signal collection from sodium in the agar gel are shown in Figure 4.16. However, for the same number of scans and TE, the SNR of the sodium signal from the agar sample is 2.6 times smaller than for the 5.17 M table salt solution. Partially this difference in the signal intensity comes from the difference in the sodium concentration.

Measurements of the relaxation time T_2 were performed only for the highest concentration of sodium chloride, 5.17 M and 4.87 M for liquid and gel samples correspondingly, as phantoms with lower concentrations were having extremely long times of measurement (more than 5 hours). The fits of the CPMG echo trains for the 5.17 M table salt and the agar gel with 4.87 M NaCl are shown in Figure 4.17. For the water solution, the data were fitted by the equation [4.30] for a mono-exponential

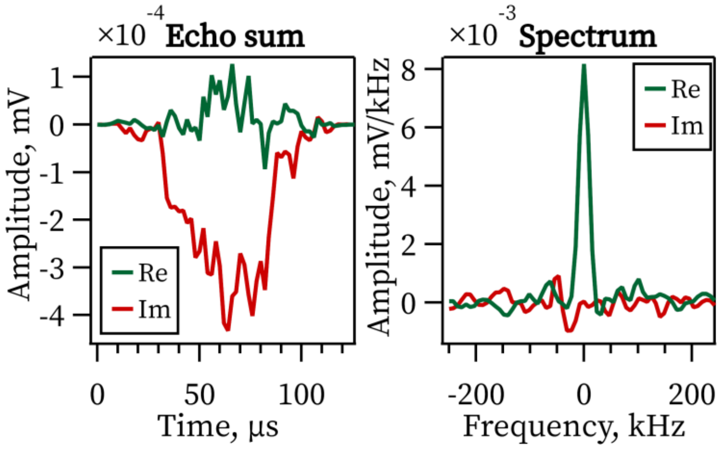

Figure 4.16. Sodium measurements with the 40-mm probe in the 4% agar sample with 4.87 M NaCl. 3600 scans, t_{acq} = 12 min, spectrum SNR = 31.6.

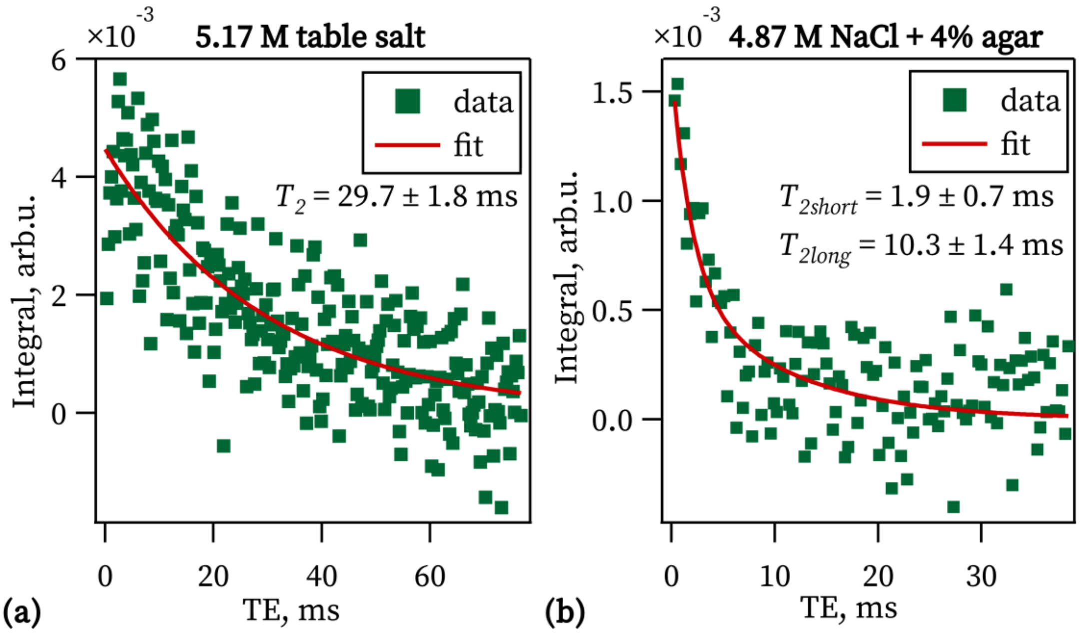

Figure 4.17. Integrals of echoes' spectra vs echo time for (a) the water solution of 5.17 M table salt and (b) the 4% agar gel with 4.87 M NaCl.

relaxation. For the agar sample, equation [3.6] of the bi-exponential decay was used to fit the data. The long component of T_2 of the agar gel, T_{2long} = 10.3 ± 1.4 ms, is almost 3 times shorter than the T_2 of the saltwater solution (29.7 ± 1.8 ms). For the same time interval defined as TE multiplied by the number of acquired echoes (256 echoes in the case of the saltwater solution), less sodium signal and more noise are collected from the agar gel due to its short sodium T_{2long}. Short relaxation times of sodium in the agar gel led to SNR decrease in the experiments depicted in Figure 4.16 even with the reduced length of the echo train.

4.4.3.1 Comparison of two coils with a different diameter

To investigate whether the benefit of increasing the coil diameter takes place, sodium signal measurements were performed by both 24-mm (Unpublished data, 2018) and 40-mm probes with the same experimental conditions: the optimal 90° pulse should be found for the 24-mm probe with acquisition parameters used for the 40-mm probe. The pulse length = 60 μs was used, and an amplitude was found for the 24-mm probe. The aqueous solution of 5.17 M table salt was used as a sample for both probes. An example of the pulse calibration for the 24-mm probe is shown in Figure 4.18(a): a signal integral is plotted vs pulse amplitude in dB. Figure 4.18(b) shows the echo sum and its spectrum obtained with the optimal pulse amplitude, -26 dB.

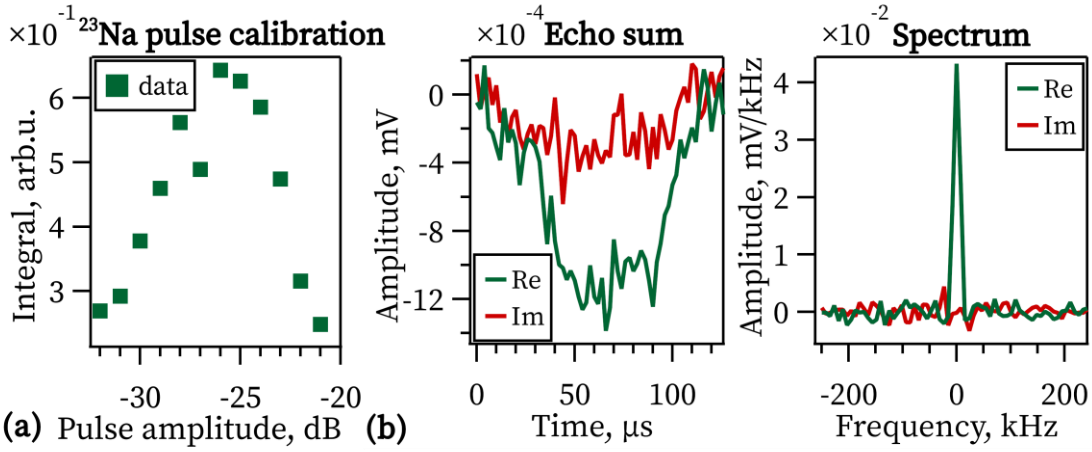

Figure 4.18. (a) Calibration of a pulse amplitude for the pulse length of 60 µs for the 24-mm probe using 5.17 M table saltwater solution as a phantom. The optimum is at -26 dB. (b) ^{23}Na FID and spectrum obtained by "CPMGAdd" with the pulse length = 60 µs and the pulse amplitude = -26 dB. Without TD filter, 512 scans, spectrum SNR = 40.

Due to the limited capabilities of the probes to tune and match to the same frequency, the probes were positioned at the field where they had tuning and matching as best as possible: 0.509 T for the 24-mm probe (f_0 = 5.73 MHz) and 0.478 T for the 40-mm probe (f_0 = 5.4 MHz). This was done to maximize the effectiveness of transmitted power by sacrificing keeping the slice thickness the same. However, it is not difficult to consider the effect of positioning.

Then one "CPMGAdd" experiment for each of the coils was performed with the same parameters (TE = 300 µs, 64 echoes summed up, 3600 scans averaged, TR = 500 ms, t_{acq} = 128 µs, RG = 43) and the same samples – the water solution of the 5.17 M table salt (Figure 4.19). Integrals of the sodium signal in a region of [-30, 30] kHz and SNRs were calculated. Results are presented in Table 4.4.

It can be seen from Table 4.4 that an increase in integral signal was achieved with the 40-mm but SNR was reduced. Several factors can contribute towards the increase in sodium signal. With increasing coil diameter, a higher number of spins is contained within a thin cylinder with a bigger diameter. Additionally, the position of the 40-mm probe was in a slightly lower gradient (G_0 = 4.0 ± 0.12 T/m) compared to the 24-mm probe (G_0 = 4.3 ± 0.2 T/m). However, the ratio of slice thicknesses is equal to 1.07 ± 0.12. Therefore, the effect of the slice thickness on the signal increase can be considered negligible. Considering the same spin densities, despite a 6 times increase in the area of the excitation slice, the total signal increase was only 1.4 times. As the

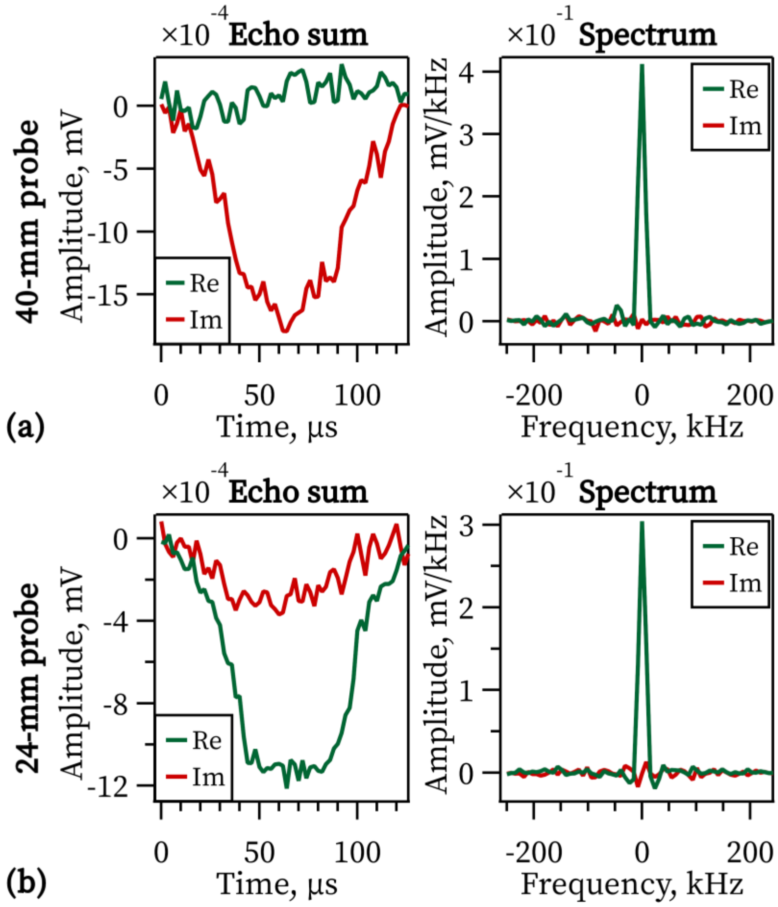

Figure 4.19. Sodium signal obtained from the 5.17 M table saltwater solution by (a) the 40-mm probe and (b) the 24-mm probe. 3600 scans, t_{acq} = 30 min, without TD filter.

signal depends linearly on the excitation volume (eq. [4.9]), the difference in the probes' sensitivity defined by eq. [4.19] could be a major factor in the insufficient signal increase. This might be also contributing to the decreased SNR of the 40-mm probe compared to the 24-mm probe.

Table 4.4. Integral and SNR values calculated from the spectra of the 5.17 M table salt obtained by the 20- and 40-mm probes.

Probe	Integral of [-30, 30] kHz	SNR
24-mm	4.4 arb.u.	146.2
40-mm	6.17 arb.u.	97.8

4.5 Discussion

This Subsection describes the main findings from the experiments described in this Chapter. The measurements of the signal of sodium nuclei in liquid samples in an inhomogeneous field of a superconducting magnet are reported for the first time to the best of the Author's knowledge. A probe based on a saddle coil with a diameter of 40 mm was constructed in-house to perform sodium measurements in the inhomogeneous field from phantoms with different concentrations of sodium chloride (NaCl): from 5.17 M water solution down to concentrations of 125 mM close to ones in biological tissues. Moreover, the performance of the two probes (the 40-mm one and an additional 24-mm probe) was compared under the same experimental conditions. The feasibility of detecting the sodium signal at concentrations below 150 mM in low magnetic fields in the presence of the static gradient is discussed.

4.5.1 Simulation of the magnetic field of the Oxford magnet and Gaussmeter measurements

Before conducting experiments in an inhomogeneous field of a superconducting magnet, the fringe field of the used magnet should be investigated, and the appropriate field strength chosen and its position found. As mentioned earlier in Subsection 4.2, the choice of 0.5 T field strength was influenced by several practical considerations. NMR devices based on permanent magnets up to 2 T have been used in a variety of applications (Blümich et al., 2009) and they are portable. This factor is taken into consideration as current work with constructed probes may serve as a basis for constructing a portable mobile device based on permanent magnets in the future. Thus, the results presented in this thesis serve as a modelling of the setup with a permanent magnet with several simplifications: the magnetic field gradient of the configuration described in this thesis 4.2 T/m is much lower than in classical portable MRI systems: 11-20 T/m depending on a magnetic field used (Perlo et al., 2005). A 0.5 T field strength is high enough to provide good sensitivity for sodium measurements and 0.5 T isoline is located outside the magnet bore giving more space for bigger coils and to perform stray field measurements.

For a better understanding of the magnetic field geometry produced by the superconducting magnet Oxford, the magnet was approximated as a simple one-layered solenoid in the computer simulations in MATLAB (Subsection 4.4.1).

Although the structure of commercial NMR spectrometers, especially shielded ones, is much more complicated than this modelled system, it is accurate enough. Results of the simulation predict experimental measurements with the gaussmeters (Subsection 4.4.2) very well.

From Figure 4.11, it can be seen that 0.5 T isolines are perpendicular to the z-axis at distances far outside of the solenoid and they are convex. Inside the magnet bore and closer to its edge, the lines are concave (Randall, 2011). Thus, following the direction on the z-axis from 0.5 T towards the edge of the magnet, the isolines become flatter and flatter changing from convex to concave shape. Additionally, the field gradient increases, and its maximum is achieved at the edge of the magnet bore (Randall, 2011). According to eq. [4.1], a larger gradient reduces the thickness of the excited slice. On one hand, having a flatter field profile and a higher gradient is more beneficial for high-resolution profiling of planar samples like human skin (Mitchell et al., 2006). On the other hand, it leads to a decrease in sensitivity and SNR. As the high-resolution profiling was not the goal of this thesis, the flatness of the excited slice was not important. Therefore, volume coils and long samples were used in this work, as gain in SNR for a low sensitive nucleus as ^{23}Na was a priority in this thesis.

According to Figure 4.13, the 24-mm probe covers approximately 20 kHz of the frequency offset, while the 40-mm probe covers up to 80 kHz depending on the accuracy of probe positioning under the magnet.

4.5.2 Design of the home-built probe

The 40-mm probe was constructed to investigate the effect of an increased number of spins in the sensitive slice compared to a smaller diameter 24-mm probe used previously (Unpublished data, 2018). In addition, the length of the 40-mm probe is smaller than its diameter to reduce the length of the used conductor and consequently reduce noise.

A way to produce a larger magnetic field B_1 is the use of additional turns to obtain the largest field for a given current. However, the noise contribution will increase accordingly as the wire resistance will increase with the number of turns, i.e. with the length l of the conductor. The inductance of the ribbon wire is proportional to its length (Terman, 1943), and the sensitivity $B_1/i \sim l$. Hence, according to eq. [4.19], the coil's

SNR is almost independent on l. Therefore, the small amount of wire used to wound the coil for the 40-mm should be beneficial for SNR.

The coils used in this thesis have low Q-factors: 58 for the 24-mm probe and 68 for the 40-mm probe (Subsection 4.3.2). It is worth noting that a high Q does not guarantee a high coil SNR (Watzlaw et al., 2013). Comparably low-Q coils can provide a high SNR if their sensitivity is maximized. Furthermore, low-Q coils can give shorter dead times which provide shorter TE which results in collection of more echoes during specified T_2.

4.5.3 Measurements of sodium signal in solutions of different concentrations of NaCl

In this thesis, measurements of the sodium signal from saline solutions with different concentrations of NaCl were performed using a probe with an RF coil of 40-mm diameter constructed in-house. In experiments with phantoms with a decreasing concentration of NaCl, the feasibility of detecting the sodium signal with the assembled probe was demonstrated and the influence of different parameters was evaluated.

Quadrature echoes were widely used in NMR in inhomogeneous fields, especially in GARField and STRAFI, even when there is no need to refocus large couplings (Backhouse et al., 2004; Ciampi et al., 2011; McDonald et al., 2005; McDonald & Newling, 1998; Stapf & Han, 2006). This choice of the pulse sequence is justified by a desire to keep the excitation bandwidth of all 90° pulses the same without a requirement to double the power in the case of 180° refocusing pulses (Mitchell et al., 2006). However, the use of the CPMG pulse sequence with its 180° pulses refocuses all the magnetization, apart from any loss due to relaxation and diffusion. This gives an advantage compared to the quadrupolar echo where two 90° pulses are used. When the first pulse is 90°, different echo amplitude can be obtained from a spin-3/2 system depending on a flip angle of the second pulse: an echo originated only from a central $|1/2\rangle \rightarrow |-1/2\rangle$ transition has its maximum when the flip angle of the second pulse is equal to 180°; a total signal originated from contributions of both central and satellite ($|1/2\rangle \rightarrow |3/2\rangle$ and $|-3/2\rangle \rightarrow |-1/2\rangle$) transitions is maximum at the flip angle either much lower than 90° or 180° (Man, 1995). These factors make CPMG more beneficial for SNR than the quadrupolar echo.

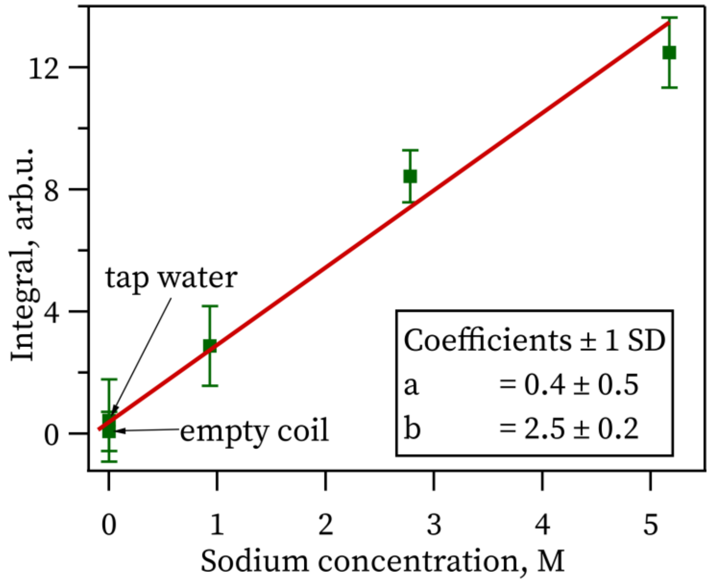

Figure 4.20. Sodium concentration calibration obtained by the 40-mm coil. Each point is an integral of the echo spectrum obtained in 7200 scans.

The performance of the 40-mm probe was tested by carrying out experiments with the same parameters for a range of phantoms: 5.17 M table salt, 2.78 M NaCl and 0.93 M NaCl water solutions. Spectra integrals from the same frequency range for every phantom were calculated and plotted vs sodium concentration to build a calibration curve (Figure 4.20). A signal corresponding to the concentration of 0 M NaCl was obtained by running the same experiment as for the phantoms but with an empty coil and a sample with tap water for comparison. It can be seen that the calibration curve follows a positive linear correlation. This serves as an indicator of the appropriate performance of the probe.

T_1 of saline solutions with different concentrations of NaCl was not measured specifically in this study, however, T_1 of sodium in a water solution and even T_2 can be considered field-independent (Mitchell, 2016). Water solutions with the highest NaCl concentration have the shortest T_1 and T_2. According to Figure 4.21, with change in sodium concentration from 5.17 M to 0.125 M T_1 (and T_2 considering that $T_1 \approx T_2$ for salt aqueous solutions) will increase about 1.7 times. Therefore TR that should be about $5T_1$ – a minimum of 300 ms. In the "CPMGAdd" experiments with the 40-mm probe (Subsection 4.4.3), TR could be reduced from 500 ms (or 1 s for the 0.125 NaCl) to 300 ms (Table 4.2). However, this would still result in a very long measurement time nearly 3 hours to obtain the same SNR of 7.7 for the 0.125 NaCl that was achieved in this work with echo-adding techniques. Such a long measurement time will not be feasible, especially *in vivo*. Using the 24-mm probe, an SNR of 7.8 was achieved in 1 h 22 min for the 0.125 M NaCl sample (Unpublished data, 2018). However, $TR = 150$ ms was used which might have caused not fully recovered magnetization and hence reduced SNR. An increase in TR to the appropriate 300 ms would increase the

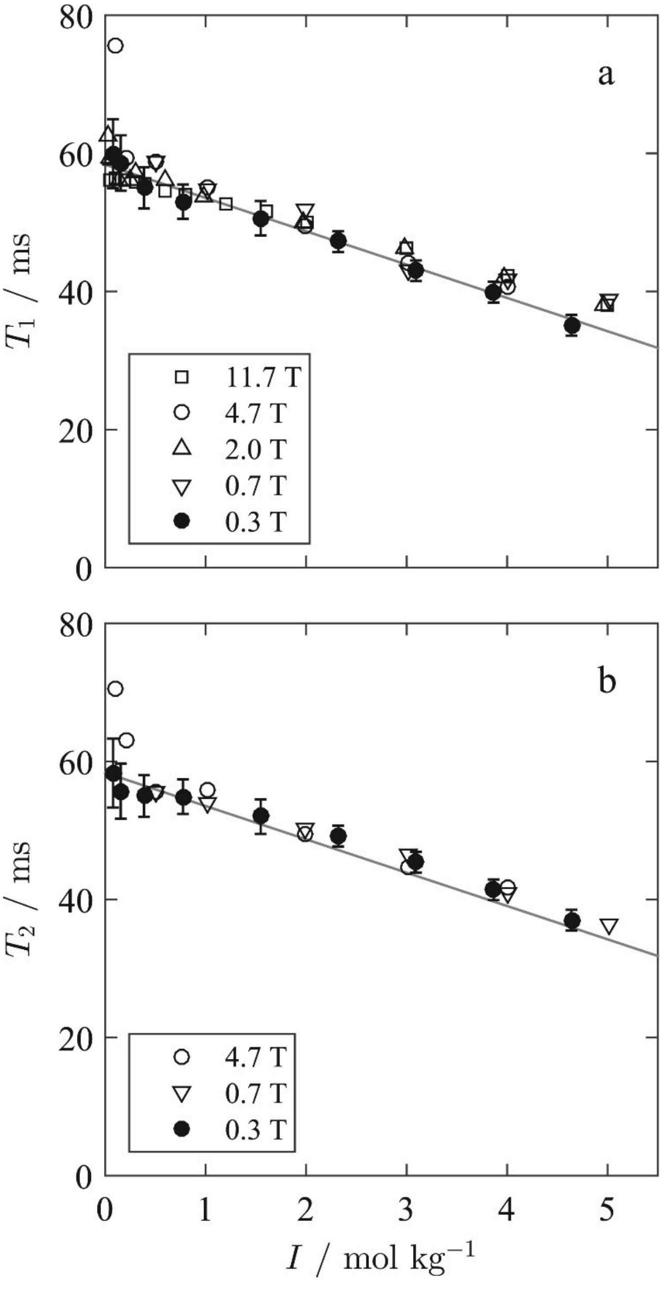

Figure 4.21. The relaxation times (a) T_1 and (b) T_2 of sodium in NaCl solutions as a function of ionic strength at different magnetic field strengths. In each graph, the solid grey line represents the theoretical relaxation behaviour, as described by eq. (1) in (Mitchell, 2016). The relaxation times are unaffected by changes in magnetic field strength. Figure is reproduced from (Mitchell, 2016).

measurement time twice. Therefore, the application of the Ernst angle (Ernst et al., 1987) can be considered in the future. However, in the case of tissue equivalent phantoms like agarose phantoms, the acquisition process can be faster due to shorter T_1: in the phantom consisting of 4% agar gel with 135 mM NaCl T_1 was measured to be 39 ms in 9.4 T (Hu, 2020). According to Table 2.2, T_1 of "solid" tissues (not including blood and cerebrospinal fluid) is less than 35 ms. This would lead to a reduction of TR to 200 ms, and consequently experimental time to less than 2 hours. However, SNR per unit of time will also rely on short echo times to collect the maximum amount of echoes per T_2 as sodium's long transverse relaxation time of tissues, T_{2long}, is shorter than in aqueous solutions of NaCl (Table 2.2 and also Table 1 in (Constantinides et al., 2000)).

The reported sodium concentration in the skin is about 80 mM (Hanson et al., 2021) which is even lower than the lowest NaCl concentration measured in this Chapter. This means that it would take even longer to obtain a sodium signal from a phantom of water solution with the sodium concentration near the skin one to achieve approximately the same SNR in an inhomogeneous field. As sodium experiences a biexponential relaxation in the skin due to interaction with its macromolecules (Hanson et al., 2021), an additional signal loss might be expected due to short T_2 component when registering the sodium signal from a tissue itself *ex vivo* or *in vivo*. Therefore, short TE, reduction of noise and increase in the slice thickness are crucial factors for sodium signal measurements at concentrations below 100 mM.

However, an optimal 90° pulse was not precisely found for the phantoms with sodium chloride concentration below 2.78 M for the 40-mm probe. For the concentrations below 0.5 M, this task is particularly difficult due to low SNR making the measurements extremely long: more than 10 hours to collect 5 points with SNR as in Figure 4.15(d)-(f) (considering TR $\approx 5T_1$). Therefore, it might be better to obtain parameters of the optimal pulses in the homogeneous field if there is a magnet or a scanner with the appropriate field strength available. However, this procedure is complicated by the fact that the Kea^2 spectrometer and an external amplifier should be transferred to the scanner which is not an easy task. Nevertheless, a potentially higher SNR may be achieved with a precisely calibrated pulse.

Using the 40-mm probe, transverse relaxation time T_2 of the 5.17 M water solution of the table salt was measured 29.7 ± 1.8 ms which is 1.13 times shorter than one reported in reference (Mitchell, 2016), about 34 ms. This phenomenon might be attributed to several factors. In relaxation time measurements, apart from a T_2-decay, additional signal attenuation is observed in liquid samples due to molecular self-diffusion in the presence of a strong magnetic field gradient. Therefore, the relaxation time extracted from the fitting of the echo train is not the same T_2 measured in a homogeneous field but an effective T_{2eff} which is weighted by an additional diffusion term $\frac{1}{12}(\gamma G_0 \cdot TE)^2 D$ (eq. [4.5]) and moreover is modified by off-resonance impact and flip angle variations in the inhomogeneous B_0 and B_1 fields correspondingly. From Figure 4.22, the diffusion coefficient of sodium ions Na^+ in the 5.17 M NaCl can be estimated: $D = 0.69 \cdot 10^{-9}$ m^2/s. Therefore, the diffusion term $\frac{1}{12}(\gamma G_0 \cdot TE)^2 D$ can be calculated: with $\gamma = 70.761 \cdot 10^6$ rad/(s·T) for sodium, gradient 4.02 ± 0.19 T/m and $TE = 300$ μs, it equals to 0.42 1/s. Compared to the attenuation caused by relaxation $1/T_2 = 33.67$ 1/s it is extremely small. This means that CPMG reduces the effect of diffusion very well.

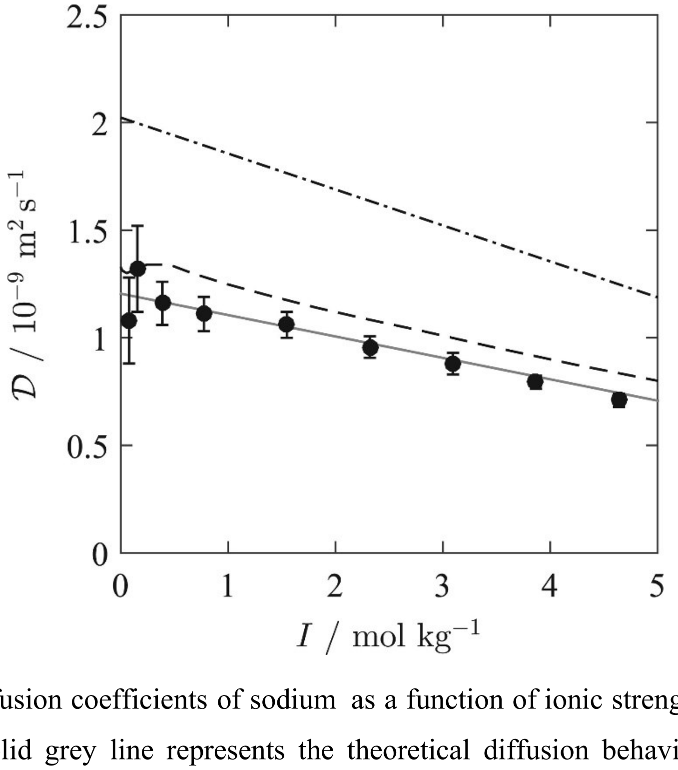

Figure 4.22. Diffusion coefficients of sodium as a function of ionic strength in NaCl water solutions. The solid grey line represents the theoretical diffusion behaviour described by eq. (3) in (Mitchell, 2016). The dash-dot line indicates the corresponding ^{1}H diffusion coefficients. Figure is reproduced from (Mitchell, 2016).

The effect of diffusion during the length of rf pulses and one TE interval can be ignored. However, the fluctuations in the nutation frequency Ω of sodium spins are negligible only when they travel a distance much smaller compared to the slice thickness during the measurement according to eq. [4.31] (Hürlimann, 2001):

$$\sqrt{D \cdot T_{exp}} \ll \omega_1/\gamma G_0. \tag{4.31}$$

In the case of the CPMG experiment resulted in Figure 4.17(a), T_{exp} is equal to $n_e \cdot TE = 76.8$ ms. Then $\sqrt{D \cdot T_{exp}} = 7.3$ μm. Using eq. [3.5], the right part of the inequality [4.31] can be transformed into $\theta/\gamma\tau_p G_0$, and with the flip angle $\theta = \pi/2$, $\gamma = 70.761 \cdot 10^6$ rad/(s·T) for sodium, the pulse length $\tau_p = 60$ μs and the gradient $G_0 = 4.02$ T/m it equals to 92 μm. These calculations show that for some sodium ions in the thin slice, the inequality [4.31] is not fulfilled to the highest extent and they have a bigger chance to escape from the slice by the end of the measurement time T_{exp} and they will not contribute to the signal which leads to a reduction of the bulk T_{2eff}.

In addition, radiation absorption by conducting samples (Dick et al., 2019) causes heating of the samples, especially when a train of pulses with a 300 μs gap between them is applied. Increasing the temperature of the sample could be the main mechanism responsible for the shortening of the measured T_2 of the 5.17 table sample.

The phantom studies possess several limitations. The use of water solutions of NaCl as phantoms may not be able to exactly predict the sodium signal behaviour in biological tissues *in vitro* or *in vivo*. To obtain results that can model and predict the results in living tissues, phantoms with matching relaxation properties are required (Woessner, 2001). In addition, diffusion of sodium ions in biological tissues is much more restricted (Eliav et al., 2013), thus its contribution to a signal decay (eq. [4.5]) will be reduced compared to a case in a water solution (Mitchell, 2016).

In this thesis, the STRAFI setup for the measurements of sodium signal from liquid samples is reported for the first time to the best of the Author's knowledge. Compared to the work of (Zia, 2016) with the portable sensor based on a permanent magnet, sodium measurements in inhomogeneous fields were demonstrated for concentrations much lower than saturated NaCl.

4.5.3.1 Comparison of two coils with different diameters

When the coils were used to perform the “CPMGAdd” experiments with the identical scanning parameters for sodium nuclei, the same samples and the shield, the wider (40-mm) probe gave higher signal integral compared to the smaller (24-mm) coil, but this increase was much smaller (1.4 times) than expected from 6-times enlargement in the area of the excitation slice. One of the reasons for the observed effect might be that the sensitivity B_1/i of the saddle coil as a homogeneous resonator is in inverse relation to its diameter (Mispelter & Lupu, 2008). In this case, a 1.7 times increase in diameter will provoke a loss in sensitivity of the same magnitude.

In addition, a presence of a shield is affecting the sensitivity of a coil and its influence depends on the ratio of diameters of the shield and the coil (Mispelter & Lupu, 2008). As the same 67.4-mm wide shield made from the copper foil was used with both coils (described in Subsection 4.3.2) in comparison experiments (Subsection 4.4.3.1), for the 24-mm probe the ratio of diameter of the shield to the coil’s diameter is larger than for the 40-mm probe which results in a smaller reduction of the magnetic field inside the coil for the 24-mm probe compared to the 40-mm probe. Both reasons described above led to an unproportional decrease in the signal for the 40-mm probe that resulted in a decrease in SNR.

Moreover, Table 4.5 shows SNR values of sodium spectra obtained in the number of scans N for experiments performed with the 40-mm probe (described in Subsection 4.4.3) and the 24-mm probe (Unpublished data, 2018). For further comparison, the SNR values were divided by $\sqrt{N}$ to obtain characteristic coefficients which are proportional to SNR per one scan $SNR_1(t)$ (according to equation [4.20]) and additionally were divided by the size of the excitation volume (in mm^3) resulting in “SNR per scan per unit volume” (right section in Table 4.5). These coefficients are plotted vs sodium concentration in Figure 4.23. It can be seen that despite almost the 3-times increase in the excitation volume for the 40-mm probe, the smaller 24-mm probe gives better SNR per scan per unit of volume.

From Figure 4.23 it can be seen that the performances of two coils with their optimal setup and scanning parameters used for phantoms with different NaCl concentrations are very different showing much higher SNR per scan per unit volume for the 24-mm probe. A gain in SNR with the 40-mm probe was not achieved due to several reasons:

Table 4.5. SNR values of sodium spectra obtained with the 24-mm and 40-mm probes with the indicated number of scans N and excitation volume V for different samples. The last column behind the border shows a calculated coefficient "SNR per 1 scan per unit volume" (calculated as obtained SNR divided by $\sqrt{N}$ and V) with graphical presentation in Figure 4.23.

Phantom/probe	**24-mm**			**40-mm**			$\frac{SNR}{\sqrt{N}\cdot V} \sim \frac{SNR_1(t)}{V}, \cdot 10^3$	
	N	V,**mm**^{3}	**SNR**	N	V,**mm**^{3}	**SNR**	**24-mm**	**40-mm**
Saturated NaCl/ 5.17 M table salt	3600	70±3	81.7	3600	204±10	74.7	19.48±0.79	6.09±0.29
2.78 M NaCl	-	-	-	3600	197±9	43.7	-	3.70±0.17
0.93 M NaCl	12800	70±3	42	7200	204±10	33.9	5.31±0.22	1.96±0.09
0.5 M NaCl	8192	70±3	13.5	25600	204±10	35.8	2.13±0.09	1.10±0.05
0.25 M NaCl	12800	70±3	14	25600	204±10	11.8	1.77±0.07	0.36±0.02
0.125 M NaCl	32768	70±3	7.8	32768	204±10	7.7	0.62±0.03	0.21±0.01

(1) a wider coil requires a longer pulse: this leads to an increase in minimal possible TE even without considering an internal duty cycle of the Kea^2 spectrometer. This results in the fact that fewer echoes will be added together for a given T_2. This factor is especially crucial for sodium in biological tissues with their short T_2s (Table 2.3) and in particular for the human skin, transverse relaxation times of which were determined in Chapter 3 . (2) For the 40-mm probe constructed in this thesis, with the 60 μs excitation pulse with the optimized amplitude, 4.02 ± 0.19 T/m field gradient at the probe's position in 0.485 T, the thickness of the excitation slice is calculated to be 184 ± 18 μm (Subsection 4.4.3). Even with a lower gradient compared to the 24-mm probe's position (4.7 ± 0.2 T/m, (Unpublished data, 2018)), the slice thickness with the 40-mm probe setup is more than twice smaller due to an exceedingly longer pulse. (3) Wider coil produces a lower magnetic field per unit of current B_1/i that was discussed at the beginning of this section. Also, according to eq. [2.12] the equilibrium magnetization is directly proportional to the spin number, but inversely proportional to the volume. Therefore, a higher concentration of sodium nuclei will produce a higher signal. (3) Copper foil comprising the shield might not be thick enough to protect from low-frequency noise. According to eq. [4.21], skin depth is inversely

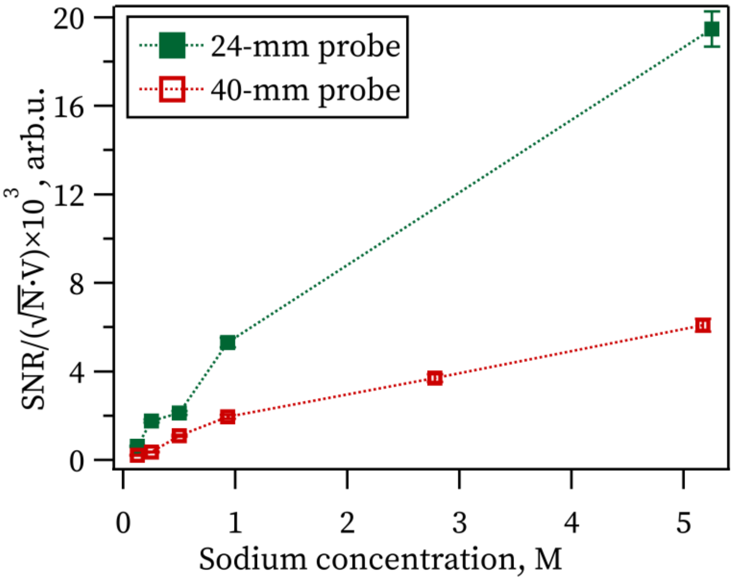

Figure 4.23. Coefficients $SNR/(\sqrt{N} \cdot V)$ proportional to $SNR_1(t)$ per unit volume for both 24- and 40-mm probes and different samples are plotted vs sodium concentration (the values are taken from the right column of Table 4.5). Experimental points are connected by straight dashed lines to guide the eye.

proportional to the frequency. A thicker shield might be required in the future. A thicker aluminium shield was implemented with the 24-mm probe for proton and sodium measurements (Unpublished data, 2018) but was removed for comparison experiments. With the 24-mm probe, these factors enabled measurements with the same SNR of sensitive areas almost 6 times smaller even with the not maximized filling factor (a sample diameter was 15.4 mm (Unpublished data, 2018)) than the wider 40-mm coil. Additionally, using shorter TE with the smaller coil would give a benefit of the measurement of a short component of T_2 relaxation time more accurately in samples like polymer gels and biological tissues like skin.

The performed measurements comparing probes with different diameters showed that the smaller coil is preferred. As can be seen from Figure 3.16, sodium in the skin is mainly located in the dermis which is only about 4 mm deep. Therefore, in the future, the presented work can be translated into work with planar coils of comparable diameter and permanent magnets to construct a portable, movable device which can be delivered to a patient and will be able to measure sodium relaxation parameters in human skin *in vivo* on a particular skin depth. Furthermore, if an expansion of the area of the sensitive slice is needed, several smaller coils may be combined to constitute planar arrays. Although, because of the low frequency and high magnetic field gradient, the presented experiments are mainly dominated by coil noise, an array assemblage may still result in an SNR enhancement compared to one large coil (Roemer et al., 1990).

4.6 Conclusion

The feasibility of sodium measurements in phantoms with NaCl concentrations in a range of [0.125, 5.17] M was demonstrated. The measurements were performed by a probe built in-house.

Even with the longer length of the conductor comprising the 24-mm coil, it was shown that its sensitivity is better than that of the 40-mm coil. Shorter pulses for the smaller coil give shorter TE which leads to an increase in SNR even with the reduced filling factor compared to the wider probe in this study. Also, a CPMG pulse sequence excites the frequency bandwidth reciprocal to pulse length (eq. [4.10]), thus by increasing the pulse length the slice thickness is reduced. An increase in diameter making the excitation slice bigger might not be enough to compensate for this effect. Measurements of samples with short T_2 (or short T_{2short}) will benefit from using a small coil as the steep beginning of the decay will be covered with more measuring points due to shorter TE.

The measurement time becomes the limiting factor for the shortest possible echo time. As the length of the RF pulses in a pulse sequence defines the excitation bandwidth, the longer pulses provide broader echoes (Casanova et al., 2011). In addition, an increase in t_{acq} lowers the number of echoes n_e used for summation as $n_e = T_2/TE$. It was also shown that maximum sensitivity is obtained when the time used to acquire an echo is equal to the length of the excitation RF pulse. Therefore, shorter pulses provided by the smaller coil will give the benefit of lower acquisition time, thicker excitation slices and consequently shorter measurement time with maximum sensitivity.

5 Conclusion and Outlook

The first part of the work in this thesis focused on the application and analysis of NMR spectroscopy to investigate sodium relaxation in *ex vivo* skin samples of patients with type 2 Diabetes Mellitus and control counterparts in ultra-high field of 9.4 T. In particular, single quantum and multiple quantum techniques, i.e. CPMG, DQF-MA and TQF spectroscopy, have been applied and the time evolution of coherences was analysed to determine short and long relaxation time components, T_{2short} and T_{2long}, of sodium in the skin and quadrupolar coupling ω_Q.

In Chapter 3 , in an ultra-high field of 9.4 T a CPMG pulse sequence was applied for measurements of sodium signal decay in the skin samples *ex vivo* for the first time. Echo integrals vs echo time were fitted with a bi-exponential decay function to obtain T_{2short} and T_{2long}. Sodium relaxation behaviour was compared between the abdomen skin samples and the ones obtained from the foot/leg of control patients and no significant difference was found for both T_{2short} and T_{2long}. Then both skin locations together within the control group were compared with the diabetic group (only foot/leg samples). No significant difference was found for T_{2short}, however, T_{2long} of the diabetic patients was significantly lengthened compared to controls.

In addition, sodium DQF-MA and TQF spectroscopy was performed on the same skin samples in 9.4 T for the first time. DQF-MA experiment is only sensitive to sodium involved in quadrupolar interaction and TQF obtains signal only from slow-moving sodium, thus no contamination from free fast-moving sodium is detected. The evolution of the DQF-MA signal vs preparation time was analysed and T_{2short} and quadrupolar coupling ω_Q were obtained. Then these parameters were set as fixed when analysing TQF build-up behaviour to obtain T_{2long}. It was found that abdomen samples have different T_{2short} than foot/leg samples within the control group that was not observed in the SQ experiment (Figure 3.19). Quadrupolar coupling constant ω_Q was found indifferent to the skin location, however, with the trend of diminishment in the foot/leg control samples. No significant difference for ω_Q was found between diabetic patients and combined control patients. Significant lengthening of T_{2long} was observed in the T2DM group compared to the control group that was in agreement with the CPMG experiment. This study suggested that differences in the sodium molecular environment in T2DM and the control population can be probed by determining sodium relaxation times using the SQ and MQ spectroscopic techniques.

The second part of the work in this thesis has focused on the development of a setup to perform sodium measurements in inhomogeneous fields of low strength. In Chapter 4 , firstly the magnetic field of a poor-shielded 9.4T magnet was simulated and then measured with gaussmeters to confirm the results of the simulations. Secondly, an additional probe with a 37.6-mm diameter (named as the 40-mm probe) was constructed in addition to the existing 24-mm probe that was already built in our laboratory earlier. Then measurements of sodium signal were performed using the 40-mm probe in phantoms with decreasing concentrations of sodium chloride from 5.17 M to 0.125 M at around 0.5 T with a field gradient of about 4.1 T/m for the first time. It was shown that the coil with a smaller diameter gives better SNR and shorter measurement time.

This thesis has shown the applicability of SQ and MQF spectroscopy in the *ex vivo* skin samples of control and diabetic patients. Logarithmic time spacing in a CPMG experiment can be adapted in the future to increase temporal resolution, especially at the beginning of the signal decay. Additional DQF-MA experiments can be performed to study the time evolution of the coherences to determine if there is more than one population of sodium involved in quadrupolar interaction. As an alternative, 2-dimensional DQF-MA experiments can be implemented where time intervals between $\theta_1 - \theta_2$ and $\theta_2 - \theta_3$ 90° pulses (eq. [3.1], Figure 3.3) are incremented (Rooney & Springer, 1991a). According to (Rooney & Springer, 1991b), varying the delay between the second and third 90° pulse will help to determine the number of sodium populations in slow exchange. Then the analysis of the DQF-MA and TQF build-up behaviours should be adapted accordingly by developing new fitting functions that take into account more than one sodium population. Resolution in the preparation time domain in the MQ experiments can be increased to match the number of parameters of the new fitting functions.

In the future, these techniques can be translated into an investigation of skin sodium in other diseases with sodium disbalance like chronic kidney disease, and cystic fibrosis (CF) of lungs and other organs (Yu & Sharma, 2022). CF patients are recommended to increase sodium in their diet to compensate for its increased loss in sweat. It was found that sodium concentration in the sweat of CF patients does not depend on dietary sodium load or the amount of exercise (Declercq et al., 2020). Adequate monitoring of sodium status is highly required. As the skin was found to be involved in the regulation of sodium homeostasis in the human body, future studies are needed to investigate sodium in the skin of CF patients. In addition, techniques described in the thesis can be applied to estimate the effect of haemodialysis on sodium removal in the skin more accurately compared to existing studies using a clinical scanner (Dahlmann et al., 2015). To reduce the invasiveness of the investigation procedures, instead of *ex vivo* skin samples current methods can be adapted to punch biopsies in the future.

This thesis has demonstrated the feasibility of the acquisition of sodium signal in a low inhomogeneous field of a poor-shielded superconducting magnet using home-build probes. In the future, aqueous solutions of NaCl can be substituted with tissue-equivalent gel phantoms with matching relaxation characteristics to biological tissues *in vivo*. All described experiments were run at room temperature. The next future step could be conducting sodium measurements at temperatures close to 37°C in gel phantoms in inhomogeneous fields and comparing them with results in homogeneous fields. Construction of the probes can be improved by substituting isolated wires with circuit boards and etching techniques to reduce the mechanical vibrations of the circuit elements during operation.

Results obtained in the ultra-high (Chapter 3) and low inhomogeneous fields (Chapter 4) could serve as a preface to the development of a portable and mobile NMR device constructed specifically for measurements of sodium signal in human skin of patients which cannot be put inside a clinical NMR scanner. To achieve a mobility of the device, it should be based on permanent magnets and with an accessible side that can be in a close contact with skin of a patient (possible design like in (Anferova et al., 2002)). To ensure the comfort of the patient during measurements but also to prevent relative movements of the patient's measured body part and the device, a specially designed support is needed (Haken & Blümich, 2000). This NMR device could help to study sodium in the skin noninvasively, it would be delivered to a patient and have a probe with an excitation slice that would target certain depths in the skin. Different coil geometries can be used for this task (Anferova et al., 2002; Blümich et al., 2008). This device could help to monitor the efficiency of different interventions like new and existing medications and treatments like haemodialysis.

References

Alberts, B., Johnson, A., Julian, L., Morgan, D., Raff, M., Roberts, K., & Walter, P. (2015). *Molecular Biology of the Cell* (6th ed.). Garland Science.

Anderegg, U., Simon, J. C., & Averbeck, M. (2014). More than just a filler - the role of hyaluronan for skin homeostasis. *Experimental Dermatology*, *23*(5), 295–303. https://doi.org/10.1111/exd.12370

Anferova, S., Anferov, V., Adams, M., Blumler, P., Routley, N., Hailu, K., Kupferschlager, K., Mallett, M. J. D., Schroeder, G., Sharma, S., & Blümich, B. (2002). Construction of a NMR-MOUSE with Short Dead Time. *Concepts in Magnetic Resonance (Magnetic Resonance Engineering)*, *15*(1), 15–25. https://doi.org/10.1002/mre.10013

Argyropoulos, A. J., Robichaud, P., Balimunkwe, R. M., Fisher, G. J., Hammerberg, C., Yan, Y., & Quan, T. (2016). Alterations of dermal connective tissue collagen in diabetes: Molecular basis of aged-appearing skin. *PLoS ONE*, *11*(4), 1–17. https://doi.org/10.1371/journal.pone.0153806

Backhouse, L., Dias, M., Gorce, J. P., Hadgraft, J., McDonald, P. J., & Wiechers, J. W. (2004). GARField magnetic resonance profiling of the ingress of model skin-care product ingredients into human skin in vitro. *Journal of Pharmaceutical Sciences*, *93*(9), 2274–2283. https://doi.org/10.1002/jps.20137

Barros, L. F., Castro, J., & Bittner, C. X. (2002). Ion Movements in Cell Death: from protection to execution. *Biological Research*, *35*(2), 209–214. https://doi.org/10.4067/S0716-97602002000200012

Baumann, M. A., Doll, G. M., & Zick, K. (1993). Stray-field imaging (STRAFI) of teeth. *Oral Surgery, Oral Medicine, Oral Pathology, and Oral Radiology*, *75*, 517–522.

Bhave, G., & Neilson, E. G. (2011). Body Fluid Dynamics: Back to the Future. *Journal of the American Society of Nephrology*, *22*(12), 2166–2181. https://doi.org/10.1681/ASN.2011080865

Bi, X., Li, G., Doty, S. B., & Camacho, N. P. (2005). A novel method for determination of collagen orientation in cartilage by Fourier transform infrared imaging spectroscopy (FT-IRIS). *Osteoarthritis and Cartilage*, *13*(12), 1050–

1058. https://doi.org/10.1016/j.joca.2005.07.008

Blank, A., Alexandrowicz, G., Muchnik, L., Tidhar, G., Schneiderman, J., Virmani, R., & Golan, E. (2005). Miniature self-contained intravascular magnetic resonance (IVMI) probe for clinical applications. *Magnetic Resonance in Medicine*, *54*(1), 105–112. https://doi.org/10.1002/mrm.20537

Blümich, B., Casanova, F., & Appelt, S. (2009). NMR at low magnetic fields. *Chemical Physics Letters*, *477*(4–6), 231–240. https://doi.org/10.1016/j.cplett.2009.06.096

Blümich, B., Perlo, J., & Casanova, F. (2008). Mobile single-sided NMR. *Progress in Nuclear Magnetic Resonance Spectroscopy*, *52*(4), 197–269. https://doi.org/10.1016/j.pnmrs.2007.10.002

Boada, F. E., Qian, Y., Nemoto, E., Jovin, T., Jungreis, C., Jones, S. C., Weimer, J., & Lee, V. (2012). Sodium MRI and the Assessment of Irreversible Tissue Damage During Hyper-Acute Stroke. *Translational Stroke Research*, *3*(2), 236–245. https://doi.org/10.1007/s12975-012-0168-7

Boada, F., LaVerde, G., Jungreis, C., Nemoto, E., Tanase, C., & Hancu, I. (2005). Loss of Cell Ion Homeostasis and Cell Viability in the Brain: What Sodium MRI Can Tell Us. *Current Topics in Developmental Biology*, *70*(05), 77–101. https://doi.org/10.1016/S0070-2153(05)70004-1

Bodart, P., Nunes, T., & Randall, E. W. (1997). Stray-field imaging of quadrupolar nuclei of half integer spin in solids. *Solid State Nuclear Magnetic Resonance*, *8*(4), 257–263. https://doi.org/10.1016/S0926-2040(97)00005-2

Borthakur, A., Hancu, I., Boada, F. E., Shen, G. X., Shapiro, E. M., & Reddy, R. (1999). In Vivo Triple Quantum Filtered Twisted Projection Sodium MRI of Human Articular Cartilage. *Journal of Magnetic Resonance*, *141*(2), 286–290. https://doi.org/10.1006/JMRE.1999.1923

Borthakur, A., Shapiro, E. M., Beers, J., Kudchodkar, S., Bruce Kneeland, J., & Reddy, R. (2002). Effect of IL-1β-induced macromolecular depletion on residual quadrupolar interaction in articular cartilage. *Journal of Magnetic Resonance Imaging*, *15*(3), 315–323. https://doi.org/10.1002/jmri.10074

Brown, S. P., & Wimperis, S. (1994). NMR measurement of spin-3/2 transverse relaxation in an inhomogeneous B1 field. *Chemical Physics Letters*, *224*(5–6), 508–516. https://doi.org/10.1016/0009-2614(94)00572-9

Buist, R. J., Deslauriers, R., Saunders, J. K., & Mainwood, G. W. (1991). 23Na and flame photometric studies of the NMR visibility of sodium in rat muscle. *Canadian Journal of Physiology and Pharmacology*, *69*(11), 1663–1669. https://doi.org/10.1139/y91-247

Burnier, Michael. (2007). Sodium in Health and Disease. In Michel Burnier (Ed.), *Sodium in Health and Disease*. Informa Healthcare USA, Inc. https://doi.org/10.3109/9781420020946

Burstein, D., & Springer, C. S. J. (2019). Sodium MRI revisited. *Magnetic Resonance in Medicine*, *82*(2), 521–524. https://doi.org/10.1002/mrm.27738

Callaghan, P. T. (1991). *Principles of Nuclear Magnetic Resonance Microscopy*. Clarendon Press.

Carr, H. Y., & Purcell, E. M. (1954). Effects of diffusion on free precession in nuclear magnetic resonance experiments. *Physical Review*, *94*(3), 630–638. https://doi.org/10.1103/PhysRev.94.630

Casanova, F., Perlo, J., & Blümich, B. (2006). Depth Profiling by Single-sided NMR. In *NMR Imaging in Chemical Engineering* (pp. 107–123).

Casanova, F., Perlo, J., & Blümich, B. (2011). *Single-Sided NMR*. Springer. https://doi.org/10.1007/978-3-642-16307-4

Ciampi, E., Van Ginkel, M., McDonald, P. J., Pitts, S., Bonnist, E. Y. M., Singleton, S., & Williamson, A. M. (2011). Dynamic in vivo mapping of model moisturiser ingress into human skin by GARfield MRI. *NMR in Biomedicine*, *24*(2), 135–144. https://doi.org/10.1002/nbm.1562

Coates, G. R., Xiao, L., & Prammer, M. G. (1999). *NMR logging: principles and applications*. Halliburton Energy Services.

Comper, W. D., & Laurent, T. C. (1978). Physiological function of connective tissue polysaccharides. *Physiological Reviews*, *58*(1), 255–315. https://doi.org/10.1152/physrev.1978.58.1.255

Constantinides, C. D., Gillen, J. S., Boada, F. E., Pomper, M. G., & Bottomley, P. A.

(2000). Human Skeletal Muscle: Sodium MR Imaging and Quantification - Potential Applications in Exercise and Disease. *Radiology*, *216*(2), 559–568. https://doi.org/10.1148/radiology.216.2.r00jl46559

Cuppoletti, J., & Malinowska, D. H. (2012). Ion Channels of the Epithelia of the Gastrointestinal Tract. In *Physiology of the Gastrointestinal Tract* (First Edit, Vol. 2). Elsevier Inc. https://doi.org/10.1016/B978-0-12-382026-6.00069-5

Dahlmann, A., Dörfelt, K., Eicher, F., Linz, P., Kopp, C., Mössinger, I., Horn, S., Büschges-Seraphin, B., Wabel, P., Hammon, M., Cavallaro, A., Eckardt, K.-U., Kotanko, P., Levin, N. W., Johannes, B., Uder, M., Luft, F. C., Müller, D. N., & Titze, J. M. (2015). Magnetic resonance–determined sodium removal from tissue stores in hemodialysis patients. *Kidney International*, *87*(2), 434–441. https://doi.org/10.1038/KI.2014.269

Declercq, D., Van Braeckel, E., Marchand, S., Van daele, S., & Van Biervliet, S. (2020). Sodium Status and Replacement in Children and Adults Living with Cystic Fibrosis: A Narrative Review. *Journal of the Academy of Nutrition and Dietetics*, *120*(9), 1517–1529. https://doi.org/10.1016/j.jand.2020.05.011

Dias, M., Hadgraft, J., Glover, P. M., & McDonald, P. J. (2003). Stray field magnetic resonance imaging: A preliminary study of skin hydration. *Journal of Physics D: Applied Physics*, *36*(4), 364–368. https://doi.org/10.1088/0022-3727/36/4/306

Dick, M. J., Veselinovic, D., & Green, D. (2019). *Eliminate sample heating during common NMR measurements*. https://nmr.oxinst.com/assets/uploads/MagRes/App Notes/GeoSpec/5161_MR_Geospec_Sample_Heating_App note 7_web.pdf

Duer, M. J. (2002). *Solid-State NMR Spectroscopy: Principles and Applications*. Blackwell Science Ltd.

Eidmann, G., Savelsberg, R., Blümler, P., & Blümich, B. (1996). The NMR MOUSE, a mobile universal surface explorer. *Journal of Magnetic Resonance - Series A*, *122*(1), 104–109. https://doi.org/10.1006/jmra.1996.0185

Eliav, U., & Navon, G. (1994). Analysis of Double-Quantum-Filtered NMR Spectra of 23Na in Biological Tissues. *Journal of Magnetic Resonance, Series B*, *103*(1), 19–29. https://doi.org/10.1006/jmrb.1994.1003

Eliav, U., & Navon, G. (1995). Quadrupole-Echo Techniques in Multiple-Quantum-Filtered NMR Spectroscopy of Heterogeneous Systems. In *Journal of Magnetic Resonance, Series A* (Vol. 115, Issue 2, pp. 241–253). https://doi.org/10.1006/jmra.1995.1173

Eliav, U., & Navon, G. (2016a). Multiple quantum MRS. *EMagRes*, *5*(1), 1061–1076. https://doi.org/10.1002/9780470034590.emrstm1448

Eliav, U., & Navon, G. (2016b). Sodium NMR/MRI for anisotropic systems. *NMR in Biomedicine*, *29*(2), 144–152. https://doi.org/10.1002/nbm.3331

Eliav, U., Shinar, H., & Navon, G. (1992). The Formation of a Second-Rank Tensor in 23Na Double-Quantum-Filtered NMR as an Indicator for Order in a Biological Tissue. *Journal of Magnetic Resonance (1969)*, *98*(1), 223–229. https://doi.org/10.1016/0022-2364(92)90128-T

Eliav, U., Xu, X., Jerschow, A., & Navon, G. (2013). Optic nerve: Separating compartments based on 23Na TQF spectra and TQF-diffusion anisotropy. *Journal of Magnetic Resonance*, *231*, 61–65. https://doi.org/10.1016/j.jmr.2013.03.006

Ernst, R. R., Bodenhausen, G., & Wokaun, A. (1987). Principles of Nuclear Magnetic Resonance in One and Two Dimensions. In *Berichte der Bunsengesellschaft für physikalische Chemie*. Clarendon Press. https://doi.org/10.1002/bbpc.198800370

Farrar, T. C., & Becker, E. D. (1971). Pulse and Fourier Transform NMR. In *Pulse and Fourier Transform NMR: Introduction to Theory and Methods*. Academic Press, Inc. https://doi.org/10.1016/c2009-0-22110-6

Fischereder, M., Michalke, B., Schmöckel, E., Habicht, A., Kunisch, R., Pavelic, I., Szabados, B., Schönermarck, U., Nelson, P. J., & Stangl, M. (2017). Sodium storage in human tissues is mediated by glycosaminoglycan expression. *American Journal of Physiology - Renal Physiology*, *313*(2), F319–F325. https://doi.org/10.1152/ajprenal.00703.2016

Fomina, D. V, Sadykhov, E. G., Hanson, P., Philp, C. J., Randeva, H. S., O'Hare, J. P., Pavlova, O. S., Anisimov, N. V, Makurenkov, A. M., Pirogov, Y. A., Barber, T. M., Meersmann, T., & Pavlovskaya, G. E. (2021). Sodium NMR relaxation times of human skin as potential biomarkers for Type 2 Diabetes Mellitus. *Proc.*

Intl. Soc. Mag. Reson. Med. 29, 1791.

Gagnon, K. B., & Delpire, E. (2021). Sodium Transporters in Human Health and Disease. *Frontiers in Physiology*, *11*(February), 1–18. https://doi.org/10.3389/fphys.2020.588664

Gast, L. V., Gerhalter, T., Hensel, B., Uder, M., & Nagel, A. M. (2018). Double quantum filtered 23Na MRI with magic angle excitation of human skeletal muscle in the presence of B0 and B1 inhomogeneities. *NMR in Biomedicine*, *31*(12), 1–16. https://doi.org/10.1002/nbm.4010

Glover, P. M., Aptaker, P. S., Bowler, J. R., Ciampi, E., & McDonald, P. J. (1999). A Novel High-Gradient Permanent Magnet for the Profiling of Planar Films and Coatings. *Journal of Magnetic Resonance*, *139*(1), 90–97. https://doi.org/10.1006/jmre.1999.1772

Goelman, G., & Prammer, M. G. (1995). The CPMG Pulse Sequence in Strong Magnetic Field Gradients with Applications to Oil-Well Logging. *Journal of Magnetic Resonance, Series A*, *113*(1), 11–18. https://doi.org/10.1006/jmra.1995.1050

Greer, M., Chen, C., & Mandal, S. (2019). Autonomous monitoring of fat, water, and sodium content in Cheese products using low-field NMR. *2019 IEEE International Symposium on Circuits and Systems (ISCAS)*, *2019-May*, 1–5. https://doi.org/10.1109/ISCAS.2019.8702695

Grochowski, C., Blicharska, E., Krukow, P., Jonak, K., Maciejewski, M., Szczepanek, D., Jonak, K., Flieger, J., & Maciejewski, R. (2019). Analysis of Trace Elements in Human Brain: Its Aim, Methods, and Concentration Levels. *Frontiers in Chemistry*, *7*, 1–14. https://doi.org/10.3389/fchem.2019.00115

Gurney, M. A., Laubitz, D., Ghishan, F. K., & Kiela, P. R. (2017). Pathophysiology of Intestinal Na+/H+ Exchange. *Cellular and Molecular Gastroenterology and Hepatology*, *3*(1), 27–40. https://doi.org/10.1016/j.jcmgh.2016.09.010

Guyton, A. C., & Hall, J. E. (2006). *Textbook of medical physiology*. Elsevier Saunders.https://openlibrary.org/books/OL18228327M/Textbook_of_medical_physiology

Haacke, E. M., Brown, R. W., Thompson, M. R., & Venkatesan, R. (1999). *Magnetic*

Resonance Imaging. Physical Principles and Sequence Design. John Wiley & Sons, Ltd.

Hahn, E. L. (1950). Spin echoes. *Physical Review*, *80*(4), 580–594. https://doi.org/10.1103/PhysRev.80.580

Haken, R., & Blümich, B. (2000). Anisotropy in Tendon Investigated in Vivo by a Portable NMR Scanner, the NMR-MOUSE. In *Journal of Magnetic Resonance* (Vol. 144, Issue 2, pp. 195–199). https://doi.org/10.1006/jmre.2000.2040

Hammon, M., Grossmann, S., Linz, P., Kopp, C., Dahlmann, A., Garlichs, C., Janka, R., Cavallaro, A., Luft, F. C., Uder, M., & Titze, J. (2015). 23Na magnetic resonance imaging of the lower leg of acute heart failure patients during diuretic treatment. *PLoS ONE*, *10*(10), 1–13. https://doi.org/10.1371/journal.pone.0141336

Hanson, P., Arkill, K. P., Merry, C. L. R., Hussain, M. S., Meersmann, T., Randeva, H. S., Pavlovskaya, G. E., Hare, P. O., Hanson, P., Arkill, K. P., Merry, C. L. R., Hussain, M. S., Meersmann, T., Randeva, H. S., Pavlovskaya, G. E., Hare, P. O., & Barber, T. M. (2022). Novel perspectives of sodium handling in type 2 diabetes mellitus. *Expert Review of Endocrinology & Metabolism*, 1–9. https://doi.org/10.1080/17446651.2022.2092094

Hanson, P., Philp, C. J., Randeva, H. S., James, S., O'Hare, J. P., Meersmann, T., Pavlovskaya, G. E., & Barber, T. M. (2021). Sodium in the dermis colocates to glycosaminoglycan scaffold, with diminishment in type 2 diabetes mellitus. *JCI Insight*, *6*(12), 1–16. https://doi.org/10.1172/jci.insight.145470

Hausmann, D., Konstandin, S., Wetterling, F., Haneder, S., Nagel, A. M., Dinter, D. J., Schönberg, S. O., Zöllner, F. G., & Schad, L. R. (2012). Apparent Diffusion Coefficient and Sodium Concentration Measurements in Human Prostate Tissue via Hydrogen-1 and Sodium-23 Magnetic Resonance Imaging in a Clinical Setting at 3 T. *Investigative Radiology*, *47*(12), 677–682. https://doi.org/10.1097/RLI.0b013e318267bc6f

Hoult, D. I., & Richards, R. E. (1976). The signal-to-noise ratio of the nuclear magnetic resonance experiment. *Journal of Magnetic Resonance (1969)*, *24*(1), 71–85. https://doi.org/10.1016/0022-2364(76)90233-X

Hu, R. (2020). Exploring Quadrupolar Interactions of 23Na and 35Cl with Triple-Quantum MRS/MRI. In *Angewandte Chemie International Edition, 6(11), 951–952.* Ruperto-Carola University of Heidelberg.

Hürlimann, M. D. (2001). Diffusion and Relaxation Effects in General Stray Field NMR Experiments. *Journal of Magnetic Resonance*, *148*(2), 367–378. https://doi.org/10.1006/JMRE.2000.2263

Hürlimann, M. D., & Griffin, D. D. (2000). Spin Dynamics of Carr-Purcell-Meiboom-Gill-like Sequences in Grossly Inhomogeneous B0 and B1 Fields and Application to NMR Well Logging. *Journal of Magnetic Resonance*, *143*(1), 120–135. https://doi.org/10.1006/jmre.1999.1967

IDF. (2021). IDF Diabetes Atlas. 10th edition 2021. In *Diabetes Research and Clinical Practice*. https://doi.org/10.1016/j.diabres.2013.10.013

Iezzi, R., Locci, F., & Mucchetti, G. (2013). Cheese true density prediction by linear equations. *Journal of Food Process Engineering*, *36*(4), 462–469. https://doi.org/10.1111/jfpe.12008

Inglese, M., Madelin, G., Oesingmann, N., Babb, J. S., Wu, W., Stoeckel, B., Herbert, J., & Johnson, G. (2010). Brain tissue sodium concentration in multiple sclerosis: a sodium imaging study at 3 Tesla. *Brain*, *133*(3), 847–857. https://doi.org/10.1093/brain/awp334

Insko, E. K., Kaufman, J. H., Leigh, J. S., & Reddy, R. (1999). Sodium NMR evaluation of articular cartilage degradation. *Magnetic Resonance in Medicine*, *41*(1), 30–34. https://doi.org/10.1002/(SICI)1522-2594(199901)41:1<30::AID-MRM6>3.0.CO;2-U

Ita, K. (2020). Anatomy of the human skin. In *Transdermal Drug Delivery. Concepts and Application* (pp. 9–18). https://doi.org/10.1016/b978-0-12-822550-9.00002-8

Kannenkeril, D., Karg, M. V., Bosch, A., Ott, C., Linz, P., Nagel, A. M., Uder, M., & Schmieder, R. E. (2019). Tissue sodium content in patients with type 2 diabetes mellitus. *Journal of Diabetes and Its Complications*, *33*(7), 485–489. https://doi.org/10.1016/J.JDIACOMP.2019.04.006

Keinan-Adamsky, K., Shinar, H., Shabat, S., Brin, Y. S., Nyska, M., & Navon, G.

(2010). 23Na and 2H magnetic resonance studies of osteoarthritic and osteoporotic articular cartilage. *Magnetic Resonance in Medicine*, *64*(3), 653–661. https://doi.org/10.1002/mrm.22479

Kemp-Harper, R., Brown, S. P., Styles, P., & Wimperis, S. (1994). In Vivo NMR of Sodium Ions in Ordered Environments. *Journal of Magnetic Resonance, Series B*, *105*(2), 199–203. https://doi.org/10.1006/jmrb.1994.1124

Kopp, C., Beyer, C., Linz, P., Dahlmann, A., Hammon, M., Jantsch, J., Neubert, P., Rosenhauer, D., Müller, D. N., Cavallaro, A., Eckardt, K. U., Schett, G., Luft, F. C., Uder, M., Distler, J. H. W., & Titze, J. (2017). Na+ deposition in the fibrotic skin of systemic sclerosis patients detected by 23Na-magnetic resonance imaging. *Rheumatology (United Kingdom)*, *56*(4), 556–560. https://doi.org/10.1093/rheumatology/kew371

Kopp, C., Linz, P., Dahlmann, A., Hammon, M., Jantsch, J., Müller, D. N., Schmieder, R. E., Cavallaro, A., Eckardt, K.-U., Uder, M., Luft, F. C., & Titze, J. (2013). 23Na Magnetic Resonance Imaging-Determined Tissue Sodium in Healthy Subjects and Hypertensive Patients. *Hypertension*, *61*(3), 635–640. https://doi.org/10.1161/HYPERTENSIONAHA.111.00566

Kopp, C., Linz, P., Maier, C., Wabel, P., Hammon, M., Nagel, A. M., Rosenhauer, D., Horn, S., Uder, M., Luft, F. C., Titze, J., & Dahlmann, A. (2018). Elevated tissue sodium deposition in patients with type 2 diabetes on hemodialysis detected by 23Na magnetic resonance imaging. *Kidney International*, *93*(5), 1191–1197. https://doi.org/10.1016/j.kint.2017.11.021

Kopp, C., Linz, P., Wachsmuth, L., Dahlmann, A., Horbach, T., Schöfl, C., Renz, W., Santoro, D., Niendorf, T., Müller, D. N., Neininger, M., Cavallaro, A., Eckardt, K.-U., Schmieder, R. E., Luft, F. C., Uder, M., & Titze, J. (2012). 23Na Magnetic Resonance Imaging of Tissue Sodium. *Hypertension*, *59*(1), 167–172. https://doi.org/10.1161/HYPERTENSIONAHA.111.183517

Kushnir, T., Knubovets, T., Itzchak, Y., Eliav, U., Sadeh, M., Rapoport, L., Kott, E., & Navon, G. (1997). In vivo 23Na NMR studies of myotonic dystrophy. *Magnetic Resonance in Medicine*, *37*(2), 192–196. https://doi.org/10.1002/mrm.1910370209

Landeghem, M. Van, Danieli, E., Perlo, J., Blümich, B., & Casanova, F. (2011). Low-gradient single-sided NMR sensor for one-shot profiling of human skin. *Journal of Magnetic Resonance*, *215*, 74–84. https://doi.org/10.1016/j.jmr.2011.12.010

Levitt, M. H. (2008). *Spin Dynamics. Basics of Nuclear Magnetic Resonance*. John Wiley & Sons, Ltd.

Li, Y., Liu, Y., Xia, W., Lei, D., Voorhees, J. J., & Fisher, G. J. (2013). Age-dependent alterations of decorin glycosaminoglycans in human skin. *Scientific Reports*, *3*. https://doi.org/10.1038/srep02422

Linz, P., Santoro, D., Renz, W., Rieger, J., Ruehle, A., Ruff, J., Deimling, M., Rakova, N., Muller, D. N., Luft, F. C., Titze, J., & Niendorf, T. (2014). Skin sodium measured with 23Na MRI at 7.0T. *NMR in Biomedicine*, *28*(1), 54–62. https://doi.org/10.1002/nbm.3224

Madelin, G., Kline, R., Walvick, R., & Regatte, R. R. (2014). A method for estimating intracellular sodium concentration and extracellular volume fraction in brain in vivo using sodium magnetic resonance imaging. *Scientific Reports*, *4*, 1–7. https://doi.org/10.1038/srep04763

Madelin, G., Lee, J. S., Regatte, R. R., & Jerschow, A. (2014). Sodium MRI: Methods and applications. *Progress in Nuclear Magnetic Resonance Spectroscopy*, *79*, 14–47. https://doi.org/10.1016/j.pnmrs.2014.02.001

Madhero88, & Komorniczak, M. (2012). *Skin layers.svg*. https://commons.wikimedia.org/w/index.php?curid=21986708. Licence: https://creativecommons.org/licenses/by-sa/3.0/deed.en

Man, P. P. (1995). Numerical analysis of Hahn echoes in solids. *Physical Review B*, *52*(13), 9418–9426. https://doi.org/10.1103/PhysRevB.52.9418

Maril, N., Rosen, Y., Reynolds, G. H., Ivanishev, A., Ngo, L., & Lenkinski, R. E. (2006). Sodium MRI of the human kidney at 3 Tesla. *Magnetic Resonance in Medicine*, *56*(6), 1229–1234. https://doi.org/10.1002/mrm.21031

McDonald, P. J. (1997). Stray field magnetic resonance imaging. *Progress in Nuclear Magnetic Resonance Spectroscopy*, *30*, 69–99.

McDonald, P. J., Akhmerov, A., Backhouse, L. J., & Pitts, S. (2005). Magnetic resonance profiling of human skin in vivo using GARField magnets. *Journal of Pharmaceutical Sciences*, *94*(8), 1850–1860. https://doi.org/10.1002/jps.20401

McDonald, P. J., & Newling, B. (1998). Stray Field Magnetic Resonance Imaging. *Reports on Progress in Physics*, *61*, 1441–1493. https://doi.org/10.1088/0034-4885/61/11/001

Meiboom, S., & Gill, D. (1958). Modified spin-echo method for measuring nuclear relaxation times. *Review of Scientific Instruments*, *29*(8), 688–691. https://doi.org/10.1063/1.1716296

Miltner, O., Schwaiger, A., Schmidt, C., Bücker, A., Kölker, C., Siebert, C. H., Zilkens, K. W., Niethard, F. U., & Blümich, B. (2003). Portable NMR-MOUSE(R): a New Method and Its Evaluation of the Achilles Tendon. *Zeitschrift Fur Orthopadie Und Ihre Grenzgebiete*, *141*(2), 148–152. https://doi.org/10.1055/s-2003-38657

Mispelter, J., & Lupu, M. (2008). Homogeneous resonators for magnetic resonance: A review. *Comptes Rendus Chimie*, *11*(4–5), 340–355. https://doi.org/10.1016/j.crci.2007.10.003

Mispelter, J., Lupu, M., & Briguet, A. (2015). *NMR Probeheads for Biophysical and Biomedical Experiments*. Imperial College Press.

Mitchell, J. (2016). Can sodium NMR provide more than a tracer for brine in petrophysics? *Journal of Petroleum Science and Engineering*, *146*, 360–368. https://doi.org/10.1016/j.petrol.2016.05.035

Mitchell, J., Blümler, P., & McDonald, P. J. (2006). Spatially resolved nuclear magnetic resonance studies of planar samples. *Progress in Nuclear Magnetic Resonance Spectroscopy*, *48*(4), 161–181. https://doi.org/10.1016/j.pnmrs.2006.04.001

Murphy, E., & Eisner, D. A. (2009). Regulation of Intracellular and Mitochondrial Sodium in Health and Disease. *Circulation Research*, *104*(3), 292–303. https://doi.org/10.1161/CIRCRESAHA.108.189050

Nagel, A. M., Bock, M., Hartmann, C., Gerigk, L., Neumann, J.-O., Weber, M.-A., Bendszus, M., Radbruch, A., Wick, W., Schlemmer, H.-P., Semmler, W., & Biller, A. (2011). The Potential of Relaxation-Weighted Sodium Magnetic Resonance Imaging as Demonstrated on Brain Tumors. *Investigative Radiology*, *46*(9), 539–547. https://doi.org/10.1097/RLI.0b013e31821ae918

Nalcioglu, O., & Cho, Z. H. (1984). Limits to signal-to-noise improvement by FID averaging in NMR imaging. *Physics in Medicine and Biology*, *29*(8), 969–978. https://doi.org/10.1088/0031-9155/29/8/005

Navon, G., Shinar, H., Eliav, U., & Seo, Y. (2001). Multiquantum filters and order in tissues. *NMR in Biomedicine*, *14*(2), 112–132. https://doi.org/10.1002/nbm.687

Nerbass, F. B., Calice-Silva, V., & Pecoits-Filho, R. (2018). Sodium Intake and Blood Pressure in Patients with Chronic Kidney Disease: A Salty Relationship. *Blood Purification*, *45*, 166–172. https://doi.org/10.1159/000485154

Nijst, P., Verbrugge, F. H., Grieten, L., Dupont, M., Steels, P., Tang, W. H. W., & Mullens, W. (2015). The pathophysiological role of interstitial sodium in heart failure. *Journal of the American College of Cardiology*, *65*(4), 378–388. https://doi.org/10.1016/j.jacc.2014.11.025

Oh, J.-H., Kim, Y. K., Jung, J.-Y., Shin, J., Kim, K. H., Cho, K. H., Eun, H. C., & Chung, J. H. (2011). Intrinsic aging- and photoaging-dependent level changes of glycosaminoglycans and their correlation with water content in human skin. *Journal of Dermatological Science*, *62*(3), 192–201. https://doi.org/10.1016/j.jdermsci.2011.02.007

Olde Engberink, R. H. G., Rorije, N. M. G., van den Born, B.-J. H., & Vogt, L. (2017). Quantification of nonosmotic sodium storage capacity following acute hypertonic saline infusion in healthy individuals. *Kidney International*, *91*(3), 738–745. https://doi.org/10.1016/j.kint.2016.12.004

Oltulu, P., Ince, B., Kökbudak, N., Findik, S., & Kiliç, F. (2018). Measurement of epidermis, dermis, and total skin thicknesses from six different body regions with a new ethical histometric technique. *Turk Plastik, Rekonstruktif ve Estetik Cerrahi Dergisi*, *26*(2), 56–61. https://doi.org/10.4103/tjps.tjps_2_17

Ooms, K. J., Cannella, M., Vega, A. J., Marcolongo, M., & Polenova, T. (2008). The application of 23Na double-quantum-filter (DQF) NMR spectroscopy for the study of spinal disc degeneration. *Magnetic Resonance in Medicine*, *60*(2), 246–252. https://doi.org/10.1002/mrm.21637

Ouwerkerk, R. (2011). Sodium MRI. In M. Modo & J. W. M. Bulte (Eds.), *Magnetic Resonance Imaging: Methods and Protocols* (pp. 175–203). Springer.

https://doi.org/10.1007/978-1-4939-5611-1_26

Ouwerkerk, R., Bleich, K. B., Gillen, J. S., Pomper, M. G., & Bottomley, P. A. (2003). Tissue Sodium Concentration in Human Brain Tumors as Measured with 23Na MR Imaging. *Radiology*, *227*(2), 529–537. https://doi.org/10.1148/radiol.2272020483

Ouwerkerk, R., Bottomley, P. A., Solaiyappan, M., Spooner, A. E., Tomaselli, G. F., Wu, K. C., & Weiss, R. G. (2008). Tissue Sodium Concentration in Myocardial Infarction in Humans: A Quantitative 23 Na MR Imaging Study. *Radiology*, *248*(1), 88–96. https://doi.org/10.1148/radiol.2481071027

Ouwerkerk, R., Jacobs, M. A., Macura, K. J., Wolff, A. C., Stearns, V., Mezban, S. D., Khouri, N. F., Bluemke, D. A., & Bottomley, P. A. (2007). Elevated tissue sodium concentration in malignant breast lesions detected with non-invasive 23Na MRI. *Breast Cancer Research and Treatment*, *106*(2), 151–160. https://doi.org/10.1007/s10549-006-9485-4

Perlo, J., Casanova, F., & Blümich, B. (2005). Profiles with microscopic resolution by single-sided NMR. *Journal of Magnetic Resonance*, *176*(1), 64–70. https://doi.org/10.1016/j.jmr.2005.05.017

Piculell, L., & Nilsson, S. (1989). Anion-specific salt effects in aqueous agarose systems. 2. Nuclear spin relaxation of ions in agarose gels and solutions. *Journal of Physical Chemistry*, *93*(14), 5602–5611. https://doi.org/10.1021/j100351a054

Pirahanchi, Y., Jessu, R., & Aeddula, N. R. (2023). *Physiology, Sodium Potassium Pump*. StatPearls [Internet]. Treasure Island (FL): StatPearls Publishing; 2023 Jan-. https://www.ncbi.nlm.nih.gov/books/NBK537088/

Pollock, M. L., Hickman, T., Kendrick, Z., Jackson, A., Linnerud, A. C., & Dawson, G. (1976). Prediction of body density in young and middle aged men. *Journal of Applied Physiology*, *40*(3), 300–304. https://doi.org/10.1152/jappl.1976.40.3.300

Pollock, M. L., Laughridge, E. E., Coleman, B., Linnerud, A. C., & Jackson, A. (1975). Prediction of body density in young and middle aged women. *Journal of Applied Physiology*, *38*(4), 745–749. https://doi.org/10.1152/jappl.1975.38.4.745

Qirjazi, E., Salerno, F. R., Akbari, A., Hur, L., Penny, J., Scholl, T., & McIntyre, C. W. (2021). Tissue sodium concentrations in chronic kidney disease and dialysis patients by lower leg sodium-23 magnetic resonance imaging. *Nephrology Dialysis Transplantation*, *36*(7), 1234–1243. https://doi.org/10.1093/ndt/gfaa036

Queval, L. (2022). *Biot Savart magnetic Toolbox*. GidHub. https://github.com/lqueval/BSmag

Randall, E. W. (2011). Stray-Field (STRAFI) NMR: Imaging in Large Field Gradients. *Encyclopedia of Magnetic Resonance*, 1–16. https://doi.org/10.1002/9780470034590.emrstm0534.pub2

Reddy, R., Insko, E. K., & Leigh, J. S. (1997). Triple quantum sodium imaging of articular cartilage. *Magnetic Resonance in Medicine*, *38*(2), 279–284. https://doi.org/10.1002/mrm.1910380218

Reddy, R., Li, S., Noyszewski, E. A., Kneeland, J. B., & Leigh, J. S. (1997). In vivo sodium multiple quantum spectroscopy of human articular cartilage. *Magnetic Resonance in Medicine*, *38*(2), 207–214. https://doi.org/10.1002/mrm.1910380208

Roemer, P. B., Edelstein, W. A., Hayes, C. E., Souza, S. P., & Mueller, O. M. (1990). The NMR phased array. *Magnetic Resonance in Medicine*, *16*(2), 192–225. https://doi.org/10.1002/mrm.1910160203

Rooney, W. D., Barbara, T. M., & Springer, C. S. J. (1988). Two-Dimensional Double-Quantum NMR Spectroscopy of Isolated Spin 3/2 Systems: 23Na Examples. *Journal of the American Chemical Society*, *110*(1), 674–681.

Rooney, W. D., & Springer, C. S. J. (1991a). The molecular environment of intracellular sodium: 23Na NMR relaxation. *NMR in Biomedicine*, *4*(5), 227–245. https://doi.org/10.1002/nbm.1940040503

Rooney, W. D., & Springer, C. S. J. (1991b). A comprehensive approach to the analysis and interpretation of the resonances of spins 3/2 from living systems. *NMR in Biomedicine*, *4*(5), 209–226. http://www.ncbi.nlm.nih.gov/pubmed/1751345

Rose, A. M., & Valdes Jr, R. (1994). Understanding the Sodium Pump and Its Relevance to Disease. *Clinical Chemistry Cun. Chem*, *40*(9), 1674–1685.

Rosen, Y., & Lenkinski, R. E. (2009). Sodium MRI of a Human Transplanted Kidney. *Academic Radiology*, *16*(7), 886–889. https://doi.org/10.1016/J.ACRA.2009.01.010

Rundo, J., & Bunce, L. J. (1966). Estimation of the total hydrogen content of the human body. *Nature*, *210*(5040), 1023–1024. https://doi.org/10.1038/2101023a0

Ruperto, M., Sánchez-Muniz, F. J., & Barril, G. (2019). Extracellular mass to body cell mass ratio as a potential index of wasting and fluid overload in hemodialysis patients. A case-control study. *Clinical Nutrition*, *39*(4), 1117–1123. https://doi.org/10.1016/j.clnu.2019.04.021

Schneider, M. P., Raff, U., Kopp, C., Scheppach, J. B., Toncar, S., Wanner, C., Schlieper, G., Saritas, T., Floege, J., Schmid, M., Birukov, A., Dahlmann, A., Linz, P., Janka, R., Uder, M., Schmieder, R. E., Titze, J., & Eckardt, K.-U. (2017). Skin Sodium Concentration Correlates with Left Ventricular Hypertrophy in CKD. *Journal of the American Society of Nephrology*, *28*(6), 1867–1876. https://doi.org/10.1681/ASN.2016060662

Selvarajah, V., Connolly, K., McEniery, C., & Wilkinson, I. (2018). Skin Sodium and Hypertension: a Paradigm Shift? *Current Hypertension Reports*, *20*(11), 1–8. https://doi.org/10.1007/s11906-018-0892-9

Selvarajah, V., Mäki-Petäjä, K. M., Pedro, L., Bruggraber, S. F. A., Burling, K., Goodhart, A. K., Brown, M. J., McEniery, C. M., & Wilkinson, I. B. (2017). Novel Mechanism for Buffering Dietary Salt in Humans: Effects of Salt Loading on Skin Sodium, Vascular Endothelial Growth Factor C, and Blood Pressure. *Hypertension*, *70*(5), 930–937. https://doi.org/10.1161/HYPERTENSIONAHA.117.10003

Shinar, H., Knubovets, T., Eliav, U., & Navon, G. (1993). Sodium interaction with ordered structures in mammalian red blood cells detected by Na-23 double quantum NMR. *Biophysical Journal*, *64*(4), 1273–1279. https://doi.org/10.1016/S0006-3495(93)81492-9

Skou, J. C., & Esmann, M. (1992). The Na,K-ATPase. *Journal of Bioenergetics and Biomembranes*, *24*(3), 249–261. https://doi.org/10.1007/BF00768846

Slichter, C. P. (1996). *Principles of Magnetic Resonance* (3rd Enlarg). Springer-

Verlag.

Smith, M. M., & Melrose, J. (2015). Proteoglycans in Normal and Healing Skin. *Advances in Wound Care*, *4*(3), 152–173. https://doi.org/10.1089/wound.2013.0464

Soo Lim, H., Young Hwang, J., Choi, E. A., Lee, G., Sun Yoon, S., & Kim, M. K. (2018). Development and validation of HPLC method for the determination of ferrocyanide ion in food grade salts. *Food Chemistry*, *239*, 1167–1174. https://doi.org/10.1016/j.foodchem.2017.07.070

Springer, C. S. J. (2007). Biological Systems: Spin-3/2 Nuclei. *EMagRes, Online*, *2007*, 1–12. https://doi.org/10.1002/9780470034590.emrstm0029

Stapf, S., & Han, S. (2006). NMR Imaging in Chemical Engineering. In S. Stapf & S. Han (Eds.), *Focus on Catalysts*. WILEY-VCH Verlag GmbH & Co. KGaA, Weinheim All. https://doi.org/10.1016/s1351-4180(07)70357-4

Tauskela, J. S., & Shoubridge, E. A. (1993). Response of the 23Na-NMR double-quantum filtered signal to changes in Na+ ion concentration in model biological solutions and human erythrocytes. *BBA - General Subjects*, *1158*(2), 155–165. https://doi.org/10.1016/0304-4165(93)90009-W

Téllez-Soto, C. A., Pereira Silva, M. G., dos Santos, L., de O. Mendes, T., Singh, P., Fortes, S. A., Favero, P., & Martin, A. A. (2021). In vivo determination of dermal water content in chronological skin aging by confocal Raman spectroscopy. *Vibrational Spectroscopy*, *112*(November 2020). https://doi.org/10.1016/j.vibspec.2020.103196

Terman, F. E. (1943). *Radio engineer's handbook* (1st Edition). McGraw-Hill Book Company, Inc.

Titze, J., Shakibaei, M., Schafflhuber, M., Schulze-Tanzil, G., Porst, M., Schwind, K. H., Dietsch, P., & Hilgers, K. F. (2004). Glycosaminoglycan polymerization may enable osmotically inactive Na+ storage in the skin. *American Journal of Physiology-Heart and Circulatory Physiology*, *287*(1), H203–H208. https://doi.org/10.1152/ajpheart.01237.2003

Tobin, D. J. (2006). Biochemistry of human skin - our brain on the outside. *Chemical Society Reviews*, *35*(1), 52–67. https://doi.org/10.1039/b505793k

Unpublished data. (2018). *Fomina D.V., Volkov D. V., Pirogov Y. A., Pavlovskaya G. E.*

Van Der Maarel, J. R. C. (2003). Thermal relaxation and coherence dynamics of spin 3/2. I. Static and fluctuating quadrupolar interactions in the multipole basis. *Concepts in Magnetic Resonance Part A: Bridging Education and Research*, *19*(2), 97–116. https://doi.org/10.1002/cmr.a.10087

Van Zuijlen, P. P. M., Ruurda, J. J. B., Van Veen, H. A., Van Marle, J., Van Trier, A. J. M., Groenevelt, F., Kreis, R. W., & Middelkoop, E. (2003). Collagen morphology in human skin and scar tissue: No adaptations in response to mechanical loading at joints. *Burns*, *29*(5), 423–431. https://doi.org/10.1016/S0305-4179(03)00052-4

Wang, P., Deger, M. S., Kang, H., Ikizler, T. A., Titze, J., & Gore, J. C. (2017). Sex differences in sodium deposition in human muscle and skin. *Magnetic Resonance Imaging*, *36*, 93–97. https://doi.org/10.1016/j.mri.2016.10.023

Watzlaw, J., Glöggler, S., Blümich, B., Mokwa, W., & Schnakenberg, U. (2013). Stacked planar micro coils for single-sided NMR applications. *Journal of Magnetic Resonance*, *230*, 176–185. https://doi.org/10.1016/j.jmr.2013.02.013

Weidmann, P., & Ferrari, P. (1991). Central Role of Sodium in Hypertension in Diabetic Subjects. *Diabetes Care*, *14*(3), 220–232. https://doi.org/doi.org/10.2337/diacare.14.3.220

Wetterling, F., Corteville, D. M., Kalayciyan, R., Rennings, A., Konstandin, S., Nagel, A. M., Stark, H., & Schad, L. R. (2012). Whole body sodium MRI at 3T using an asymmetric birdcage resonator and short echo time sequence: first images of a male volunteer. *Physics in Medicine and Biology*, *57*(14), 4555–4567. https://doi.org/10.1088/0031-9155/57/14/4555

Wheaton, A. J., Borthakur, A., Shapiro, E. M., Regatte, R. R., Akella, S. V. S., Kneeland, J. B., & Reddy, R. (2004). Proteoglycan Loss in Human Knee Cartilage: Quantitation with Sodium MR Imaging — Feasibility Study. *Radiology*, *231*(3), 900–905. https://doi.org/10.1148/radiol.2313030521

Wimperis, S. (2011). Relaxation of Quadrupolar Nuclei Measured via Multiple-Quantum Filtration. *EMagRes*, *2011*(3).

https://doi.org/10.1002/9780470034590.emrstm0462.pub2

Wimperis, S., & Wood, B. (1991). Triple-quantum sodium imaging. *Journal of Magnetic Resonance (1969)*, *95*(2), 428–436. https://doi.org/10.1016/0022-2364(91)90234-K

Woessner, D. E. (2001). NMR relaxation of spin-3/2 nuclei: Effects of structure, order, and dynamics in aqueous heterogeneous systems. *Concepts in Magnetic Resonance*, *13*(5), 294–325. https://doi.org/10.1002/cmr.1015

Woessner, D. E., & Bansal, N. (1998). Temporal Characteristics of NMR Signals from Spin 3/2 Nuclei of Incompletely Disordered Systems. *Journal of Magnetic Resonance*, *133*(1), 21–35. https://doi.org/10.1006/jmre.1998.1423

Wright, E. M., Loo, D. D. F., & Hirayama, B. A. (2011). Biology of Human Sodium Glucose Transporters. *Physiological Reviews*, *91*(2), 733–794. https://doi.org/10.1152/physrev.00055.2009

Younes, M., Aggett, P., Aguilar, F., Crebelli, R., Dusemund, B., Filipič, M., Frutos, M. J., Galtier, P., Gott, D., Gundert-Remy, U., Kuhnle, G. G., Lambré, C., Leblanc, J. C., Lillegaard, I. T., Moldeus, P., Mortensen, A., Oskarsson, A., Stankovic, I., Waalkens-Berendsen, I., … Woutersen, R. A. (2018). Re-evaluation of sodium ferrocyanide (E 535), potassium ferrocyanide (E 536) and calcium ferrocyanide (E 538) as food additives. *EFSA Journal*, *16*(7), 5374–26. https://doi.org/10.2903/j.efsa.2018.5374

Yu, E., & Sharma, S. (2022). *Cystic Fibrosis*. Treasure Island (FL): StatPearls Publishing; 2023 Jan-. https://www.ncbi.nlm.nih.gov/books/NBK493206/

Zbýň, S., Mlynárik, V., Juras, V., Szomolanyi, P., & Trattnig, S. (2014). Sodium MR Imaging of Articular Cartilage Pathologies. *Current Radiology Reports*, *2*(4), 41. https://doi.org/10.1007/s40134-014-0041-4

Zeece, M. (2020). Food additives. In M. Zeece (Ed.), *Introduction to the Chemistry of Food* (pp. 251–311). Academic Press. https://doi.org/10.1016/B978-0-12-809434-1.00007-4

Zia, W. (2016). *Advances in Compact Magnetic Resonance: Devices, Methodologies, and Investigations*.

Zimmermann, D. R., Dours-Zimmermann, M. T., Schubert, M., & Bruckner-

Tuderman, L. (1994). Versican is expressed in the proliferating zone in the epidermis and in association with the elastic network of the dermis. *Journal of Cell Biology*, *124*(5), 817–825. https://doi.org/10.1083/jcb.124.5.817

Appendix A. Processing of the DQF-MA data

The DFQ-MA data for processing was extracted from TopSpin. In TopSpin, after an experiment finishes, spectrum data for all 23 FIDs was obtained from the time-domain data using a command “xf2” that performs apodization, 1D Fourier Transform and baseline correction for every FID. Later, both real and imaginary parts of the FIDs were saved as separate files with an extension “.txt” to read by MATLAB. Processing in MATLAB was performed by the following code:

```
%% Load data from TopSpin files “filename_re.txt” and
“filename_im.txt” as an example
SpectraRe(:,:) = readmatrix(”C:\Users\...\filename_re.txt”);
SpectraIm(:,:) = readmatrix(”C:\Users\...\filename_im.txt”);

N = 1024; %number of points in the spectrum
NE = 23; %number of FIDs

% Removing values which are not numbers and creating new arrays
for real and imaginary data Specre and Specim
k = isnan(SpectraRe);
m = isnan(SpectraIm);
Specre = SpectraRe(~k);
Specim = SpectraIm(~m);
echoes = zeros(N,NE);

% Filling in the arrays Specre and Specim
index = 1;
ec = 1;
for j = 1:N*NE
    echoes(index,ec) = Specre(j)+1i*Specim(j);
    index = index+1;
    if index > N
        ec = ec+1;
        index = 1;
    end
end
```

```
%% Plot the data
SWH = 6250; % spectral width in Hz
Hz = linspace(0,SWH,N);
Hz = Hz’;
for ec = 1:1:NE
    figure;
    plot(Hz,real(echoes(:,ec)),Hz,imag(echoes(:,ec)));
    hold on;
    title(['Spectrum ' num2str(ec) ', LB = 150 Hz']);
    xlabel('Frequency, Hz');
    ylabel('Amplitude, a.u.');
    legend({'Re','Im'},'Location','northeast');
    axis tight;
    grid on;
    hold off;

    x0 = 1400;
    y0 = 500;
    width = 500;
    height = 400;
```

```
    set(gcf,'position',[x0,y0,width,height]);
end
```

```
%% Make a projection and phase it
Spectra1sum = sum(echoes,2);
Spectra1sumph = Spectra1sum;

% Phasing the projection
line = zeros(N,1);
    k = 1;
    for deg = 0:1:20 % range in degrees for phase correction
        Spectra1sumph = Spectra1sum*exp(-1i*2*pi/360*deg); % p0
correction
% As the real part of the spectra needs to be phased as anti-
phased doublet, for the best phasing a minimum difference in
absolute hights of the positive and negative peaks is found and
plotted vs degrees of phase correction.
        max1 = max(real(Spectra1sumph));
        min1 = abs(min(real(Spectra1sumph)));
        delta(k,1) = deg;
        delta(k,2) = abs(max1-min1);
            figure;
            plot(Hz,real(Spectra1sumph),Hz,imag(Spectra1sumph));
            title(['Degrees ' num2str(deg)]);
            hold on
            plot(Hz,line);
        k = k+1;
    end
figure
plot(delta(:,1),delta(:,2))
```

```
%% Apply the phase to all the spectra
echoesph = zeros(N,NE);
degmax = 11; % determined from the graph of delta(:,2) vs
delta(:,1) in the previous section
for spNo = 1:1:NE
    echoesph(:,spNo) = echoes(:,spNo)*exp(-1i*2*pi/360*degmax);
end
```

```
%% Find frequency difference between the peaks
freq = zeros(NE,2); % Frequency positions of the positive and
negative peaks
omegaQ = zeros(NE,1); % Frequency difference between the peaks
amp = zeros(NE,1);
maxmin = zeros(NE,2);

for spNo = 1:1:NE
    max1 = max(real(echoesph(:,spNo)));
    min1 = min(real(echoesph(:,spNo)));
    maxmin(spNo,1) = max1;
    maxmin(spNo,2) = min1;
    idx1 = find(real(echoesph(:,spNo)) == max1);
    idx2 = find(real(echoesph(:,spNo)) == min1);
    freq(spNo,1) = Hz(idx1);
    freq(spNo,2) = Hz(idx2);
    omegaQ(spNo,1) = abs(freq(spNo,2) - freq(spNo,1));
    amp(spNo,1) = max1 - min1; % Amplitude of the signal
determined as a sum of absolute values of positive and negative
peaks’ heights
end

% Plot the phased spectra with marked peak positions
for spNo = 1:1:NE
```

```
    figure;
    plot(Hz,real(echoesph(:,spNo)),Hz,imag(echoesph(:,spNo)));
    hold on;
plot(freq(spNo,1),maxmin(spNo,1),'*r',freq(spNo,2),maxmin(spNo,2),
'*r');
    title(['Phased Spectrum ' num2str(spNo)]);
    xlabel('Frequency, Hz');
    ylabel('Amplitude, a.u.');
    legend({'Re','Im'},'Location','northeast');
    axis tight;
    grid on;
    hold off;
    x0 = 1400;
    y0 = 555;
    width = 500;
    height = 400;
    set(gcf,'position',[x0,y0,width,height]);
        filename = ['spectrum' num2str(spNo) 'ph' num2str(degmax)
'd.tif']; saveas(gcf,filename);
end
% After 15th spectrum, SNR drops dramatically, and it was
impossible to determine peak positions adequately using the
algorithm above. Therefore, peak positions were determined
manually to find frequency difference between them.
```

```
%% Save processed data in .txt
pulse90 = 50; % length of 90° pulse in microsec
pulse180 = 100; % length of 180° pulse in microsec
tau =
1000*[0.0002,0.0003,0.0004,0.0005,0.0006,0.0007,0.0008,0.0009,0.00
1,0.0015,0.002,0.003,0.004,0.005,0.006,0.007,0.008,0.009,0.01,0.01
5,0.02,0.05,0.1]'; % time interval between 90° and 180° pulses and
between 180° and 54.74° pulses in ms
taufull = pulse90/2/1000+tau+pulse180/1000; % preparation time τ

% Save build-up curve
Calc = zeros(23,3);
Calc(:,1) = taufull;
Calc(:,2) = amp2; % Peak amplitudes after manual correction for
spectrum number > 15
Calc(:,3) = omegaQ2; % Frequency difference between positive and
negative peaks after manual correction for spectrum number > 15
T = array2table(Calc);
T.Properties.VariableNames(1:3) = {'Tau_full,ms','MaxInt','wQ'};
filename = ['60_lb150_tau_maxint_wQ.txt'];
writetable(T,filename,'Delimiter',' ');

% Save phased spectra
Exper = zeros(N,NE+1);
Exper(:,1) = Hz;
Exper(:,2:NE+1) = echoesph;
T = array2table(Exper);
n = [1:1:NE];
colnames = "Spectrum" + n;
T.Properties.VariableNames(1) = {'Time'};
T.Properties.VariableNames(2:NE+1) = colnames;
filename = ['SpectraPh' num2str(degmax) 'd.txt'];
writetable(T,filename,'Delimiter',' ');
```

Appendix B. T_{2short} and T_{2long} obtained from CPMG

Table B.1. Values of T_{2short} and T_{2long} with their errors obtained from biexponential fitting of CPMG to eq. [3.8] for samples collected from the foot/leg and abdomen of control and diabetic patients.

Patient	**Sample**	**Location**	T_{2short}, **ms**	T_{2long}, **ms**
C1	1	abdomen	0.854 ± 0.086	13.216 ± 0.561
C2	1	abdomen	0.776 ± 0.065	12.524 ± 0.387
C2	2	abdomen	0.998 ± 0.120	13.186 ± 0.762
C3	1	abdomen	0.882 ± 0.084	13.095 ± 0.538
C3	2	abdomen	0.909 ± 0.118	14.216 ± 0.853
C4	1	abdomen	1.186 ± 0.266	14.515 ± 1.760
C4	2	abdomen	0.650 ± 0.103	13.587 ± 0.603
C5	1	foot/leg	0.967 ± 0.126	14.573 ± 0.933
C5	2	foot/leg	1.097 ± 0.147	15.996 ± 1.200
C5	3	foot/leg	0.562 ± 0.228	13.197 ± 1.070
C5	4	foot/leg	0.923 ± 0.109	14.596 ± 0.814
C6	1	abdomen	0.748 ± 0.055	14.471 ± 0.389
C6	2	abdomen	0.955 ± 0.063	15.125 ± 0.493
D1	1	foot/leg	0.879 ± 0.062	17.030 ± 0.582
D1	2	foot/leg	0.931 ± 0.096	18.113 ± 1.010
D2	1	foot/leg	0.600 ± 0.177	17.897 ± 1.430
D3	1	foot/leg	0.858 ± 0.072	18.065 ± 0.744
D3	2	foot/leg	0.792 ± 0.132	16.854 ± 1.190
D4	1	foot/leg	0.751 ± 0.123	18.991 ± 1.320
D4	2	foot/leg	0.658 ± 0.025	19.824 ± 0.201
D5	1	foot/leg	0.845 ± 0.040	18.557 ± 0.347
D5	2	foot/leg	0.945 ± 0.060	19.983 ± 0.740
D6	2	foot/leg	0.662 ± 0.035	21.305 ± 0.233

Appendix C. T_{2short}, T_{2long} and ω'_Q obtained from DQF-MA and TQF

Table C.1. Values of T_{2short}, ω'_Q and T_{2long} with their errors obtained from fitting of build-up curves of DQF-MA (eq. [3.10]) and TQF (eq. [3.12]) experiments (Subsections 3.4.2.1-3.4.2.2) for all samples collected from the foot/leg and abdomen of control and diabetic patients.

Patient	Sample	Location	T_{2short}, ms	ω'_Q, Hz	T_{2long}, ms
C1	2	abdomen	0.711±0.063	33.2±20.2	20.47±3.95
C2	1	abdomen	0.580±0.032	78.6±17.4	20.53±3.23
C2	2	abdomen	0.642±0.057	0.0±16.5	23.73±2.94
C3	1	abdomen	0.854±0.082	1.4±17.1	25.71±4.74
C3	2	abdomen	0.978±0.079	1.2±13.8	25.60±5.20
C4	1	abdomen	0.510±0.067	578±147	22.32±2.27
C4	2	abdomen	0.961±0.126	142.0±43.2	21.48±4.75
C5	1	foot/leg	0.991±0.116	96.3±32.4	25.69±5.08
C5	2	foot/leg	1.234±0.088	41.4±15.1	24.62±5.16
C5	3	foot/leg	1.086±0.065	128.8±18.3	25.46±4.60
C5	4	foot/leg	0.899±0.052	30.8±12.1	27.47±4.26
C6	1	abdomen	0.826±0.047	52.6±13.8	21.23±3.93
C6	2	abdomen	1.134±0.067	117.1±17.2	29.74±7.72
D1	1	foot/leg	0.891±0.037	51.4±9.8	27.65±4.82
D1	2	foot/leg	0.621±0.060	137.3±37.3	24.91±3.98
D3	1	foot/leg	0.786±0.047	62.7±15.6	33.77±2.52
D3	2	foot/leg	0.952±0.086	0.0±15.5	28.75±4.10
D4	1	foot/leg	0.480±0.072	239.2±90.1	21.33±2.39
D4	2	foot/leg	1.149±0.063	9.2±9.6	28.43±6.40
D5	1	foot/leg	0.544±0.072	137.4±54.9	27.24±1.54
D5	2	foot/leg	1.062±0.083	66.3±18.8	27.28±5.99